UNIVERSITY OF CALIFORNIA SAN DIEGO

Silicon rich silicon carbide for integrated photonic applications

A Dissertation submitted in partial satisfaction of the requirements
for the degree Doctor of Philosophy

in

Materials Science and Engineering

by

Li-Yang Chang

Committee in charge:

Professor Paul Yu, Chair
Professor Prabhakar R. Bandaru
Professor Y. Shaya Fainman
Professor Zhaowei Liu

2023

The Dissertation of Li-Yang Chang is approved, and it is acceptable in quality and form for publication on microfilm and electronically.

University of California San Diego

2023

TABLE OF CONTENTS

LIST OF FIGURES

LIST OF TABLES

ACKNOWLEDGEMENTS

I would like to extend my heartfelt gratitude to the following individuals and groups, whose support, guidance, and encouragement have been invaluable throughout my academic journey.

First and foremost, I am deeply indebted to Prof. Paul Yu for his exceptional guidance, mentorship, and unwavering support as my adviser. His wisdom, expertise, and dedication to research have been instrumental in shaping my academic and research endeavors.

My sincere appreciation extends to Dr. Steve Pappert, whose contributions have been akin to that of a second adviser. His invaluable insights and collaboration have significantly enriched my research experience.

I extend my gratitude to my esteemed committee members, Prof. Shaya Fainman, Prof. Zhaowei Liu, and Prof. Prabhakar Bandaru, for their invaluable insights, feedback, and guidance, all of which have greatly fortified my thesis.

A special acknowledgment goes to Prof. Alexey Arefiev for offering me TA positions for consecutive years. Your support during financially challenging times was invaluable, and it was a pleasure working alongside you.

My sincere thanks to the Nano3 staff, with a special mention of Dr. Maribel Montero, whose expertise in electron beam lithography and support in the cleanroom were indispensable to my research endeavors.

I owe a debt of gratitude to my fellow researchers at UCSD, with a heartfelt thank you to Dr. Hani Nejadriahi for her invaluable support in the lab, particularly her assistance with device measurement. It’s very nice working with you in the group. Po-Chun Chen, it's always fun working with you in the Nano3, and I am grateful for the knowledge I learned from you in fabrication skills. Reuniting with you in graduate school after college has been a wonderful journey. Chi-Hsin Huang, your insightful suggestions during challenging times have been pivotal in overcoming research obstacles. I always remember those late-night meals we had together after working so late in the lab.

To my dear Taiwanese friends in San Diego, though not directly involved in research, your companionship and warmth have made me feel at home, even thousands of miles away. Your support has been an anchor during this journey.

I want to extend my heartfelt thanks to my girlfriend, Ching-Jui, who has played multiple roles as my cheerleader, mentor, hero, best friend, and eventually, my everything. Her continuous support has steered me towards positivity, kindness, responsibility, and becoming a better person.

Last but not least, my family holds a special place in my heart. To my mom and dad, your lifelong support, love, and belief in me have been an enduring source of strength. I am profoundly grateful for everything you have done, as none of this would have been possible without you.

To everyone mentioned, as well as the countless others who have contributed to my academic and personal growth, thank you for being an integral part of this incredible journey.

Chapter 2, in part, is a reprint of the materials as it appears in Applied Physics Letters 2022. Li-Yang Sunny Chang, Hani Nejadriahi, Steve Pappert, and Paul K. L. Yu. The dissertation author is the primary investigator and author of this paper.

Chapter 3, in part, is a reprint of the materials as it appears in Applied Physics Letters 2022. Li-Yang Sunny Chang, Hani Nejadriahi, Steve Pappert, and Paul K. L. Yu. The dissertation author is the primary investigator and author of this paper.

Chapter 4, in part, is a reprint of the materials as it appears in Optics Letters 2023. Li-Yang Sunny Chang, Steve Pappert, and Paul K. L. Yu. The dissertation author is the primary investigator and author of this paper.

Chapter 5 contains unpublished material coauthored with Li-Yang Sunny Chang, Steve Pappert, and Paul K. L. Yu. The dissertation author was the primary investigator of this chapter.

VITA

2014 B.S. in Materials Science and Engineering, National Taiwan University

2017 M.S. in Materials Science and Engineering, Carnegie Mellon University

2023 Ph.D. in Materials Science and Engineering, University of California San Diego

PUBLICATIONS

1. **Li-Yang Sunny Chang**, Steve Pappert, and Paul K. L. Yu, "Efficient thermo-optic micro-ring phase shifter made of PECVD silicon-rich amorphous silicon carbide", Optics Letters. 48, 1188-1191 (2023)
2. **Li-Yang Sunny Chang**, Steve Pappert, and Paul K. L. Yu, "Thermo-optic properties in PECVD silicon rich silicon carbide", OSA Advanced Photonic Congress (2022)
3. **Li-Yang Sunny Chang**, Hani Nejadriahi, Steve Pappert, and Paul K. L. Yu, "Demonstration of DC Kerr effect induced high nonlinear susceptibility in silicon rich amorphous silicon carbide", Applied Physics Letter 120, 071107 (2022)

ABSTRACT OF THE DISSERTATION

Silicon rich silicon carbide for integrated photonic applications

by

Li-Yang Chang

Doctor of Philosophy in Materials Science and Engineering

University of California San Diego, 2023

Professor Paul Yu, Chair

Silicon photonics is a rapidly growing field of technology that focuses on the use of silicon-based materials to manipulate light in order to transmit information. By leveraging the unique properties of silicon-based materials, silicon photonics offers several advantages over conventional electronic-based technologies. Silicon is a mature CMOS material and is one of the most widely used integrated photonic platforms. However, silicon has a relatively smaller

band gap, which limits its power handling capabilities due to two-photon absorption, making it unsuitable for high-intensity nonlinear optical processing.

In this dissertation, I will show our effort in developing silicon rich carbide (SRC) as a new photonic material that addresses the limitations of silicon. By increasing the silicon content, SRC offers enhanced nonlinearity while maintaining a wider band gap than silicon. Results demonstrate a 7-fold increase in nonlinearity compared to stoichiometric silicon carbide. Additionally, preliminary work on a Si/SRC hybrid waveguide modulator is presented, utilizing the quadratic EO effect (DC Kerr effect).

Another important active photonic building block is the phase shifter. Many photonic applications, including optical modulators and all-optical switches, rely on tunability to control the optical properties in PICs. One of the common mechanisms that is used for circuit tuning is the thermo-optic effect. The dissertation will show our work on exploring the thermo-optic coefficient (TOC) of the SRC material and demonstrates a 3-fold improvement in the TOC with respect to the stoichiometric silicon carbide. An efficient thermo-optic phase shifter is also demonstrated using SRC.

In conclusion, SRC, with its high nonlinearities, high power handling capability, high TOC, and compatibility with CMOS processing, shows great potential as a promising material candidate for integrated photonic applications.

CHAPTER 1: SILICON PHOTONICS TECHNOLOGY STATUS AND CHALLENGE

1.1 Background

Data traffic has been rapidly increasing in our daily lives due to the proliferation of devices, the growth of the internet, and the rise of various digital services. From streaming video and social media to online shopping and remote work, data traffic has become an integral part of our daily lives. With the advent of technologies like 5G, the Internet of Things (IoT), cloud computing, and Artificial Intelligence (AI), there has been an exponential increase in the amount of data that is being transmitted and processed. As a result, data traffic has become a critical aspect of our daily lives, and it is expected to continue growing at an unprecedented rate into the future.

Telecom companies have been predicting a massive surge in data traffic for many years now, and their predictions have been largely accurate. **Figure 1.1** shows the growth of the reported global connections by Cisco. According to the Cisco Annual Internet Report, the number of devices connected to IP network will be more than three times the global population by 2023 [1]. Additionally, Ericsson Mobility Report forecasts that by 2028, there will be 5 billion mobile subscriptions to 5G networks, which accounting for 55% of all mobile subscriptions, leading to a massive increase in mobile data traffic [2]. Both reports predict an enormous demand in future video steaming. **Figure 1.2** shows the demands of the bandwidth for future video applications. Ericsson forecasts that the demand for video services will continue to increase by 30% annually, which will account for 80% of mobile data traffic by the end of 2028.

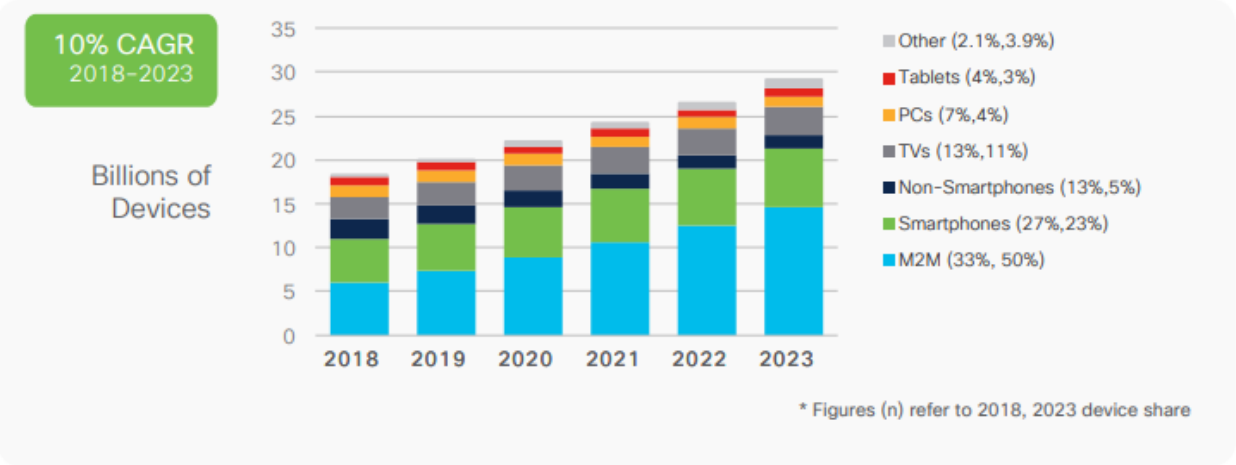

Source: Cisco Annual Internet Report, 2018–2023

Figure 1.1 The reported global devices and connection growth from Cisco.

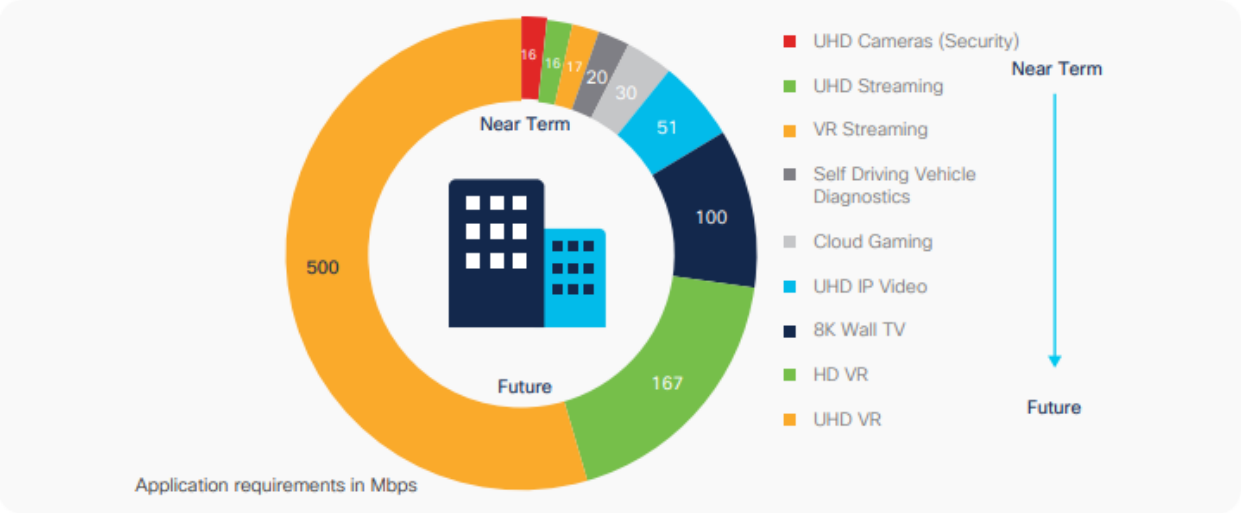

Source: Cisco Annual Internet Report, 2018–2023

Figure 1.2 The demand of bandwidth for video applications in the future.

The massive influx of data traffic requires high-speed, energy-efficient, and cost-effective solutions. Traditional electronic-based technologies are struggling to keep up with these demands. To address this exponential growth in data traffic, telecom companies are investing heavily in new technologies like fiber-optic networks, and silicon photonics. These technologies offer affordable high-speed data transmission and processing capabilities, enabling telecom companies to provide their customers with faster and more reliable services. They also allow for the integration of optical and electronic components, reducing the size, cost, and complexity of existing systems.

1.2 Silicon photonics

As metal-based electrical interconnects near their performance limits and struggle to keep pace with the surge in data rate demand over the past decade, optical interconnects are being considered as a solution to datacom bottlenecks and high energy consumption. These interconnects use optical signals instead of electrical signals and can replace electrical wires with faster, low-power optical devices in integrated circuits. Silicon photonics has gained significant attention over the years as it offers a solution to numerous applications, including optical communications, sensing, and quantum information processing. **Figure 1.3** shows the evolution and the applications for industrial silicon photonics.

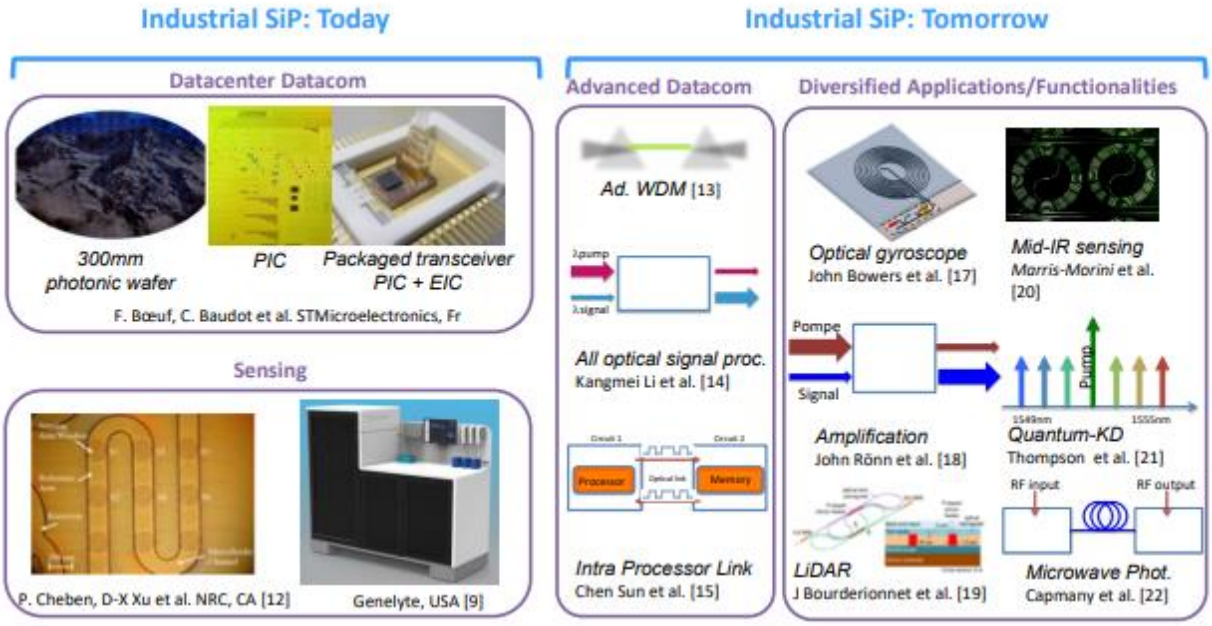

Figure 1.3 The evolution and the applications for industrial silicon photonics. [3]

Silicon possesses several unique optical properties that make it an attractive material for integrated photonics applications. It has a wide transparency window ranging from 1.2 μm to 7 μm and a higher refractive index ($n_{Si} = 3.48$), allowing for more compact optical components design and reducing the device footprint. Most importantly, most of the semiconductor industry uses silicon as the primary material to create integrated CMOS circuits, which makes silicon perfectly suitable to pattern and fabricate photonic devices and circuits and can integrate with other electronics functionalities easily.

The major functionalities that people put effort into silicon photonic development are to emit, transmit, modulate, and detect the light. In this dissertation, we would like to focus on two important physical effects that are widely used in producing many of the active silicon photonics

devices. One is utilizing the nonlinear optical effect and the other is the thermo-optic effect. The following sections will discuss the nonlinear optical effect and the thermo-optic effect, as well as the materials selection, including the advantages and the limitations.

1.2.1 Nonlinear optical effect

Nonlinear photonics is a study of the interaction between the electric field of the optical signal with the materials polarization. When an electric field resonates with electrons in the outer shells of atoms, it gives rise to polarization. The relation between the materials polarization and an electric field can be expressed by a power series [3]:

$$P = \underbrace{\epsilon_0\chi^{(1)}E}_{\text{linear}} + \underbrace{\epsilon_0\chi^{(2)}E^2 + \epsilon_0\chi^{(3)}E^3 + \cdots}_{\text{nonlinear}} \quad (1)$$

where ϵ_0 is the permittivity of free space and $\chi^{(i)}$ are the ith-order optical susceptibilities. The equation describes both the linear and nonlinear relationship between the material polarization and the electric field. Based on this relationship, people have found a number of interesting behaviors that the material can impart upon the optical wave.

Nonlinear studies have mainly focused on the $\chi^{(2)}$ and $\chi^{(3)}$ processes since other higher order susceptibilities are typically small. These processes are demonstrated to be used to amplify, generate, process and sense signals. $\chi^{(2)}$ process demonstrations include the electro-optic effect, which is mainly used in the electro-optic modulators to impose the electrical signal onto the optical wave, and second harmonic generation (SHG), which is a process that generates a new photon with twice the energy of the initial photons and is commonly used to generate green light ($\lambda =$

532 nm) in the industry. Some examples of $\chi^{(3)}$ process demonstrations are third harmonic generation (THG), three photons of frequency ω are annihilated and one photon of frequency 3ω is generated during the process; self-phase modulation (SPM), which leads to an intensity dependent refractive index change; four wave mixing (FWM), where three incident photons generate a fourth photon at an idler frequency; and the stimulated Ramen scattering (SRS), in which an incident pump light can be used to generate a frequency shift radiation called Stokes wave in the process that makes use of the vibrational states of molecules. These processes are the key technologies to optical signal processing.

1.2.2 Thermo-optic effect

The refractive index of an optical material is not a constant over temperature. The measure of the response of the material's refractive index to changes in the temperature is called the thermo-optic coefficient (TOC). The units for TOC are expressed in per degree Centigrade or Kelvin, and the relation can be expressed by the following equation:

$$n(T) = n_0 + \alpha T \tag{2}$$

where α is the TOC of the material. Analysis of the TOC is essential to characterize temperature dependent nonlinear optical devices, optical fiber communication systems and semiconductor technology.

One of the desirable characteristics for integrated photonic applications is tunability and reconfigurability of photonic circuits, which enables reconfigurable photonic devices. Among the various options, the thermo-optic phase shifter has garnered widespread adoption due to its simple design, ease of fabrication, cost-effectiveness, and compact footprint. This makes it a favored

choice for photonic devices and large-scale integrated photonic integrated circuits. In such devices, the thermo-optic phase shifter is employed to manipulate light phase by locally managing temperature within the phase-shifting region. Nevertheless, it is worth mentioning that the modulation bandwidth of the thermo-optic effect is relatively slow, rendering the thermo-optic phase shifter more suitable for applications where high modulation speeds are not essential.

1.3 Photonic Materials: Silicon and Silicon Carbide

Silicon is a mature CMOS material and is one of the most widely used integrated photonic platforms. Several reasons make silicon an attractive candidate for integrated photonics applications. The refractive index of silicon is high (n = 3.48) compared to air (n = 1) or the common cladding material SiO2 (n = 1.45). This enables the strong optical confinement in the waveguide at near-infrared wavelength of 1550 nm which allows compact device footprints down to ten to hundred micrometers. More importantly, with the mature CMOS technology, very low cost, and large-scale integration of many functional devices on a single silicon chip is achievable. Also, the combination of optical devices and electronic devices can also benefit from the compatibility of the CMOS process.

However, there are still challenges in developing silicon photonics devices. The indirect bandgap of silicon prohibits stimulated emission and makes the lasing process less efficient. Also, due to the centrosymmetric structure, silicon lacks a second order nonlinear susceptibility $\chi^{(2)}$, making it challenging for the use in second order nonlinear processes such as SHG and phase modulation. The small bandgap of silicon leads to two-photon absorption and can introduce large nonlinear optical loss at telecommunication wavelengths. Despite these drawbacks, there are still

lots of research efforts focused on the development of nonlinear silicon photonics and great progress has been achieved.

Due to the lack of $\chi^{(2)}$ in silicon which has a centrosymmetric crystal structure, the research on the $\chi^{(2)}$ processes in silicon are mainly focused on two directions: (1) the incorporation of other nonlinear materials, and (2) breaking the crystal symmetry in silicon. Some examples are incorporating another $\chi^{(2)}$ electro-optic nonlinear material as a cladding to realize electro-optic modulation [4-11]. Another method to introduce the $\chi^{(2)}$ in silicon is to deposit a stress layer to strain the silicon waveguide and hence breaks symmetry of the crystal structure [12]. A small linear electro-optic effect is found in strained silicon waveguide [13-15]. However, the upper limit of the effective $\chi^{(2)}$ is estimated to be only 8 ± 3 pm/V. SHG also been demonstrated by using this method [16]. However, the stress induced $\chi^{(2)}$ has proved to be only 0.5 pm/V from the measured conversion efficiency [17].

Silicon has a relatively high $\chi^{(3)}$. The third order nonlinearities are important in silicon as they exhibit many optical processes. One application is applying THG in silicon to generate green light from 1550 nm wavelength laser [18, 19]. SPM will lead to spectral broadening from a pulse spectrum [20] and can be used for supercontinuum generation [21-23]. FWM has been extensively study for the application of wavelength conversion [24-27] and parametric amplification [28, 29]. However, the high intensity nonlinear process will also introduce another effect called two-photon absorption (TPA) in which the photons excite electrons from the valence band to the conduction band. TPA will also cause an intensity dependent α_2 to the linear absorption coefficient as [30]:

$$\alpha = \alpha_0 + \alpha_2 \mathrm{I} \tag{3}$$

where $\alpha_2 = -\frac{3}{2}\frac{\omega}{c^2 n_0^2 \epsilon_0}\mathrm{Im}(\chi^{(3)})$ and I is the intensity of the light. A figure of merit commonly used to compare the materials' nonlinearity and TPA is defined as:

$$\mathrm{FOM} = \frac{1}{\lambda}\frac{n_2}{\alpha_2} \tag{4}$$

where $n_2 = \frac{3}{4}\frac{1}{n_0^2 \epsilon_0 c}\mathrm{Re}(\chi^{(3)})$ is the Kerr nonlinearity. A larger FOM indicates a more efficient nonlinear material. Silicon has a large Kerr nonlinearity. However, the large TPA coefficient results in a low FOM $\cong 0.4$ [31]. Much research on nonlinear optics is to find a material that has a large Kerr nonlinearity and a low TPA coefficient.

The TOC of silicon is as high as $1.8 \times 10^{-4}\mathrm{K}^{-1}$ at 1550 nm at 300K [32]. The high TOC in silicon enables efficient thermo-optic phase shifters [33]. These thermo-optic phase shifters have been applied to many different applications, such as optical neural networks [34], optical phased arrays [35, 36], programmable photonic circuits [37, 38], and quantum photonic devices [39, 40]. On the other hand, due to the high TOC, the thermal fluctuations induced by high-power processes in silicon need to be considered and addressed.

To address the power handling capability in silicon, people started to study the nonlinearity and the TOC of large bandgap material to prevent the loss generated from high intensity processes. As an alternative material, silicon carbide has drawn attention as a new photonic material recently because of its relatively high refractive index, wide bandgap, and large second and third order nonlinearities. The relatively high refractive index of silicon carbide ($n \cong 2.6$) enables high confinement of the optical mode in the waveguide due to high index contrast between it and the common cladding material SiO_2. The wide bandgap (E_g between 2.4 and 3.2 eV [41]) helps to

suppress the TPA, which can limit the nonlinear optical process in the waveguide at telecommunications wavelengths. The large predicted second order nonlinearity ($\chi^{(2)} \cong 30$ pm/V [42]) as well as the large Kerr nonlinearity ($n_2 \cong 6 \times 10^{-19}\ m^2/W$ [43]) make silicon carbide a good candidate as a core material for nonlinear optical processing. In addition, the high thermal stabilities also allow silicon carbide to be less influenced by thermal fluctuation during nonlinear processes at high optical power.

Silicon carbide photonic device demonstrations, such as micro-disk [44-46], ring resonators [47-52], and photonic crystals [53, 54], on 3C, 4H, and 6H crystalline silicon carbide have been reported for many nonlinear applications, such as four-wave mixing [43, 51], second harmonic generation [50, 53, 54], self-phase modulation [55], and parametric oscillation [52]. However, because the index of silicon carbide is lower than that of silicon, the silicon carbide device layers may be suspended to prevent the optical mode from leaking into the silicon substrate [44, 49], or use smart-cut techniques [55, 56] to form silicon-carbide-on-insulator (SICOI) platforms. Both methods include rather complicated fabrication steps.

Silicon carbide has outstanding thermal stability. Therefore, it has a relatively low TOC. The TOC of stoichiometric silicon carbide is $2.67 \times 10^{-5}\ ℃^{-1}$ [57] which is almost one order of magnitude lower than that of silicon, leading to less competitive thermal tuning properties. The lower TOC and lower refractive index cause stoichiometric SiC-based devices to have higher power consumption and larger device footprints.

Instead of crystalline silicon carbide, amorphous silicon carbide (a-SiC) has also been proposed as a photonic material since the fabrication process is relatively simple compared to crystalline silicon carbide [58-65]. A high quality factor (Q) a-SiC ring resonator has been

demonstrated using plasma-enhanced chemical vapor deposition (PECVD) as a growth technique [59]. The low temperature PECVD process is a CMOS available process. The easy material properties tunability is also a favor characteristic. Higher Kerr nonlinearity is also found in a-SiC to be 4.8×10^{-18} m^2/W which is still one order of magnitude lower than amorphous silicon (a-Si).

Taking advantage of the easy tunability of the deposition process, we propose a material that lies between a-SiC and a-Si, namely silicon rich a-SiC. By tuning the deposition condition, we can control the properties of silicon rich a-SiC leading to the material property advantages of both sides. The new material could possibly have higher nonlinearities and higher TOC while maintaining a wide enough bandgap to provide better power handling capabilities.

1.4 Thesis outline

This dissertation discusses our efforts in developing silicon rich a-SiC as a new material for integrated photonics applications. It starts from the materials preparation, materials characterization and waveguide design, fabrication, and characterization. Finally, the two important elements in the photonic circuit, thermo-optic phase shifter and electro-optic modulator are proposed, designed, fabricated, and characterized to demonstrate the feasibility of silicon rich a-SiC as a new photonic material for integrated photonics.

In Chapter 2, we cover the preparation of the silicon rich a-SiC thin film by using PECVD. Different precursor ratios are applied to the deposition chamber to form SiC thin films with different silicon atomic ratio. The thin films with different stoichiometries are studied to explore the relationship between the silicon content and the materials properties.

In Chapter3, we discuss the silicon rich a-SiC waveguide design and fabrication. The loss of the waveguide is then estimated from the transmission spectrum of the ring resonators. Finally, an enhancement of $\chi^{(3)}$ in the material and the induced $\chi^{(2)}$ is demonstrated using DC Kerr effect. A comparison of the materials using similar techniques will also be discussed.

In Chapter 4, we show our work to characterize the TOC of the silicon carbide with different stoichiometry and demonstrate an enhancement in the TOC as the silicon content increased in the film. Next, we demonstrate efficient micro-ring thermo-optic phase shifter by integrating NiCr heater with silicon rich a-SiC ring waveguides.

In Chapter 5, we propose a Si/SiC hybrid waveguide DC Kerr effect modulator. We will show our effort in design, fabrication, and characterization of the device. Including the passive and the active structures. Finally, in Chapter 6 we conclude with areas of future research.

CHAPTER 2: SILICON RICH SILICON CARBIDE MATERIAL PREPARATION AND CHARACTERIZATION

2.1 Introduction

Silicon has been extensively studied as a photonic material for both linear and nonlinear optical processes. Large transparent windows in the telecommunications wavelengths, large index contrast between silica, and the compatibility to complementary metal oxide semiconductor (CMOS) processing make silicon potentially suitable for many photonic applications [30]. However, silicon lacks a second order nonlinear susceptibility $\chi^{(2)}$, due to the centrosymmetric structure, and possesses a relatively small bandgap making it challenging for use in second order nonlinear processes, such as second harmonic generation (SHG) and phase modulation. Although past efforts have demonstrated that depositing silicon nitride to strain the silicon and break the crystal symmetry [15, 17], the induced $\chi^{(2)}$ is relatively small. More recently, demonstrations of using a DC electric field to break the symmetry has proved to be a more effective means to induce a large $\chi^{(2)}$ [66-68]. This has enabled the DC Kerr effect in silicon, which perturbs the material's electric permittivity and introduces a phase shift of lightwave. However, the breakdown voltage for silicon is relatively low, which limits the induced $\chi^{(2)}$.

As a new alternative photonic material, silicon carbide has drawn considerable recently because of its relatively high refractive index, wide bandgap, and large second and third order nonlinearities. The relatively high refractive index of silicon carbide ($n \cong 2.6$ [69]) enables high confinement of the optical mode in the waveguide due to high index contrast between it and the common cladding material SiO_2 ($n \cong 1.45$). The high bandgap (E_g between 2.4 and 3.2 eV [41])

helps to suppress two-photon absorption, which can limit the nonlinear optical process in the waveguide at telecommunications wavelengths. The large predicted second order nonlinearity ($\chi^{(2)} \cong 30$ pm/V [42]) as well as the large Kerr nonlinearity $\chi^{(3)} \cong 6 \times 10^{-19}$ m^{2}W [43]) make silicon carbide a good candidate material for nonlinear optical process. In addition, the high thermal stabilities also allow silicon carbide to be less influenced by thermal fluctuation during nonlinear processes at high optical power. Moreover, silicon carbide has a higher dielectric strength compared with silicon, which makes silicon carbide very suitable for this electric field induced $\chi^{(2)}$ process.

In this chapter, I will discuss the preparation of silicon carbide by using PECVD. Silicon carbide thin films with different stoichiometry are prepared using different precursor ratios and the materials properties are characterized in the relation to the silicon content in the film.

2.2 Silicon carbide deposition

The silicon carbide thin film is prepared using the Oxford Plasmalab PECVD system, which utilizes plasma to facilitate growth. The plasma discharge ionizes the gases, generating active species that react with the surface of the wafer. **Figure 2.1** depicts the configuration of the PECVD chamber, featuring a top electrode RF (MHz/KHz) driven plasma that promotes deposition at lower temperatures compared to LPCVD methods. The process involves positioning the substrate on a heated bottom electrode, while precursor gases are introduced through a "showerhead" gas inlet in the top electrode.

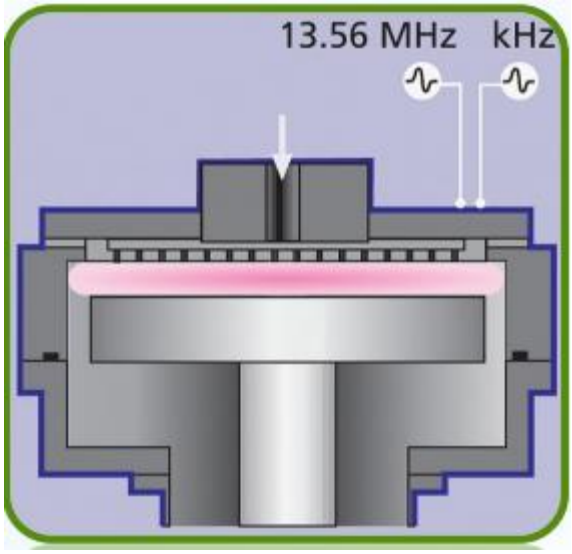

Figure 2.1 Schematic of the PECVD (Oxford Plasmalab PECVD) system used to deposit the SiC films.

In this work, around 300 nm thick silicon carbide thin films are deposited onto 1cm-by-1cm silica on Si substrates. The deposition process employs a gas mixture of silane (SiH_4) and methane (CH_4) as precursors, with a chamber pressure set at 1000 mTorr. To form different stoichiometric SiC compositions, different gas flow ratios are applied. The temperature is maintained at 350 ℃, and the power at 20W throughout the process.

The thin film thickness is measured by using J.A. Woollam M-2000D Ellipsometer. Five spots are measured on the 1cm-by-1cm sample. **Figure 2.2 (a)** shows the relative location of the ellipsometry measurement points. The laser beam size is 3 mm in diameter, and we move the stage by 1.5 mm for each step. The results show that the deposition rate is quite uniform throughout the chip. With the average film thickness around 300 nm, there is a less than 5 nm thickness difference between the center and the edge for all the composition we investigated. **Figure 2.2 (b)** shows the

thickness measurement results for different stoichiometric films. From the picture of sample in **Figure 2.2 (c)**, we can also visualize roughly a uniform deposition from the color of the chip. Another thing to be noted: the deposition rate of the silicon carbide film is slightly different for different precursor flow ratios. The deposition rate ranges from 7.46 nm/min at the lowest SiH_4/CH_4 flow ratio to 8.65 nm/min at the highest SiH_4/CH_4 flow ratio.

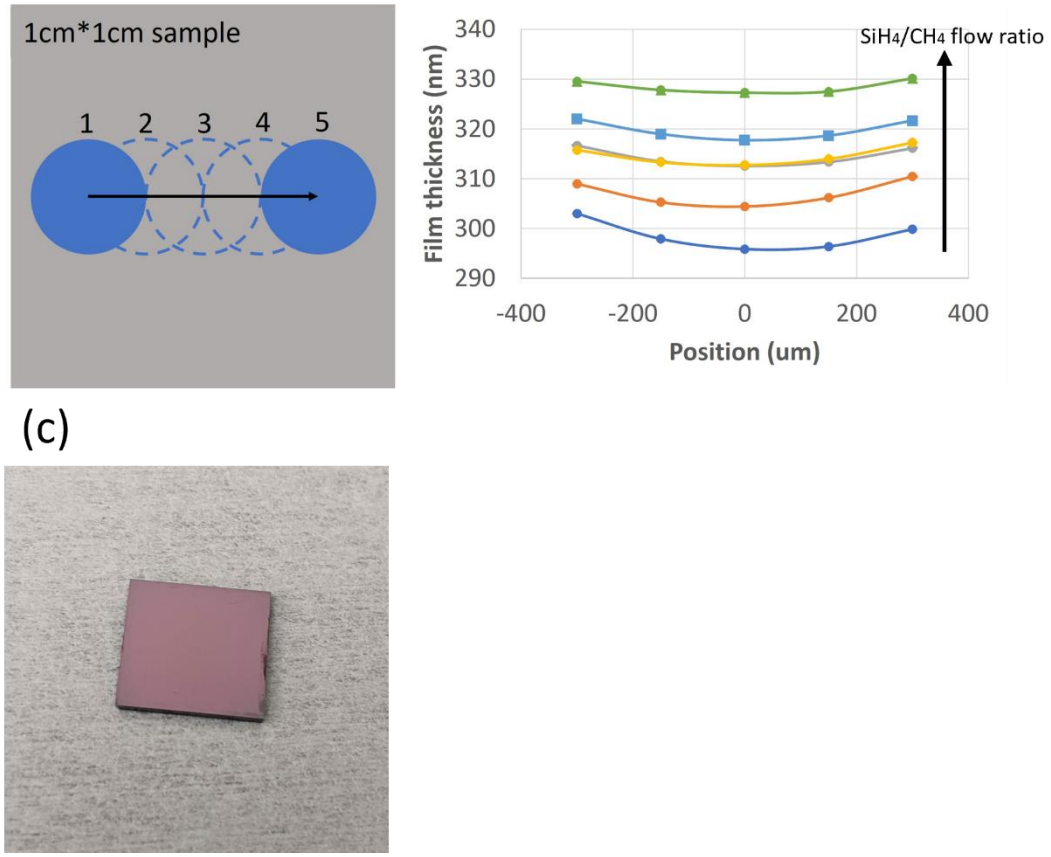

Figure 2.2 (a) Schematic of the ellipsometry measurement points on a 1cm-by-1cm sample. (b) Thickness measurement results for different stoichiometric silicon carbide thin films. (c) A picture of a 1cm-by-1cm sample with uniform silicon carbide thin film deposition.

2.3 Characterization of the SiC thin films properties

2.3.1 Materials refractive index

The material refractive index is an important optical property of a material. The real part of the refractive index describes the phase of the light propagating in the medium and the imaginary part of the refractive index describes the loss the light in the medium. They are critical parameters in designing optical waveguides. It is important to study how the precursor flow ratio affects the refractive index of the thin film.

The material refractive index is characterized by J.A. Woollam M-2000D Ellipsometer. Ellipsometry measures a change in polarization as light reflects or transmits from a material structure. The polarization change is represented as an amplitude ratio and the phase difference. The measured response depends on optical properties and thickness of individual materials. **Figure 2.3** shows the results of ellipsometer measurements from 200 to 1000 nm. We can see that as the SiH_4/CH_4 flow ratio increases, the real part of the refractive index, n, of the film gets higher. It is also clearly visible that the imaginary part of the index, k, which is a measure of the optical loss of the SiC film, is negligible when the wavelength is larger than 700 nm for all the layer compositions investigated.

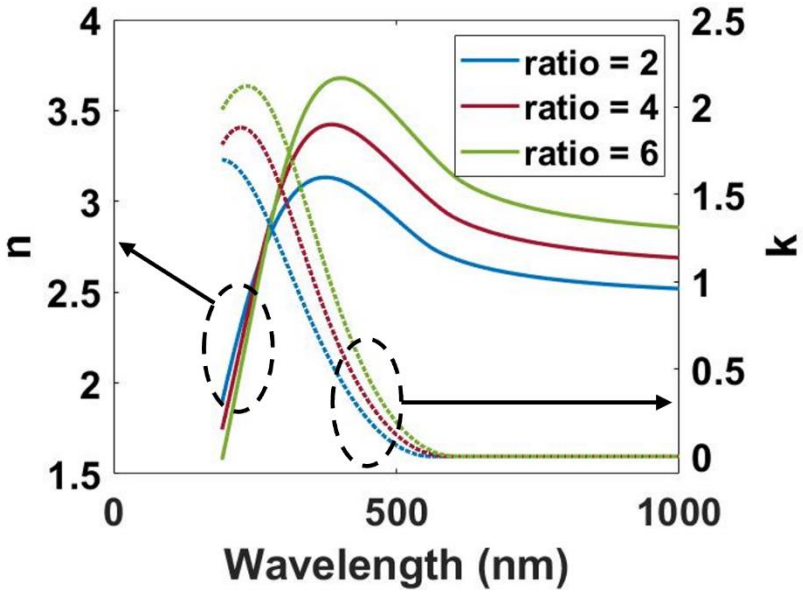

Figure 2.3 Ellipsometer measurements for the real part and the imaginary part of the index for three films with different gas flow ratio of SiH_4/CH_4.

2.3.2 Surface roughness

The surface roughness of the thin film is an important parameter that affects the waveguide propagation loss. The surface roughness of the thin film is characterized by the AFM system (Veeco Scanning Probe Microscope). **Figure 2.4** shows the AFM scans of ~300 nm thick silicon carbide thin films. The measurement of root mean square (RMS) surface roughness of the thin film with different SiH_4/Ch_4 flow rate within a 5 um by 5 um scan area are 0.2 nm, 0.35 nm and 0.7 nm respectively. The results show an increase in the surface roughness as the silicon content increases in the film. With the highest 0.7 nm RMS surface roughness, we can estimate the scattering loss from the waveguide side wall to be on the order of 0.37 dB/cm [70]. If the waveguide is operated in transverse electric (TE) modes, the loss generated from the top surface could be even lower.

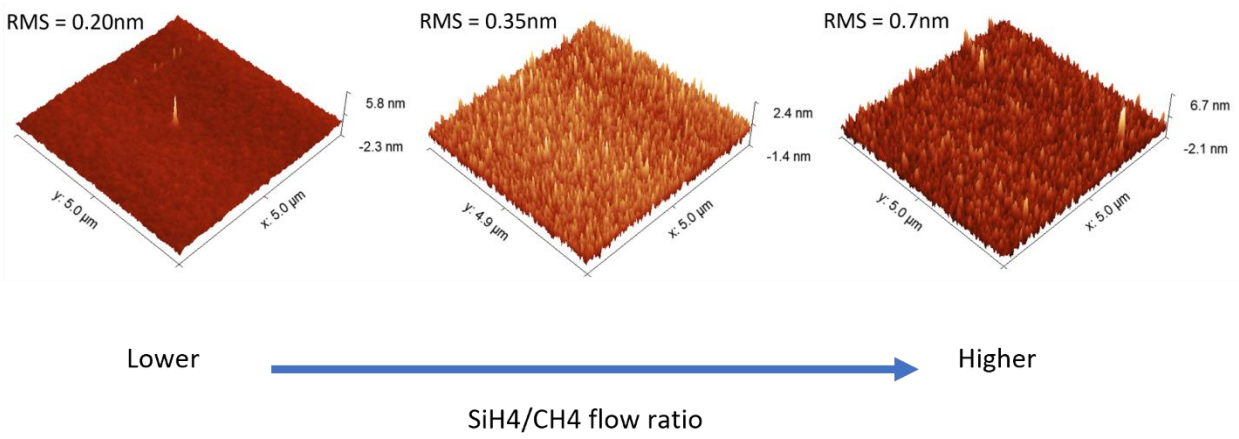

Figure 2.4 AFM images of the silicon carbide thin films with different stoichiometry. The scanning area is 3 μm by 3μm. The RMS surface roughness measured are 0.2 pm, 0.35 pm and 0.7 pm respectively.

2.3.3 Band gap

Band gap energy is an important factor to evaluate the nonlinear optical loss. The main contributor of the nonlinear optical loss at high optical power is TPA. It is a process where the material absorbs two photons simultaneously and excites the electron to the higher energy state. This process normally happens in the nonlinear process that operates in high optical intensity. To avoid two-photon absorption, it requires the bandgap of the materials to be larger than two times of the photon energy at the operating wavelength.

The band gap of the materials is estimated by fitting the ellipsometry measurements data using the Tauc-Laurantz model. **Figure 2.5** shows the calculated band gap energy of the silicon carbide films that we investigated. We observed an inverse relation between the band gap energy and the refractive index of the thin films in this series. One thing to note is that even with the highest refractive index film, the band gap energy is still larger than 2 eV. The result indicates that

our silicon rich a-SiC films will have limited two-photon absorption for photons at 1550 nm wavelength which corresponds to photon energy of 0.8 eV.

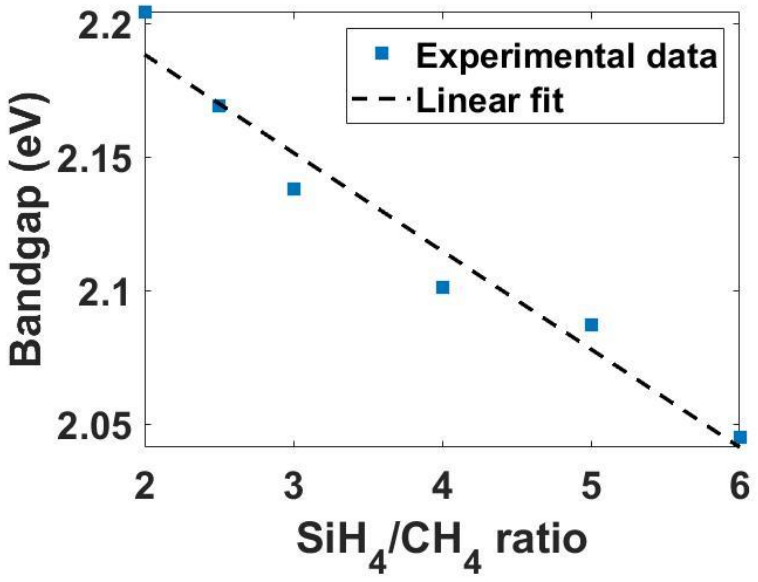

Figure 2.5 Band gap energy of the silicon carbide thin films with different precursor flow ratio.

2.3.4 Atomic composition

In order to further confirm the relationship of silicon content and the materials refractive index, the energy-dispersive x-ray spectroscopy (EDX) measurements are carried out to determine the atomic composition of each film. The measurements confirm that with the higher SiH_4/CH_4 flow ratio, the silicon content increases. This also confirms that as the thin film's silicon mole fraction increases, the refractive index of the film goes up. **Figure 2.6** shows the EDX measurement for the film with highest silicon content. The atomic composition of silicon and carbon for the film is estimated to be 77.1% and 19.4%. This indicates that the film is $Si_{0.8}C_{0.2}$.

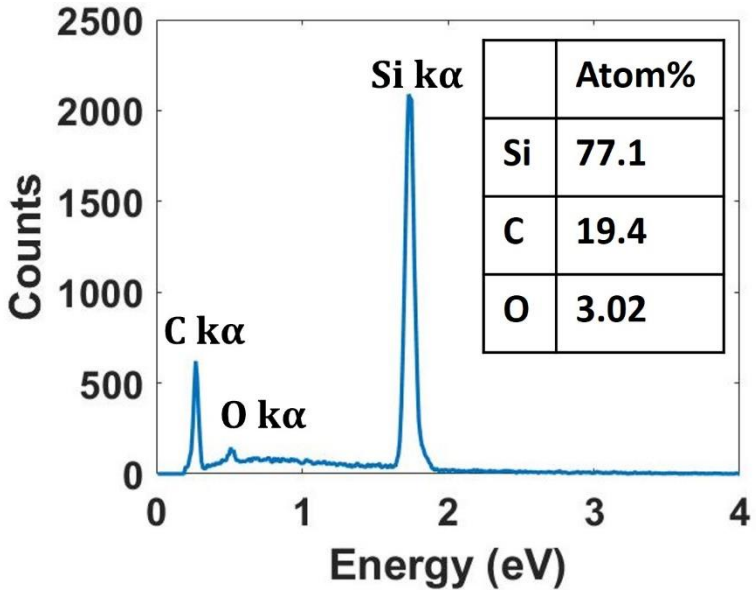

Figure 2.6 EDX spectra showing the composition of the film with the highest silicon content. The atomic ratio showing that the film is $Si_{0.8}C_{0.2}$.

2.3.5 Permittivity and breakdown electric field

In order to characterize the breakdown electric field of the material, which is a crucial parameter for the DC Kerr effect measurement, we made circular capacitors with a 100 nm thick silicon rich a-SiC film sandwiched between the highly doped silicon substrate and gold pads with diameter ranging from 200 µm to 300 µm. **Figure 2.7** shows the schematic of the capacitor structures. The circular capacitors minimize the electric field concentration at the corner and hence preclude the chance of unwanted breakdown happening at the edge of the structures.

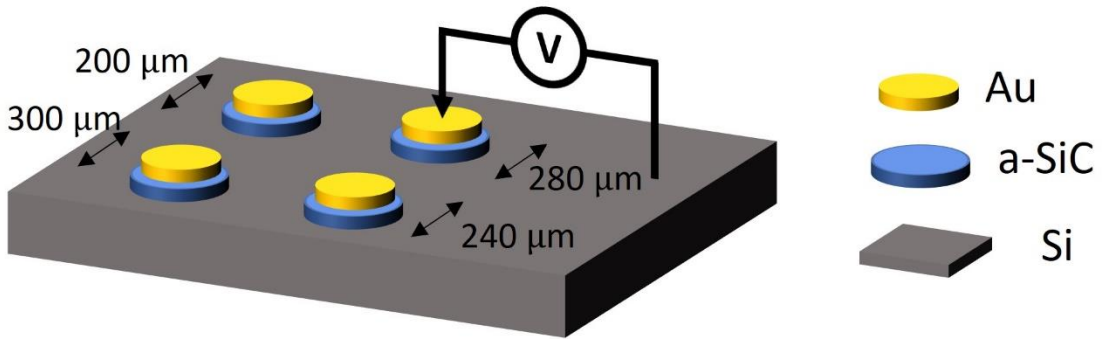

Figure 2.7 Schematic of the round shaped capacitors with different diameters.

I–V measurements are carried out by an Agilent B1500A Semiconductor Device Analyzer. The measured I-V data were converted to current density-V data by divided by capacitor areas. We can observe that the curves with different diameters (for a given flow ratio) overlap, and this confirms that the breakdown is predominant from the bulk material not from the edge. Because if the edge breaks down happens, the leakage current will depend on the radius rather than the area of the capacitors.

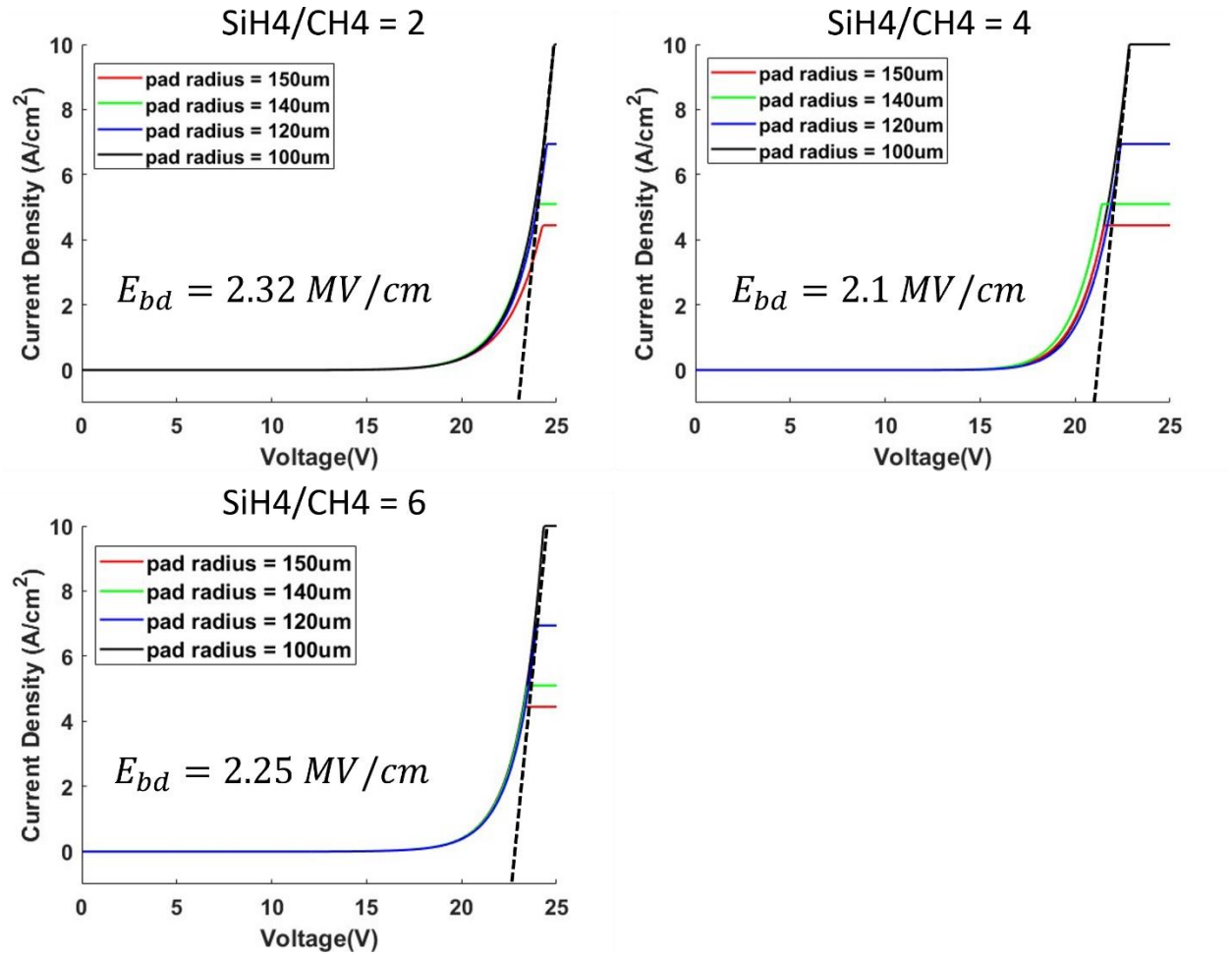

Figure 2.8 J–V characteristic of the capacitor showing the breakdown electric field for the a-SiC thin film deposited with three different precursor flow ratios. The measured breakdown electric fields for the three films are 2.32 V/cm, 2.1 V/cm, and 2.25 V/cm, respectively.

We observed a big increase in the leakage current as the applied voltage is raised between 21 V and 23 V for the three films investigated. This implies that the breakdown electric field for the materials are around 2.2×10^6 V/cm, which is within the same order of magnitude as that of stoichiometric a-SiC ($E_{bd} \cong 3 \times 10^6$ V/cm [71]) and an order of magnitude higher than crystalline silicon ($E_{bd} \cong 2.5 \times 10^5$ V/cm [72]). The higher breakdown electric field implies that a-SiC has the potential for utilizing DC Kerr effect to achieve higher induced $\chi^{(2)}$.

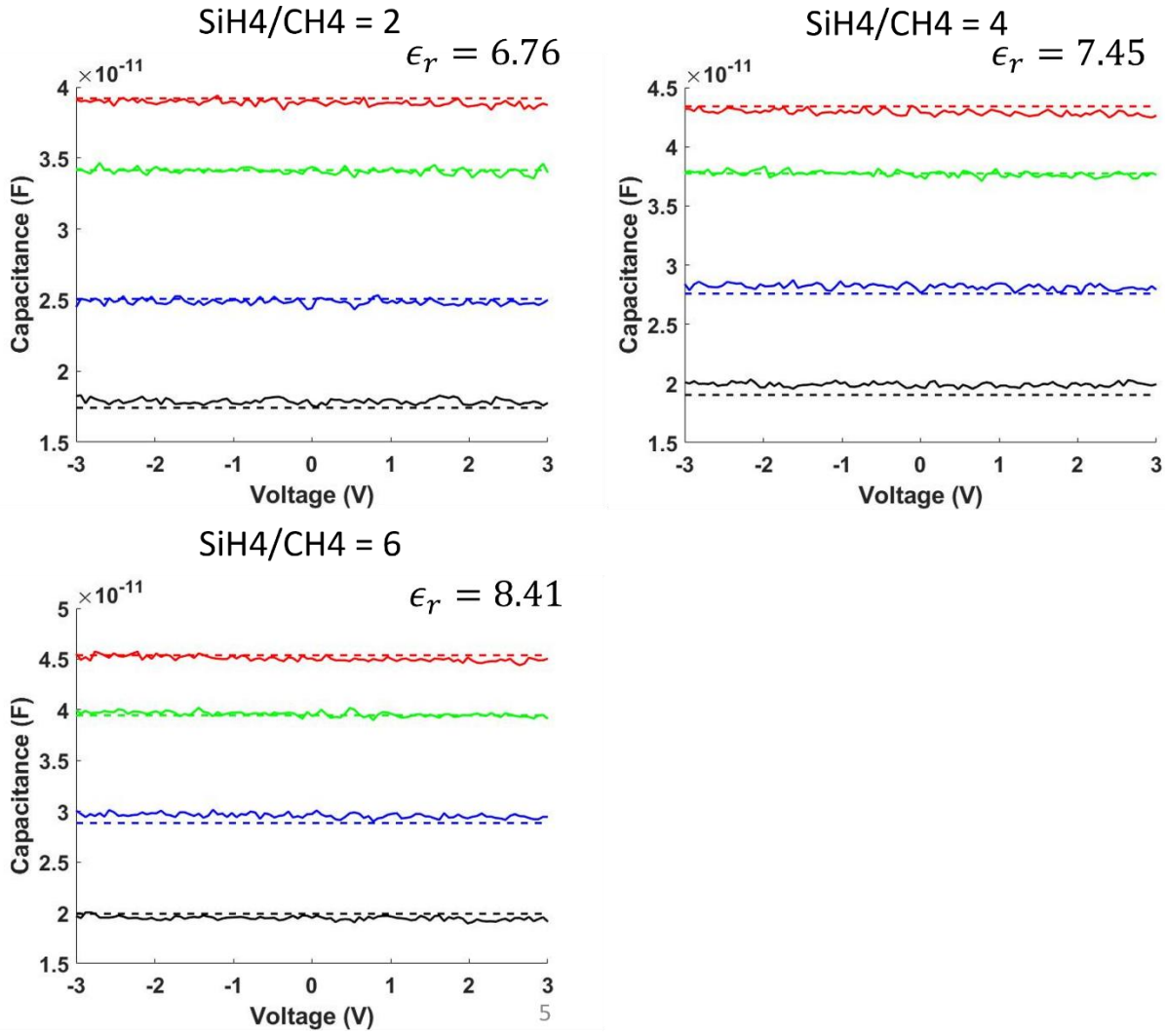

Figure 2.9 C-V measurement at 1 MHz along with the fittings for the relative permittivity for the a-SiC thin film deposited with three different precursor flow ratios.

The C-V measurements were also performed to study the materials permittivity as the lower the materials permittivity we have a higher chance to achieve higher device speed. The capacitance of the devices is measured in the same setup as shown in **Figure 2.7**. From **Figure 2.9**, we can find that the capacitance increases as the silicon content increases. We fit the capacitance for the four capacitors with different diameters simultaneously to extract the

permittivity of the film. The fittings are shown as dot lines in the figure. We confirm that the permittivity is about the linear refractive index squared. Also, we know that even if we increase the linear refractive index, the film still exhibits relatively low permittivity.

2.4 Conclusion

In conclusion, our study demonstrates the tunability of silicon carbide material deposition through the use of PECVD. By employing different precursor gas flow ratios, we have successfully obtained thin films with varying stoichiometry. A detailed characterization of the materials properties has been performed to investigate their correlation with the silicon content in the film. We found that a smooth and uniform deposition can be achieved, which is crucial for better loss control. Moreover, we have observed an inverse relationship between the band gap and the refractive index. Even with the most silicon-rich film, the band gap remains sufficiently large to reduce two-photon absorption. Furthermore, the breakdown electric field and permittivity have been determined through the characterization of the J-V and C-V behavior of a parallel plate structure. Understanding these materials properties provides valuable insights to aid in the design of optical devices for further investigation of materials' nonlinearity.

Chapter 2, in part, is a reprint of the materials as it appears in Applied Physics Letters 2022. Li-Yang Sunny Chang, Hani Nejadriahi, Steve Pappert, and Paul K. L. Yu. The dissertation author is the primary investigator and author of this paper.

CHAPTER 3: THIRD ORDER SUSCEPTIBILITY ENHANCEMENT IN SILICON RICH SILICON CARBIDE

3.1 Introduction

Stoichiometric amorphous silicon carbide exhibits some unusual optical properties that makes it an excellent material for integrated photonics applications. Its wider band gap effectively eliminates two-photon absorption, rendering it highly suitable for high-intensity nonlinear photonic devices. However, it is worth noting that the reported nonlinearity in silicon carbide is currently one order of magnitude lower than that of silicon, which can limit its efficiency in nonlinear optical processes.

To address this limitation, we have explored the potential of leveraging both silicon and silicon carbide advantages through the controllable deposition conditions in PECVD. By increasing the silicon content in the amorphous silicon carbide film, we aim to enhance the nonlinearity while retaining a sufficiently wide band gap to mitigate two-photon absorption effects. This approach offers a promising pathway to augment the performance of silicon carbide for nonlinear optical applications.

In the first part of the chapter, I will discuss our effort in the design and demonstration of the silicon rich carbide waveguide. The waveguide propagation loss is estimated by measuring the transmission spectrum of the ring resonators. In the second part of the chapter, I will elaborate on our efforts to demonstrate the DC Kerr effect in the waveguide consisting of a silicon rich amorphous silicon carbide (a-SiC) layer. Notably, we have observed an enhancement of third-order nonlinearity $\chi^{(3)}$ and induced second-order nonlinearity $\chi_{\text{eff}}^{(2)}$ in silicon-rich a-SiC.

3.2 Amorphous silicon carbide waveguide design and fabrication

To further investigate the nonlinearity of the silicon rich a-SiC films, we design and fabricate optical waveguides. The waveguide geometry is first modeled by the Finite Difference Eigenmode (FDE) solver built in Lumerical MODE solution. **Figure 3.1(a)–(c)** shows the effective index of the optical mode in different waveguide geometries. The orange lines represent the transverse electric (TE) modes, and the green lines represent the transverse magnetic (TM) modes supported in the waveguide. The vertical dashed line represents the cut-off of the waveguide width that delineates single mode or multimode operation. **Figure 3.1(d)** illustrates the simulated mode profile. In consideration of single mode operation and a comfortable fabrication tolerance, we decided to design the waveguide to have around 300 nm in height and 850 – 900 nm in width.

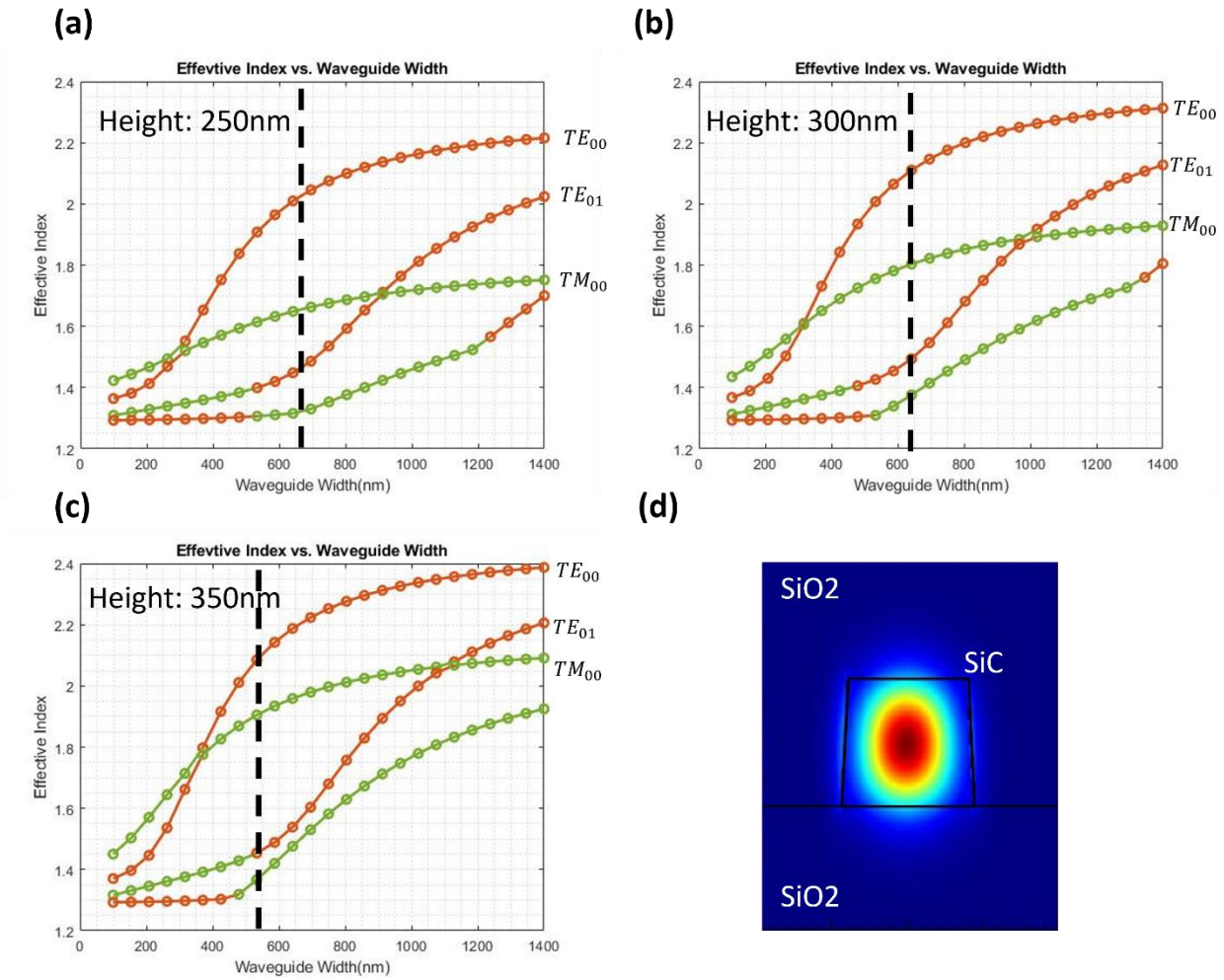

Figure 3.1 (a) – (c)The FDE simulation of effective index of the optical mode in different waveguide geometries. (d) Simulate optical mode profile.

Ring resonators with bus and ring waveguides separated by a coupling gap are then fabricated to determine the propagation loss of the waveguide. The transmission spectrum of the designed resonators is then calculated using MATLAB. The ring radius is 50 μm, and the coupling gap between the bus and the ring waveguides ranges from 100 to 400 nm. The light is coupled in and out of the bus waveguide using edge couplers that are designed and optimized using finite-

difference time-domain (FDTD) method built-in Lumerical to achieve the maximum coupling efficiency to the fundamental TE-polarized mode at 1550 nm.

The fabrication steps for the waveguides are shown in **Figure 3.2**. The process starts with the deposition of around 320 nm of silicon rich a-SiC on 3 μm thermal oxide on the silicon substrate. The waveguides are designed and patterned by electron beam lithography. In the process, 600 nm of FOX16 negative E-beam resist is spin-coated and hard baked on the a-Si film. Patterns are transferred by electron beam lithography followed by reactive ion etching (RIE). a-SiC is etched using a gas mixture of 35 sccm CHF_3 and 10 sccm O_2 with the 30 mTorr chamber pressure and under 150W of RF power. The etch rate is around 20 nm/min. The bottom electrode is formed by the lift off process. It is first patterned using NR9–3000 negative resist and Heidelberg MLA150 maskless aligner. A 350 nm layer of gold is then deposited by the Denton 18 sputter system. The gap size between the electrodes is 2.9 μm. A 2 μm thick silicon dioxide cladding layer is then deposited using Oxford PlasmaLab PECVD. Vias are patterned by AZ1518 positive resist and MLA150 and then opened by buffered oxide etch (BOE) to yield a sloped sidewall. 500 nm of a contact pad is formed using the lift off process again. Finally, focused ion beam (FIB) is used to mill the end surface of the input and output tapers to improve the coupling efficiency. **Figures 3.3 (a)** and **Figure 3.3 (b)** show the scanning electron microscope (SEM) images of the top view of the ring resonator with 200 nm of coupling gap and the cross section of the coupling region before encapsulated by silicon dioxide. We observed an 80-degree etching profile from the cross-section view. The FDE model is then updated for the slope to calculate the effective index for more accuracy to the real case. **Figure 3.3 (c)** is the optical microscope (OM) image of the top view after depositing the electrode and contact pad.

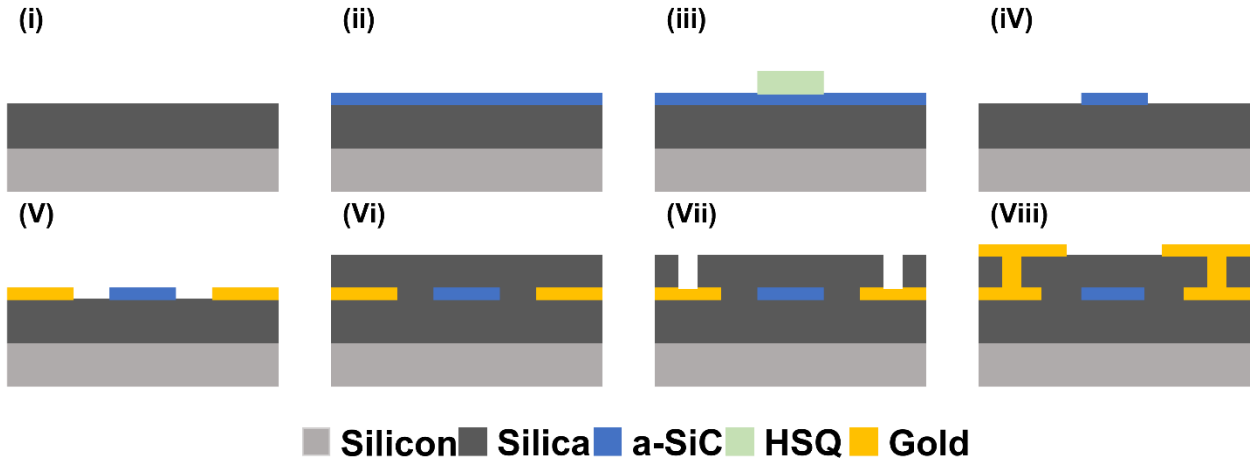

Figure 3.2 (a) Schematic of process flow for the fabrication of ring resonators. (i)–(iv) a-SiC waveguide formation. (v) Bottom electrode formation. (vi) SiO2 cladding deposition. (vii) Vias formation. (viii) Contact pad formation.

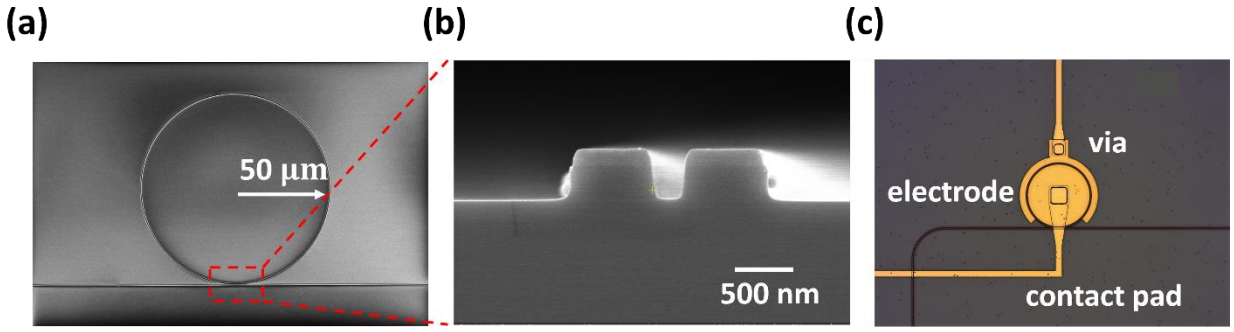

Figure 3.3 The SEM image of the (a) cross section and (b) top view of the ring resonators with HSQ remaining on top of the waveguide. (c) Optical microscope image of the ring device with the electrode

3.2.1 Ring waveguide measurement and analysis

The transmission spectra of the ring resonator are measured by the setup shown in **Figure 3.4**. A CW wavelength-tunable laser (from 1465 nm to 1575 nm) is applied through a single mode fiber (SMF), an Erbium-Doped Fiber Amplifier (EDFA) is used to enhance the optical power, and a polarization controller is used to maintain the TE-polarized mode in the waveguide. The laser is fiber coupled to the ring resonators through a lensed fiber. An objective lens collimated the light transmitted through the device and was filtered by a polarizing crystal before being detected by a photodetector (PD) and a CCD camera. The PD was connected to a data acquisition (DAQ) system to record the results. All the samples are mounted onto a stage with temperature controlled by a thermo-electric cooler (TEC) module.

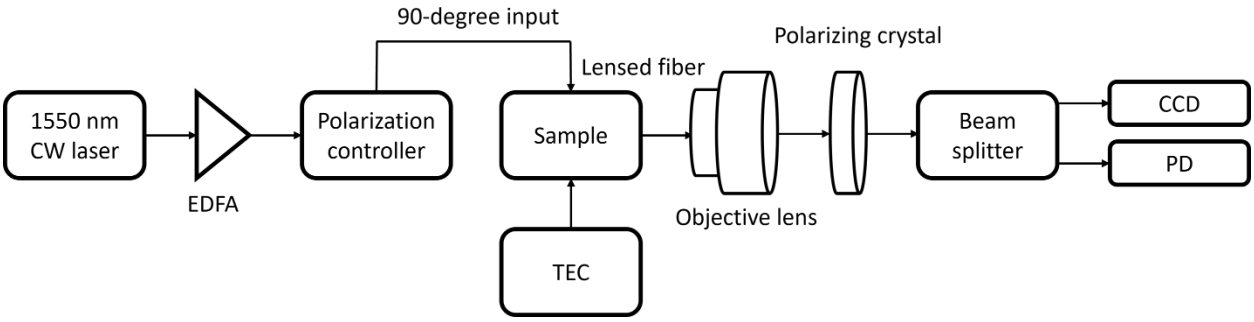

Figure 3.4 The block diagram of the test setup.

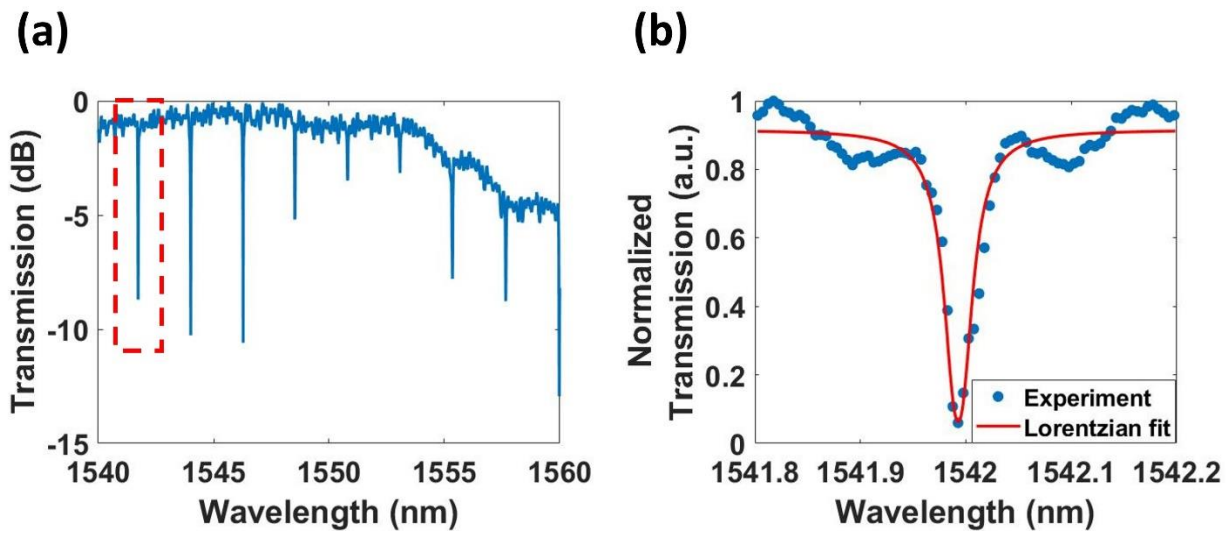

Figure 3.5 (a) Multiple resonances and (b) zoom-in single resonance at 1542 nm with the Lorentzian fit of the passive transmission spectra of a ring resonator with 200 nm of ring and bus waveguide separation for TE polarized mode.

The transmission spectrum of the ring resonator is shown in **Figure 3.5 (a)**. We confirm the single mode propagation from the transmission spectrum since there is no multiple resonance from higher order modes. The free spectral range (FSR) is measured to be 2.27 nm, and the corresponding group index can be calculated to be around 3.38 using the equation:

$$n_g = \frac{\lambda^2}{2\pi R \times FSR} \tag{5}$$

where R is the radius of the ring. The quality factor of the ring resonator is extracted from the Lorentzian of the transmission spectra. **Figure 3.5 (b)** shows the single resonance at 1542 nm with the Lorentzian fit function. The loaded quality factor can be calculated from the equation:

$$Q_L = \frac{\lambda}{\Delta\lambda} \tag{6}$$

where $\Delta\lambda$ is the full width at half maximum (FWHM), and the intrinsic quality factor can be calculated from:

$$Q_i = \frac{2Q_L}{1 + \sqrt{T}} \tag{7}$$

where T is the transmission at the resonance. The Q_L and Q_i for our ring resonators are extracted to be ~68 000 and 96 000, respectively. The corresponding propagation loss for TE-polarized mode of the waveguide can be derived by:

$$\alpha = \frac{2\pi n_g}{Q_i \lambda} \tag{8}$$

and the loss is estimated to be 6.2 dB/cm, which is higher than the best reported value for stoichiometric a-SiC ($\alpha \cong 4.2\ \mathrm{dB/cm}$) [59]. From a cut back loss measurement of 2 μm wide waveguides, the higher loss was attributable to the sidewall scattering loss (>3 dB/cm), which can be improved by optimizing the fabrication process, including using a finer mask, fine tuning the etching chemistry and annealing. These approaches can reduce the sidewall surface roughness.

3.2.2 Edge coupler

Since we have a nano dimension waveguide (~300 nm × 900 nm), the mode mismatch between the lensed fiber (radius ≅ 2.5 μm) and the waveguide is very large, it will introduce a high fiber to waveguide coupling loss for the measurement. It is necessary to design an edge

coupler to reduce the insertion loss. The laser light will be coupled in and out of the waveguide using edge couplers.

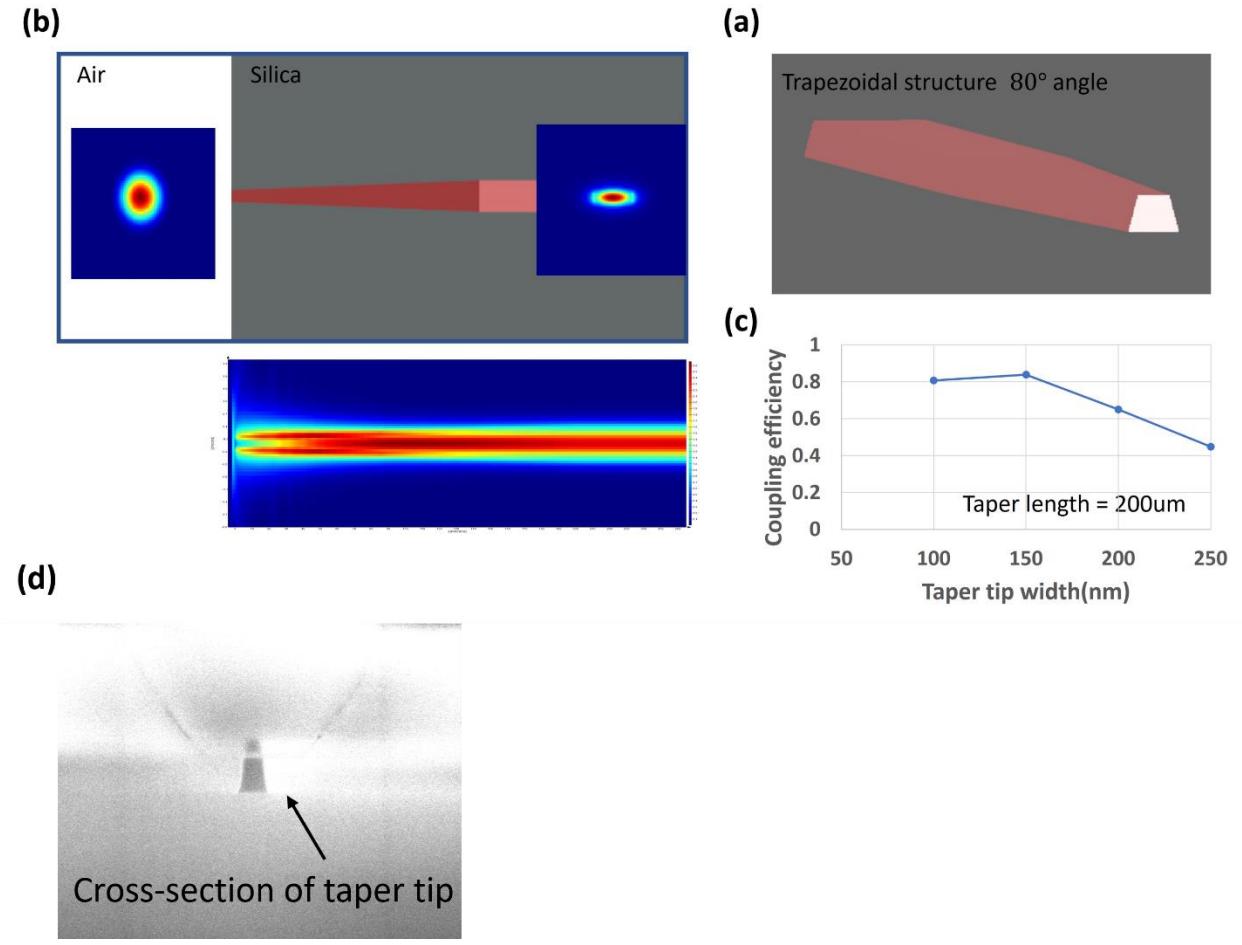

Figure 3.6 (a) 3D structure of the taper. (b) Top view of the taper and the simulated electric field profile along the taper structure (c) FDTD simulation result of the coupling efficiency to the taper tip width. (d) SEM image of the cross-section of the taper tip.

We used the FDTD solver built in Lumerical to design the edge coupler. In the model, we create a 200 μm tapered waveguide with a side wall angle of 80° which is close to the etching profile observed under SEM. The 3-dimensional structure of the taper waveguide and the SEM

image of the cross-section of the fabricated taper tip are shown in **Figure 3.6 (a)** and **Figure 3.6 (d)** respectively.

Figure 3.6 (b) is the top view of the taper. The input light (left) is the fundamental TE-polarized laser mode coupled from a lensed fiber and the output is the propagating mode after the transition from the taper region. The bottom is the simulated electric field of the propagating mode along the taper. A gradual transition of the fiber mode to a waveguide mode is observed. A plot of coupling efficiency versus taper tip width is shown in **Figure 3.6 (c)**. It indicates that a taper tip width of 150 nm provides the maximum coupling efficiency of 84%.

3.3 DC Kerr effect

After designing silicon rich carbide optical waveguides and characterizing the loss of the waveguide, the next step is to design an experiment to extract the nonlinearity of the materials. We utilize a nonlinear optical process called DC Kerr effect or quadratic electro-optic Kerr effect to extract the materials' nonlinearity. In the following, we will discuss the theory of the DC Kerr effect and the experiment to extract the materials' nonlinearity.

3.3.1 Theory and equation derivation

The DC Kerr effect is the effective $\chi^{(2)}$ process that can be derived from a material exhibiting $\chi^{(3)}$. An asymmetry can be introduced by electric field because the dipole moments tend to orient themselves in the direction of the applied field. Through this process, the third-order nonlinearity $\chi^{(3)}$ is converted to $\chi^{(2)}$. The field-induced $\chi^{(2)}$can perturb the electric permittivity and introduce a phase shift. By measuring the transmission spectrum of a ring resonator, we can

extract the resonance shift before and after applied the voltage across. It can then be used to back calculate the $\chi^{(3)}$ and the effective $\chi^{(2)}$.

The following is a derivation of the relationship between the refractive index change to the applied electric field. We will use it to extract the $\chi^{(3)}$ from the measurement results. The relationship between material's $\chi^{(3)}$ and the effective $\chi^{(2)}_{\text{eff}}$ introduced by the DC Kerr effect is also derived.

The power expansion of the polarization for a medium in the presence of an electric field can be described as [3]:

$$\mathrm{P}(\mathrm{t}) = \epsilon_0\left(\chi^{(1)}\mathrm{E}(\mathrm{t}) + \chi^{(2)}\mathrm{E}^2(\mathrm{t}) + \chi^{(3)}\mathrm{E}^3(\mathrm{t}) + \cdots\right) \tag{9}$$

where P is the material polarization, ϵ_0 is the vacuum permittivity and E is the electric field. The electric field included in the DC Kerr effect process is the DC electric field and the incident optical field, which can be expressed as:

$$\mathrm{E}(\mathrm{t}) = \mathrm{E}_{\mathrm{DC}} + \mathrm{E}_{\omega}\cos(\omega \mathrm{t}) \tag{10}$$

If we plug the electric field into **Equation (9)**, we can find the nonlinear polarization that is related to the incident frequency $\mathrm{E}_{\omega}\cos(\omega \mathrm{t})$ can be expressed as follows:

$$\mathrm{P}_{\mathrm{DC\ Kerr}} = 3\epsilon_0\chi^{(3)}\mathrm{E}_{\mathrm{DC}}^2\mathrm{E}_{\omega}\cos(\omega \mathrm{t}) \tag{11}$$

$$\mathrm{P}_{\mathrm{Electrooptic}} = 2\epsilon_0\chi^{(2)}\mathrm{E}_{\mathrm{DC}}\mathrm{E}_{\omega}\cos(\omega \mathrm{t}) \tag{12}$$

Equation (11) represents the DC Kerr effect and **Equation (12)** represents the electro-optic effect. The DC Kerr effect term can be related to the materials index change as it perturbs the materials polarization:

$$\mathrm{P} = \epsilon_0\left(\chi^{(1)} + 3\chi^{(3)}\mathrm{E}_{\mathrm{DC}}^2\right)\mathrm{E}_\omega \cos(\omega \mathrm{t}) \tag{13}$$

and it can be related to the materials refractive index n as:

$$n^2 = (\mathrm{n}_0 + \Delta \mathrm{n})^2 = \left(1 + \chi^{(1)} + 3\chi^{(3)}\mathrm{E}_{\mathrm{DC}}^2\right) \tag{14}$$

Therefore, the material refractive index change Δn that introduced by the DC Kerr effect can be expressed as:

$$\Delta \mathrm{n} = \frac{3}{2\mathrm{n}_0}\chi^{(3)}\mathrm{E}_{\mathrm{DC}}^2 \tag{15}$$

Similarly, the electrooptic effect term can also be related to the materials index change and can be viewed as an effective $\chi^{(1)}$change. Consequently, the polarization of the materials can be expressed as

$$\mathrm{P} = \epsilon_0\left(\chi^{(1)} + 2\chi^{(2)}\mathrm{E}_{\mathrm{DC}}\right)\mathrm{E}_\omega \cos(\omega \mathrm{t}) \tag{16}$$

and

$$\mathrm{n}^2 = (\mathrm{n}_0 + \Delta \mathrm{n})^2 = \left(1 + \chi^{(1)} + 2\chi^{(2)}\mathrm{E}_{\mathrm{DC}}\right) \tag{17}$$

Therefore, the material refractive index change Δn that introduced by the electro-optic effect can be expressed as:

$$\Delta n = \frac{1}{n_0}\chi^{(2)}E_{DC} \tag{18}$$

Comparing **Equation (15)** and **(16)**, the relationship between $\chi^{(3)}$ and the corresponding effective $\chi_{eff}^{(2)}$ can be found:

$$\chi_{eff}^{(2)} = \frac{3}{2}\chi^{(3)}E_{dc} \tag{19}$$

3.3.2 Measurement results and analysis

To characterize the DC Kerr effect, we again use the same setup as the optical loss measurement which is shown in **Figure 3.4**. An electric field is applied horizontally across the a-SiC waveguide by applying a voltage between the contact pads. We measured the resonance wavelength shift $\Delta\lambda$ at different applied voltages. The change in the effective index Δn_{eff} is related to $\Delta\lambda$ as [73]:

$$\frac{\Delta\lambda}{\lambda_{res}} = \frac{3}{4}\frac{\Delta n_{eff}}{n_g} \tag{20}$$

where λ_{res} is the resonance wavelength and n_g is the group index of the waveguide. From our design, since the electrode only covers 3/4 of the ring waveguide as shown in **Figure 3.3(c)**, the Δn_{eff} is normalized with respect to the ring perimeter. The resonance shifts for three applied voltages are shown in **Figure 3.7 (a)**. The extracted Δn_{eff} from **Equation (20)** is then correlated

with the FDE simulations to estimate the materials' index change Δn under the same applied electric field.

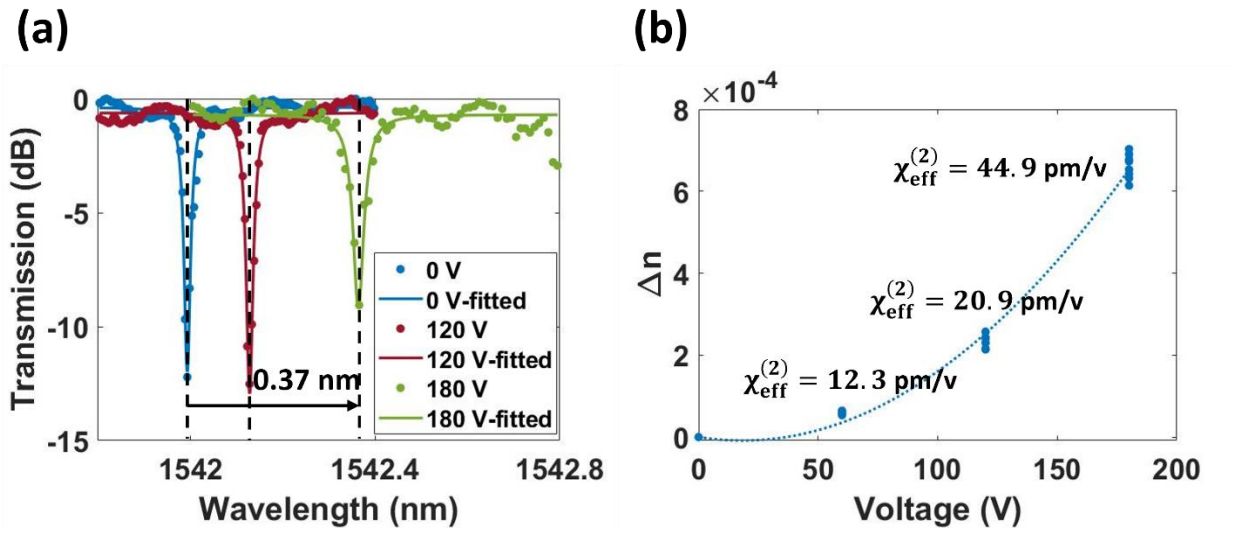

Figure 3.7 (a) Resonance shift of the ring transmission spectra at 0, 120, and 180 V and (b) calculated Δn vs applied voltage 0, 60, 120, and 180 V. The Δn is fitted with a quadratic function in the applied voltage.

An electric field distribution simulation was performed to better understand the electric field across the waveguide. **Figure 3.8** shows the simulated electric field distribution between the electrodes. The electric field is across the silicon dioxide cladding, the buried oxide, and the silicon rich a-SiC waveguide. We find that the electric field is uniform across the a-SiC waveguide under different applied voltages.

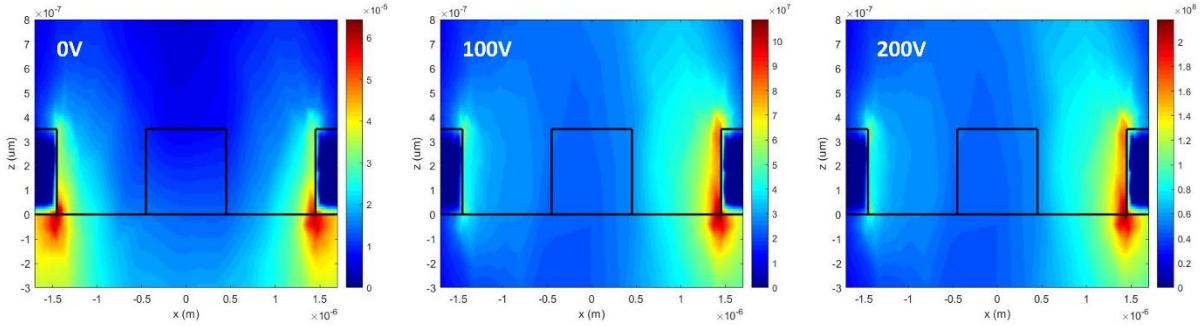

Figure 3.8 Electric field distribution simulation under 0V, 100V and 200V.

From the four-point probe measurement, the resistivity of our a-SiC film was measured to be $4.2 \times 10^8\ \Omega \cdot \text{cm}$. This indicates that our film possesses rather high resistance. Therefore, in the simulation, we set the a-SiC layer to be dielectric. The dielectric constant of the a-SiC material is set to be 8.5 from the C-V measurement which is shown in **Figure 2.9**. The bandgap of the film is 2.05 eV as we measured from the ellipsometer. The dielectric constant for SiO_2 layer is set to be 3.9.

Table 3.1 summarizes the average electric field and the standard deviation (STD) of the electric field of all the mesh grid points in the a-SiC waveguide region. The results show that around 70% of the electric field is within ±6% of the average electric field and 95% of the electric field is within ±12% of the average electric field. The relatively small STD indicates a uniform electric field distribution in the a-SiC waveguide.

Table 3.1 Average and STD of the simulated electric field under 0V, 100V and 200V

Applied voltage (V)	0V	100V	200V
Ave. E-field (V/m)	1.1E-05	2.4E+07	4.8E+07
Std. E-field (V/m)	2.0E-06	1.6E+06	3.2E+06

From here, we assume that the electric field is uniform in the a-SiC waveguide and use the simulated average electric field to extract the materials nonlinearity from DC Kerr effect measurement. $\chi^{(3)}$ and the corresponding nonlinear index n_2 are extracted from Δn and the applied electric field using **Equation (15)** and

$$n_2 = \frac{3\chi^{(3)}}{4n_0} Z \tag{21}$$

where n_0 is the real part of the materials' index and Z is the free space impedance which equals 377 Ω. A plot of the Δn vs the voltage is shown in **Figure 3.7 (b)**, which shows the quadratic dependence between Δn and the applied voltage. This confirms that the index change is mainly due to the DC Kerr effect, as indicated in **Equation (15)**. The $\chi^{(3)}$ and n_2 extracted from our silicon rich a-SiC waveguides are 6.9×10^{-19} m^2/V^2 and 2.54×10^{-17} m^2/W, which are more than six times and five times higher than the stoichiometric a-SiC [59], respectively.

The electric field induced $\chi_{eff}^{(2)}$ is calculated using **Equation (19)**. The $\chi_{eff}^{(2)}$ calculated from the measurement data are 44.9 pm/V under 180 V, which is more than two times higher than the reported value from crystalline silicon [68] and silicon rich nitride [74] utilizing the DC Kerr effect. Due to the limitation of the experimental setup, we could not apply voltages up near the breakdown

field. Theoretically, if the waveguide is poled under near breakdown field of 2.2×10^6 V/cm, the induced $\chi_{\text{eff}}^{(2)}$ could be even higher.

3.3.3 Nonlinear materials Comparison

We now look at comparing the important material properties of the competing materials. **Table 3.2** is the comparison of the materials that use the ring waveguide to demonstrate the DC Kerr effect. It can be seen that our silicon rich carbide has the highest $\chi^{(3)}$ as well as the highest breakdown electric field. These are the two important factors for the electric field induced $\chi^{(2)}$ process. Although the in-waveguide propagation loss α is higher than the other reported values. We believe that it could be reduced by further optimizing the fabrication process to preclude the fabrication imperfection.

Table 3.2 Silicon photonic materials that demonstrate the DC Kerr effect.

	Silicon rich SiC	Silicon [68]	Silicon rich nitride [74]
n_0	2.77	3.48	3.02
$\chi^{(3)}\ \left(\frac{\text{m}^2}{\text{V}^2}\right)$	6.9×10^{-19}	2.45×10^{-19}	6×10^{-19}
$\chi_{\text{eff}}^{(2)}\ \left(\frac{\text{pm}}{\text{V}}\right)^*$	44.9	16.0	14.5
$\text{E}_{\text{bd}}\ \left(\frac{\text{V}}{\text{cm}}\right)$	2.2×10^6	2.5×10^5	1.2×10^6
$\alpha\ \left(\frac{\text{dB}}{\text{cm}}\right)$	6.2	< 1	3.4

* The $\chi_{\text{eff}}^{(2)}$ shown here are poled under different electric fields.

Table 3.3 Nonlinear index of high bandgap materials

Material	n_2 (m^2/W)
Si_3N_4 [75]	2.4×10^{-19}
Silicon rich nitride [76]	2.8×10^{-17}
Hydex [77]	1.1×10^{-19}
AlN [78]	2.3×10^{-19}
Diamond [79]	8.2×10^{-20}
Ta_2O_5 [80]	3.4×10^{-18}
a-SiC [59]	4.8×10^{-18}
Silicon rich a-SiC	2.54×10^{-17}

Table 3.3 shows a comparison of several high band gap materials that are used for nonlinear applications. In Chapter 1, we showed that the figure of merit for nonlinear optical process is the nonlinear index divided by the two-photon absorption coefficient. Among these materials, the band gap is high enough to eliminate the two-photon absorption. So, the higher the nonlinear index the more efficient nonlinear material it is. As we can see from the table, Silicon rich carbide has an outstanding n_2. We believe that silicon rich carbide could be a very good candidate as a new material for optical nonlinear processes. Very efficient devices could be realized based on the material.

3.4 Conclusion

In conclusion, we demonstrate the design of the silicon rich carbide waveguide to achieve both single mode operation and the fabrication tolerance. The waveguide fabrication process is proposed and demonstrated by utilizing UCSD nano3 cleanroom facilities. An optical ring resonator is used to estimate the propagation loss of the waveguide. The Q_L and Q_i for our ring resonators are extracted to be ~68 000 and 96 000, respectively, and the corresponding propagation loss is 6.2 dB/cm. By using the cutback method to a wider waveguide, we conclude that the higher loss was mainly the scattering loss from the side wall of the waveguide. It can be improved by optimizing the fabrication process. An edge coupler is also designed to achieve better coupling efficiency from the fiber mode to waveguide mode. From the FDTD simulation, 84% of coupling efficiency can be achieved.

In the second part of the chapter, we experimentally demonstrate the DC Kerr effect in silicon rich carbide film and extract the third order nonlinearities (6.9×10^{-19} m^2/V^2) and the nonlinear index (2.54×10^{-17} m^2/W). The extracted induced second order nonlinearity is as high as 44.9 pm/V. With the high nonlinearity, the wide bandgap, the potential for low loss, and the easy control of the materials' properties by the PECVD process, we believe that silicon rich carbide provides a promising material for nonlinear optical applications.

Chapter 3, in part, is a reprint of the materials as it appears in Applied Physics Letters 2022. Li-Yang Sunny Chang, Hani Nejadriahi, Steve Pappert, and Paul K. L. Yu. The dissertation author is the primary investigator and author of this paper.

CHAPTER 4: EFFICIENT SILICON RICH SILICON CARBIDE THERMO-OPTIC PHASE SHIFTER

4.1 Introduction

Silicon carbide emerges as a potential material for advancing photonic integrated circuit (PIC) applications, offering a diverse array of functionalities. With its large transparency window [81], minimal waveguide propagation loss [52], and notable second order [42] and third order nonlinearities [43], silicon carbide becomes an appealing material for PIC development across various applications. Its advantage over silicon devices becomes evident in its absence of two-photon absorption at near-infrared (NIR) wavelengths, making it an attractive choice for high-intensity nonlinear optical PICs. Already, several nonlinear optical devices based on silicon carbide have been successfully demonstrated [51, 53, 55], highlighting its potential. The unique vacancy states within silicon carbide contribute to its standing as a distinctive material for quantum photonic applications [50].

In addition to these attributes, the sought-after qualities for integrated photonic applications encompass tunability and reconfigurability of photonic circuits. These capabilities enable the creation of reconfigurable photonic devices, crucial for numerous applications such as optical modulators and all-optical switches. A widely employed mechanism for circuit tuning is the thermo-optic effect, which hinges on the material's thermo-optic coefficient (TOC) – a metric measuring the refractive index's response to temperature changes.

For stoichiometric silicon carbide, the TOC stands at $2.67 \times 10^{-5}\,℃^{-1}$, significantly lower than that of silicon ($1.8 \times 10^{-4}\,℃^{-1}$), ultimately leading to less competitive thermal tuning

capabilities. The combination of a lower TOC and refractive index results in higher power consumption and larger device footprints for stoichiometric SiC-based devices. A viable remedy involves leveraging silicon-rich a-SiC instead of stoichiometric SiC. By manipulating deposition conditions, the silicon content can be tailored to improve optical properties. Recent findings indicate the potential for achieving remarkable third-order nonlinearity in silicon-rich a-SiC through the DC Kerr effect [82]. A higher refractive index leads to a more confined mode within the waveguide, enabling a smaller device footprint.

In the first part of the chapter, I will discuss our work in characterizing the TOC of the a-SiC with different stoichiometry. It is done by measuring the change of the transmission spectrum of the ring resonators under different temperatures. We have observed an enhancement in the TOC. In the second part of the chapter, I will discuss our effort in designing and demonstrating an efficient thermo-optic phase shifter based on silicon rich carbide waveguide integrated with NiCr heaters. A high thermo-optic tunability and a low P_π is achieved.

4.2 Study of thermo-optic coefficient in silicon carbide

To investigate the thermo-optic properties of a-SiC with different stoichiometry, the a-SiC films are prepared by PECVD onto a thermally oxidized silicon substrate. As discussed in Chapter 2, by varying the flow ratio of the precursors, SiH_4 and CH_4, a-SiC films with different stoichiometry can be realized. The refractive index of the films ranges from 2.48 to 2.8 at 1550 nm as measured by the ellipsometer. **Table 4.1** summarizes the materials index and the flow rate of precursor gases for samples SRC1, SRC2, and SRC3 investigated in this work. Energy-Dispersive X-ray spectroscopy (EDX) measurement in our previous work indicates that the silicon

content increases as the SiH_4/CH_4 gas flow ratio increases [82]. The EDX estimated silicon content of these samples is shown in **Table 4.1**.

Table 4.1 Refractive index n at λ=1550 nm and the precursor gasses flow rate of the three a-SiC films SRC1, SRC2, and SRC3 in this study.

Materials	n	SiH_4 flow rate (sccm)	CH_4 flow rate (sccm)	Si content (%)
SRC1	2.48	200	100	61
SRC2	2.61	200	50	70
SRC3	2.80	300	50	80

To determine the materials' TOC, we fabricated three different sets of micro-ring resonators using the three different films (SRC1, SRC2, and SRC3) we prepared earlier. The a-SiC thin film is patterned by electron beam lithography (EBL) and the patterns are transferred by reactive ion etching (RIE) with CHF_3 and O_2 etching chemistry. The samples are then encapsulated by a silicon dioxide cladding layer using PECVD. Finally, the input and the output of the waveguides are polished by focused ion beam (FIB) milling to ensure better edge coupling efficiency. **Figure 4.1(a)** illustrates the fabrication process for the waveguides. **Figure 4.1(b)** shows the Scanning Electron Microscopic (SEM) cross-section image of the waveguides. The waveguide width and height are 875 nm and 320 nm respectively, which are designed to ensure single-mode propagation in the waveguide as simulated by a Finite Difference Eigenmode (FDE) solver built in Lumerical MODE. **Figure 4.1(c)** shows the FDE simulated mode profile of the waveguide made on SRC3. The bending radius for the ring waveguide is 50 μm. The coupling gap between the bus and the ring waveguides are designed to range from 100 to 400 nm to find the critical coupling.

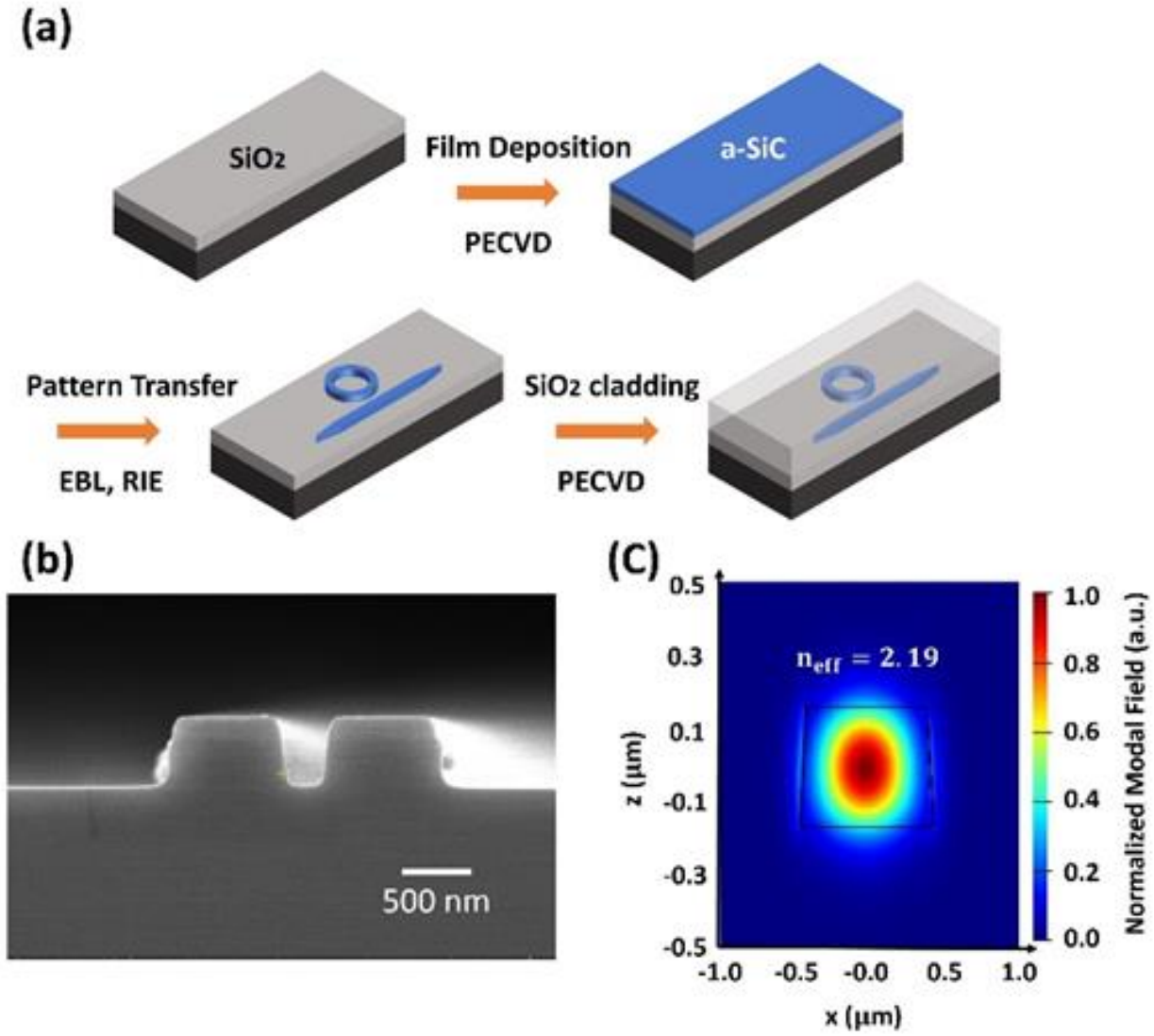

Figure 4.1 (a) Schematic of the fabrication process of the silicon-rich a-SiC micro-ring resonators. (b) The SEM cross-section image of the waveguide (hydrogen silsesquioxane (HSQ) is not removed). (c) The simulated mode profile for the waveguide made on SRC3. The simulated effective index is 2.19.

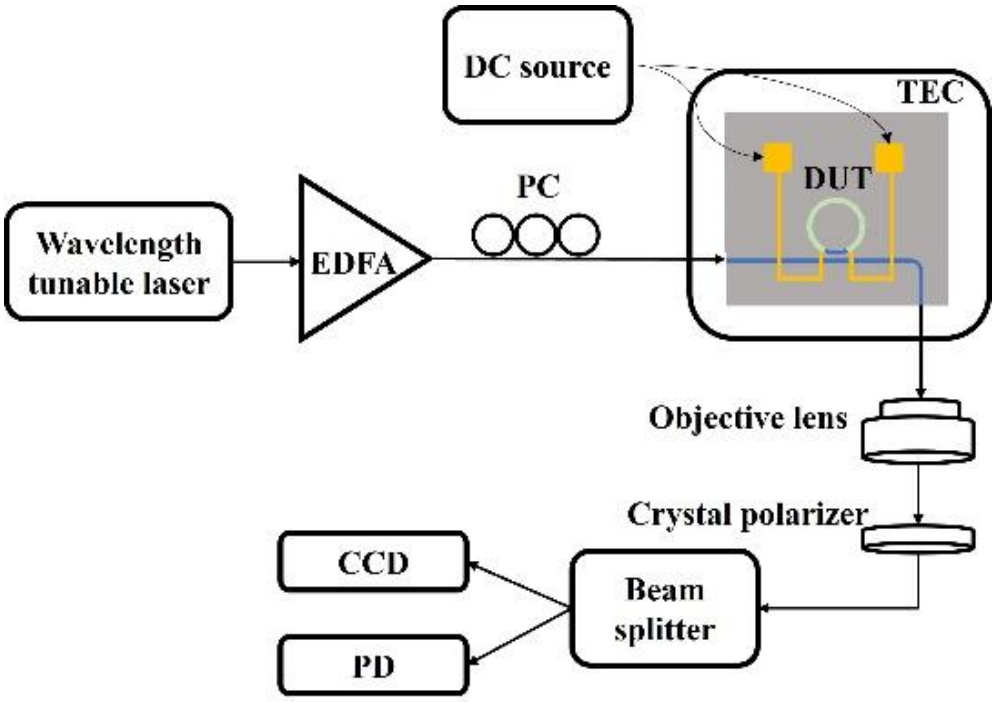

Figure 4.2 Schematic of measurement setup for thermal-optic characterization.

The transmission spectra of the ring resonators are obtained using a fiber-in-free-space-out setup shown in **Figure 4.2**. The output from a wavelength-tunable CW laser ranging from 1465 to 1575 nm is applied through a single-mode fiber, an Erbium-Doped Fiber Amplifier (EDFA), and a polarization controller to make sure that only the TE-polarized mode is excited in the waveguide. A lensed fiber is used to edge couple the laser light to the device under test (DUT). The output spectrum is filtered by a TE-mode crystal polarizer and then collected using a large-area InGaAs/InP photodetector which detect this wavelength range. The DUT is mounted onto a stage that is temperature controlled by a thermo-electric cooler (TEC) module with an accuracy of ± 0.1 ℃.

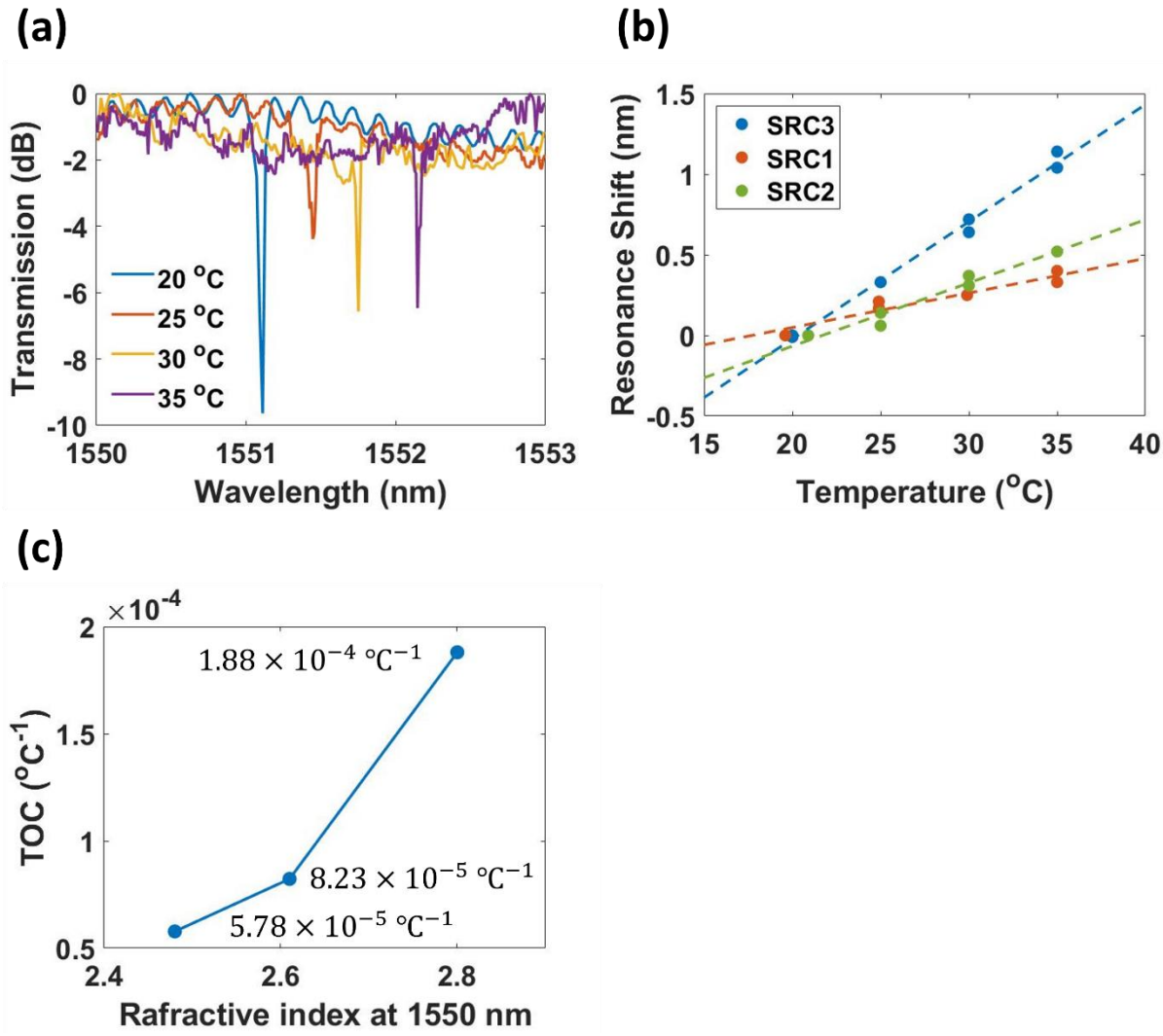

Figure 4.3 (a) Transmission spectra of the micro-ring resonator made by SRC3 under 20 ℃, 25 ℃, 30 ℃, and 35 ℃ at a wavelength around 1550 nm. The variation of the extinction ratio is due to the resolution limit of the wavelength sweep in the system. (b) Extracted resonance wavelength shift for the micro-ring resonators with three different stoichiometry SRC1, SRC2, and SRC3. (c) Extracted thermo-optic coefficient for the three films.

We measure the transmission resonance wavelength shift by changing the TEC temperature. **Figure 4.3(a)** shows the transmission spectra near the 1550 nm wavelength measured from the SRC3 ring resonators at temperatures ranging from 20 ℃ to 35 ℃. The red shift of the resonance wavelength with temperature indicates a positive TOC in a-SiC. We apply the Lorentzian fit function to the resonance response and then calculate the resonance wavelength. The resonance wavelength shifts versus temperature are plotted in **Figure 4.3(b)**. We can see that SRC3 has the largest resonance shift in response to the temperature change. Hence, we demonstrated that larger silicon content leads to a larger temperature response.

The TOC of the materials can be extracted from the resonance shift. Temperature dependence of the resonance wavelength can be related to the effective index n_{eff} as [83]:

$$\frac{d\lambda}{dT} = \left(n_{eff} \cdot \alpha_{sub} + \frac{dn_{eff}}{dT}\right)\frac{\lambda}{n_g} \tag{22}$$

where αsub is the thermal expansion coefficient of the silicon dioxide, λ is the resonance wavelength, and n_g is the group index of the waveguide. The change of the effective index is due to the interaction of the mode with the waveguide core and cladding and can be related to the change of the materials' index as [84]:

$$\frac{dn_{eff}}{dT} = \Gamma_{SiO2}\left(\frac{dn}{dT}\right)_{SiO2} + \Gamma_{a-SiC}\left(\frac{dn}{dT}\right)_{a-SiC} \tag{23}$$

where Γ is the overlap integral of the SiC waveguide core and the silicon dioxide cladding and dn/dT is the TOC of the materials. **Figure 4.3(c)** shows the extracted TOC of the three films investigated. A clear trend of increasing the materials' refractive index leading to an increase in the TOC is observed. The result shows a more than three-fold improvement in the TOC from SRC1

(5.78×10^{-5} ℃$^{-1}$) to SRC3 (1.88×10^{-4} ℃$^{-1}$). The highest TOC achieved in SRC3 is comparable to that of crystalline Si (1.8 × 10−4 ℃$^{-1}$ [32]).

Table 4.2 provides a comparison of different types of SiC, including the SiC on insulator wafer formation techniques, refractive index and the extracted TOC. We can see that a-SiC has the advantage of easier fabrication and tunability of materials properties. By enriching the silicon content, we are gaining thermal optic tunability due to higher index and higher TOC.

Table 4.2 Comparison of different types of silicon carbide.

Material	Technique	Index	TOC (1/℃)	Reference
3C-SiC	Wafer Bonding	2.6	2.67×10^{-5}	[57]
4H-SiC	Smartcut	2.6	4.21×10^{-5}	[85]
6H-SiC	Smartcut	2.5	3.87×10^{-5}	[86]
a-SiC	PECVD	2.32	4.65×10^{-5}	[87]
a-SiC	PECVD	N/A	9.20×10^{-5}	[61]
SRC	PECVD	2.8	1.88×10^{-4}	

4.3 Silicon rich carbide thermo-optic phase shifter

The SRC3 micro-ring is further investigated by integrating it with a NiCr heater to form a thermo-optic phase shifter. The NiCr heater film is positioned on top of the a-SiC waveguide. By applying current through the heater, it can effectively heat up the waveguide underneath. The simulation of the temperature distributions in the devices is done by the Lumerical heat solver.

Detailed materials parameters used in the simulation are shown in **Table 4.3**, where ρ, C, k are the density, specific heat, and the thermal conductivity, respectively.

Table 4.3 Material parameters used in the temperature distribution simulation.

Material	ρ (kg/m^3)	C (J/ (kg· K))	k (W/ (m·K))
Si	2330	711	148
SiO_2	2203	709	1.38
a-SiC	2480	750	120
NiCr	8400	450	11.3

Firstly, we have investigated three types of waveguides: a-SiC, c-SiC and c-Si to explore the impact of thermal conductivity on the device's temperature distribution. The waveguide and the heater geometries are the same in each simulation. The thermal conductivity for the three materials is set to be 120 W/mK, 490 W/mK and 148 W/mK, respectively. With 20 mW of power applied to the heater, the temperature of the waveguides is close to 326 K for the three films. From the simulation, we do not observe any significant advantage with lower thermal conductivity. Intuitively, we believe this is due to the fact that the waveguide geometry is rather small compared to the whole heating area (2 μm heater and waveguide separation). We found the temperature distribution profiles for a-SiC waveguide and c-SiC waveguide are very similar as shown in **Figure 4.4**.

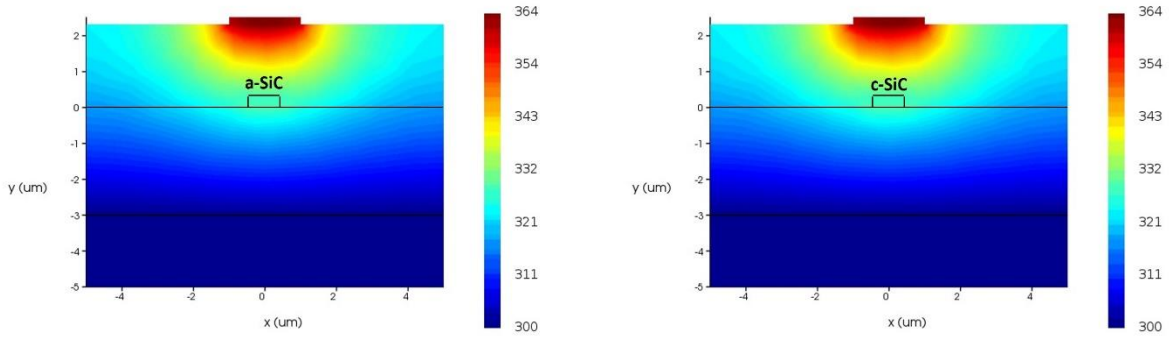

Figure 4.4 Temperature distribution profiles for a-SiC waveguide and c-SiC waveguide.

Next, we study the separation between the NiCr heater and the a-SiC waveguide. We fixed the heater geometry to 200 nm × 1.5 μm and varies the separation from 1 μm to 2 μm. **Figure 4.5(a)** shows the device configuration in the simulation and **Figure 4.5(b)** shows the temperature of the a-SiC waveguide under different heater and waveguide separation setting. It is obvious that as the heater gets closer to the waveguide, it can heat up the waveguide more effectively. However, the loss could also be higher as the metal gets closer to the waveguide. A Lumerical MODE simulation is done to estimate the propagation loss of the waveguide with different metal waveguide separation which is shown in **Figure 4.5(c)**. As we can see from the figure, there is almost no loss when the separation is larger than 1.5 μm. To be extra safe, we design our heater to be placed at 2 μm separation.

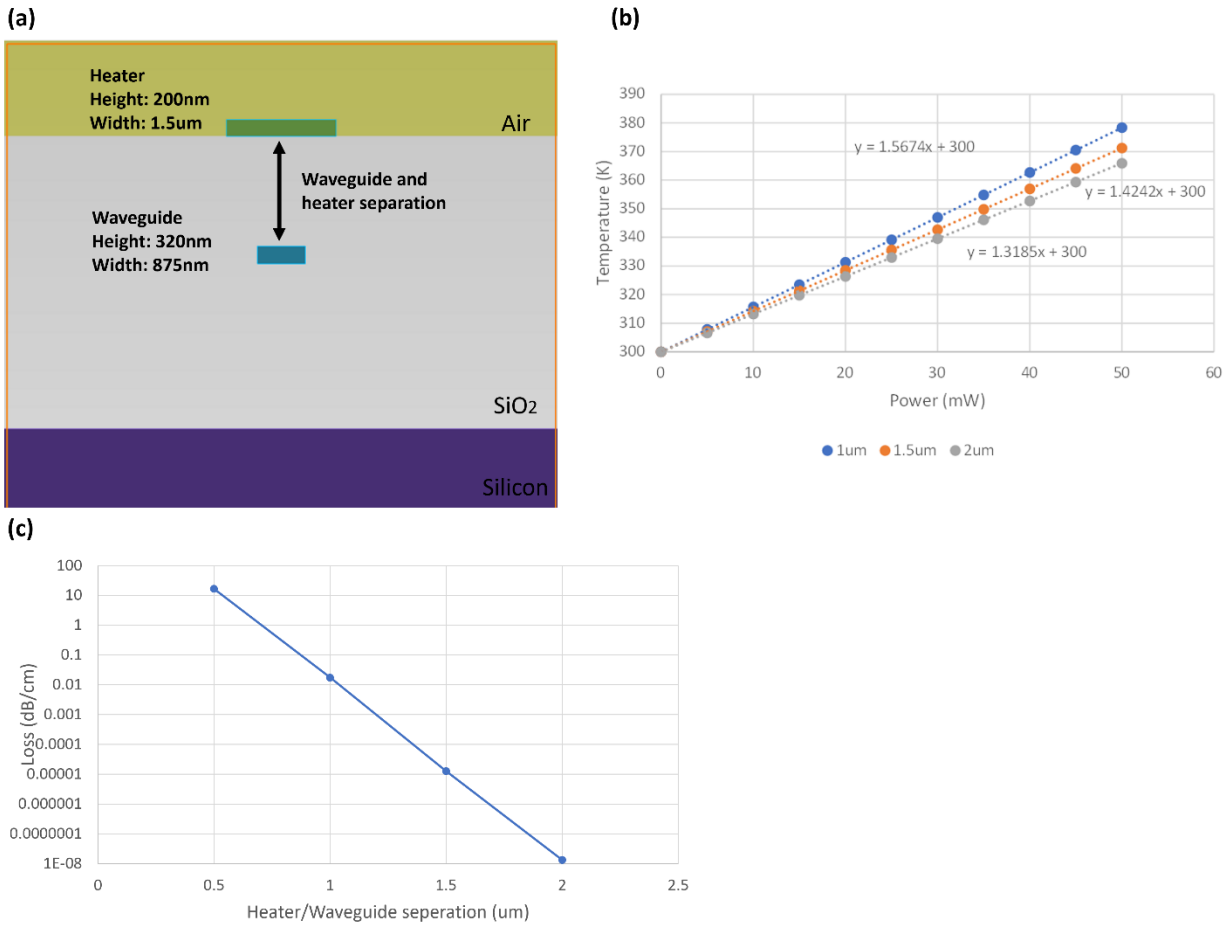

Figure 4.5 (a) Temperature distribution simulation configurations. (b) The temperature of the waveguide core for 1μm, 1.5 μm and 2 μm separations under the applied power from 0 mW to 50 mW. (c) Propagation loss of the optical mode with the separation of 0.5 um, 1μm, 1.5 μm and 2 μm.

The width of the heater is also simulated in the thermal simulation. **Figure 4.6** shows the results. The simulation indicates that the narrower the heater the more effective the heater can be. But the improvement is insignificant. The increase of waveguide temperature per mW change from 0.12974 K/mW (3µm) to 0.13712 K/mW (0.5 µm). In consideration of the alignment limitation of our photolithography mask aligner, we decide to set out heater width to be 2 µm to have a good balance in efficiency and the easiness of fabrication.

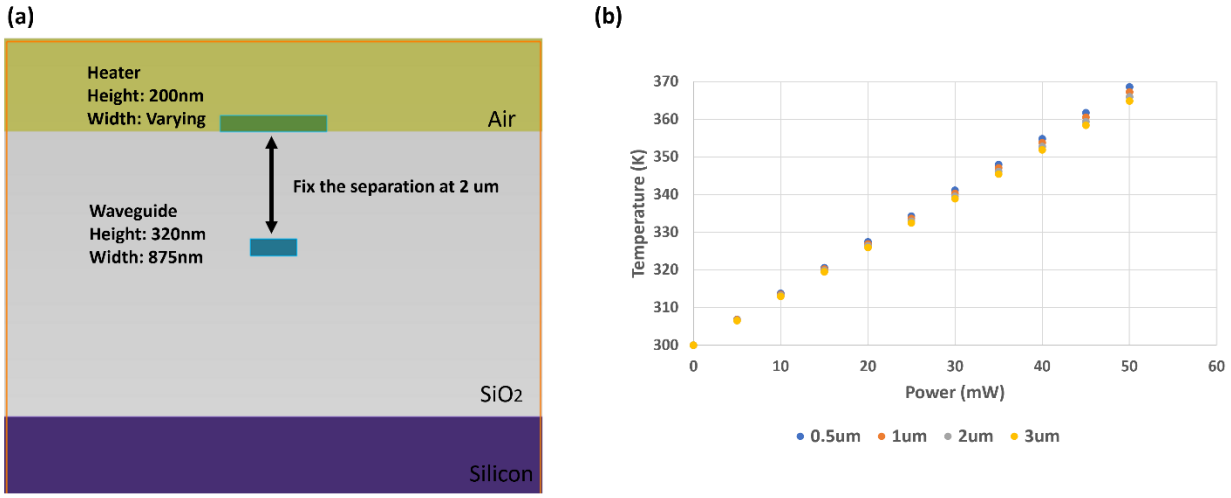

Figure 4.6 (a) Temperature distribution simulation configurations. (b) The temperature of the waveguide core for 0.5μm, 1 μm, 2 μm and 3 μm heater width under the applied power from 0 mW to 50 mW.

The following shows the simulation procedures of the device's thermal optic tunability. After the temperature distribution simulation is performed using Lumerical Heat solver, we extract the temperature of the waveguide under different applied powers. Next, we calculate the material index change by multiplying the extracted TOC and the temperature change. The Lumerical FDE solver is then applied to simulate the effective index of the mode under different applied powers. The calculated effective index from the FDE solver for the three films are used to simulate the transmission spectrum using MATLAB; and the resonance peak shift is extracted. **Figure 4.7(a)(b)(c)** shows the simulated transmission spectrum for SRC1, SRC2 and SRC3 samples. **Figure 4.7(d)** is a comparison of the simulated tunability of micro-ring phase shifter made of the three films SRC1, SRC2 and SRC3. We observed that the tunability for SRC3 device is much higher when compared with the other two. The reason is that the SRC3 device is not only gaining from a lot higher TOC but also has higher mode confinement for the same waveguide geometry.

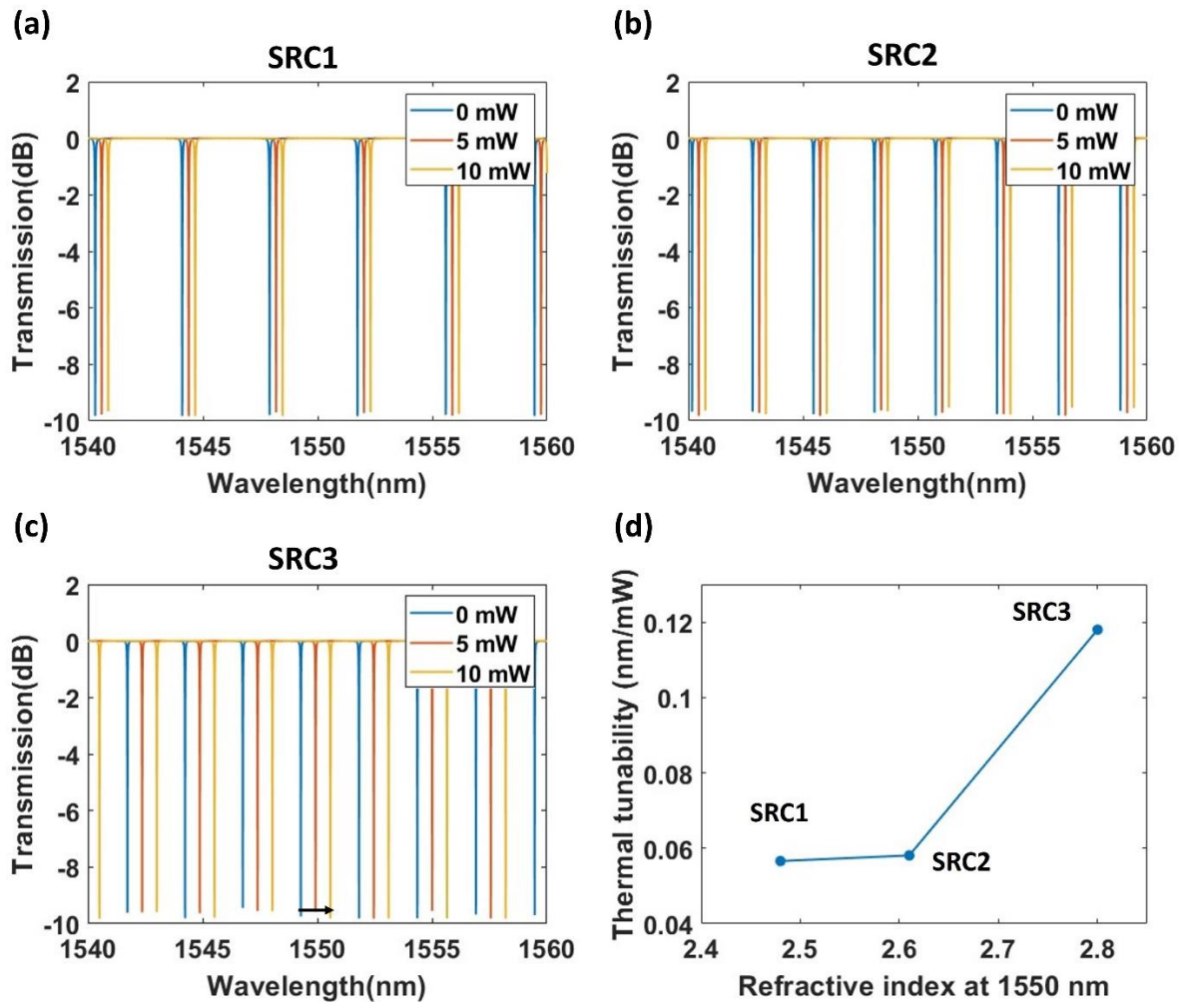

Figure 4.7 (a)(b)(c) Simulated transmission spectrum of the micro-ring phase shifter made of SRC1, SRC2, SRC3, respectively. (d) Simulated thermal optic tunability of the three devices

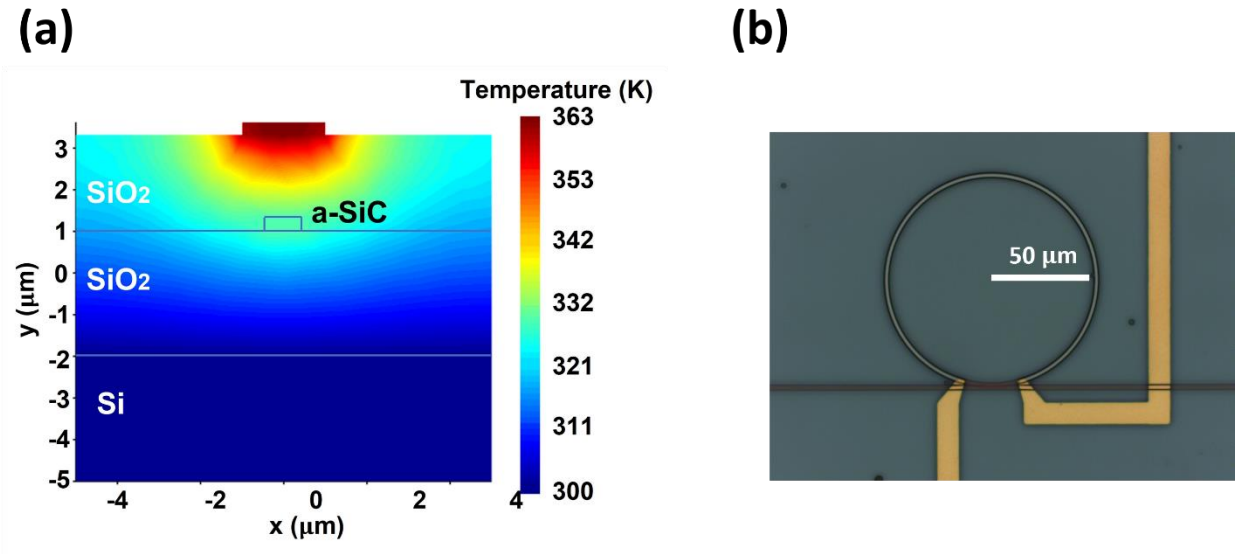

Figure 4.8 (a) Temperature distribution simulation for the a-SiC micro-ring resonator heated by a NiCr heater under 20 mW of applied power. (b) Top view of the fabricated micro-ring phase shifters obtained using an OM.

Figure 4.8(a) shows the simulated temperature distributions with 20 mW of applied power. The NiCr heater is designed to be 2 µm wide, 200 nm thick, and has a separation of 2 µm from the silicon-rich a-SiC waveguide as discussed in previous paragraphs. From the simulation, the temperature in the waveguide is increased by 1.319°C per 1 mW of applied power, which is used in **Figure 4.7(c)** in simulating the wavelength shift with respect to the applied power. The NiCr heater is formed using the lift-off process after the fabrication steps shown in **Figure 4.1(a)**. It is patterned using NR9–3000 negative resist and a Heidelberg MLA150 maskless aligner. A 200 nm layer of NiCr is then deposited by a Denton 18 sputter system. Finally, a 300 nm gold contact pad is formed by the same lift-off process. The resistance of the NiCr heater is measured to be 3600 Ω using an Agilent semiconductor analyzer. Figure 4(b) shows an optical microscope (OM) image of the top view of the micro-ring heater and the gold contact pad, which illustrates the heating area.

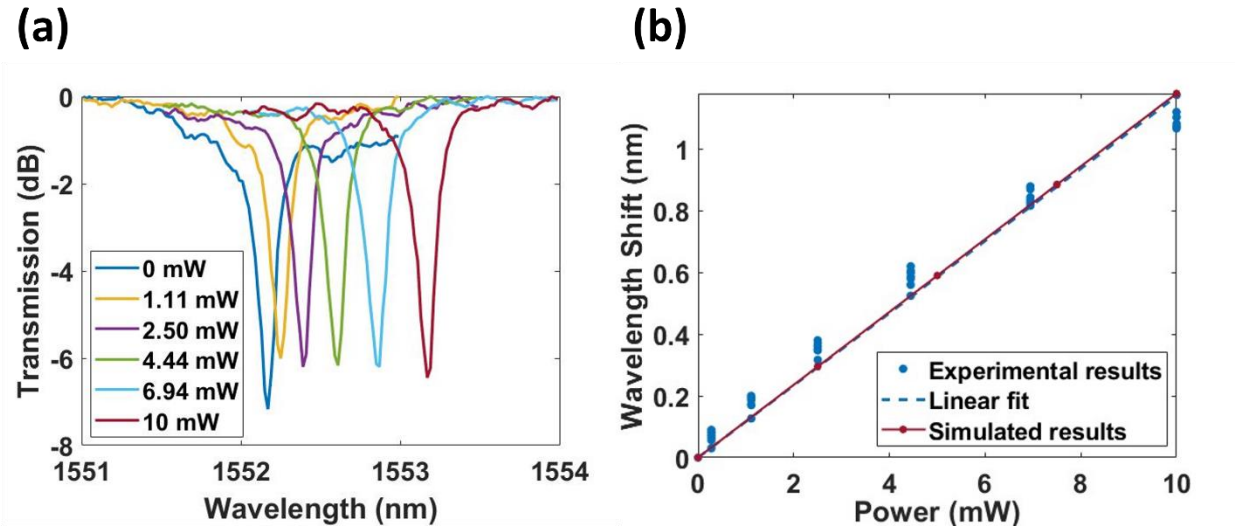

Figure 4.9 (a) The transmission spectra of the micro-ring phase shifter made from SRC3 obtained under different applied voltages at a wavelength of around 1552 nm. (b) The simulated and the experimental results for the thermal tunability of the phase shifter. The extracted thermal tunability is 0.117 nm/mW.

The thermo-optic phase shifter is then measured by applying different powers and collecting the transmission spectra using the same setup depicted in **Figure 4.2**. The optical insertion loss is approximately 13 dB which includes a 1.86 dB propagation loss for the 3 mm long device and 11.1 dB fiber to chip coupling loss. Note that the fiber to chip coupling largely depends on how good we can align the lensed fiber to waveguide manually. So, it may vary a lot from measurement to measurement. **Figure 4.9(a)** shows the measured resonance wavelength at around 1552 nm with different applied powers. We observed around 6 dB extinction ratio for switching on and off. The extinction ratio could be improved by better addressing the coupling gap to achieve critical coupling. We extract the resonance wavelength shift and plot it versus applied power in Fig. 5(b). The simulated results which are shown in **Figure 4.7(c)** are also plotted together for comparison. From **Figure 4.9(b),** one can see good agreement between the experimental and the

calculated results. A linear trend is observed, an 0.117 nm/mW of thermal tunability is estimated from the slope of the linear fit to the data. The power requirement for a π phase shift, Pπ, for resonator based thermo-optic switches can be defined as the power consumption needed to tune the resonator by a phase shift of the product of π and the full width at half maximum (FWHM) of the resonance peak, and it can be calculated as [88]:

$$P\pi = FWHM \times \pi \, \eta \tag{24}$$

where η is the thermal tunability. The FWHM for our device is 0.155 nm and the Pπ is calculated to be 4.2 mW. The P_π could be further reduced by reducing the distance between the heater and the waveguide as discussed in previous paragraphs, with the drawback of higher waveguide propagation loss. The small Pπ indicates the potential for the realization of many efficient thermo-optic integrated circuit applications.

4.4 Comparison of thermo-optic switch based on silicon photonics

Table 4.4 presents a comprehensive overview of thermo-optic switches based on common silicon photonic materials, outlining essential performance parameters for evaluation. Our own results for SRC are included in the table for comparative analysis. Notably, the SRC device exhibits a tuning efficiency that is on par with other counterparts. It's worth mentioning that our device design isn't solely optimized for compact configurations, leaving room for potential smaller footprints and less insertion loss through more intricate design considerations. Furthermore, the SRC phase shifter offers distinct advantages over silicon, particularly for applications necessitating robust optical power handling capabilities. As a result, SRC emerges as a compelling option for realizing efficient, small footprint, and high optical power handling devices.

Table 4.4 Performance matrix for the thermo-topic switch base on silicon photonic materials

Material	Tunning efficiency (mW/π)	Extinction ratio (dB)	Loss (dB)	Footprint (μm^2)	Power handling
Si [33]	2.56	23	1.23	109× 21	Low
Si [89]	3	20	0.9	67× 28	Low
SRN [90]	8	9	1.2	65× 65	High
SiN [91]	64.4	25	0.48	700000	High
SiC [57]	50	14	N/A	80× 80	High
SRC	4.2	6	1.86	100× 100	High

4.5 Conclusion

In summary, we have measured the TOC in a-SiC thin films as the silicon content increases. By heating up a-SiC micro-ring resonator, we capture the resonance shift of the transmission spectrum to estimate the TOC of the materials. We find that by increasing the silicon content, we can effectively increase the TOC of the material. A more than threefold improvement is achieved in our silicon-rich a-SiC thin films compared with stoichiometric a-SiC thin film. The highest TOC we get is 1.88×10^{-4} ℃, which is comparable to that of crystalline silicon.

In the second part of the chapter, we discuss the design and demonstration of a highly efficient thermo-optic phase shifter by integrating a NiCr heater with a silicon-rich a-SiC micro-ring resonator. A thermal tunability of 0.117 nm/mW is achieved in the micro-ring resonator, which translates to a Pπ of 4.2 mW. With the high TOC and easy tuning of the material properties, we believe that silicon-rich a-SiC can be a promising material for reconfigurable PIC applications.

Chapter 4, in part, is a reprint of the materials as it appears in Optics Letters 2023. Li-Yang Sunny Chang, Steve Pappert, and Paul K. L. Yu. The dissertation author is the primary investigator and author of this paper.

CHAPTER 5: DEVELOPMENT OF SIC/SI HYBRID WAVEGUIDE DC KERR EFFECT OPTICAL MODULATOR

5.1 Introduction

Electro-optic modulators are essential components in modern optical communication systems, enabling the manipulation of light signals using electrical signals. These devices play a critical role in various applications, including data transmission, signal processing, and optical sensing. Electro-optic modulators typically exploit the electro-optic effect, where the refractive index of a material is modified by an applied electric field, allowing for precise control of light propagation and modulation.

Electro-optic modulators can be classified into different types based on their operating principles and materials used. One prominent category is silicon-based modulators, which rely primarily on the plasma dispersion effect [92] and often suffer from limited bandwidth due to carrier mobility constraints [93], limiting their applications in high-speed communication systems. Moreover, plasma dispersion type modulator relies on the change of the carrier concentration will always be accociated with amplitute modulation, which which could generate amplitude chirp to the phase shift [92]. Si modulators reliant on the Pockels effect can transcend these limitations, yielding fast and almost pure phase modulation. However, silicon's inherent centrosymmetric structure prevents the natural presence of $\chi^{(2)}$. Consequently, integration of materials with sizable $\chi^{(2)}$ onto the silicon platform has garnered attention. Noteworthy candidates encompass EO polymers [6], Lithium Niobate ($LiNbO_3$) [94], Barium Titanate (BTO) [9], Piezoelectric Lead Zirconate Titanate (PZT) [95], etc. Among these types of material integration, thin film lithium niobate on insulators (LNOI) is note-worthy as the availability of the commercial LNOI has made

it a very hot topic recently. It has shown a good combination of modulation efficiency (~2Vcm), optical loss (1dB/cm), and operating speed (100GHz bandwidth). However, these avenues entail hybrid or heterogeneous integration processes, significantly increasing technological complexities.

Another category of electro-optic modulators includes lithium niobate ($LiNbO_3$) modulators. These modulators are based on the electro-optic properties of $LiNbO_3$ crystals. $LiNbO_3$ modulators exhibit high electro-optic coefficients, allowing for efficient phase modulation with shorter device lengths and lower power consumption compared to silicon modulators. They can operate at higher speeds, making them suitable for high-frequency applications. However, $LiNbO_3$ modulators typically require external poling and temperature stabilization, which adds complexity to their integration and operation.

In this chapter, we propose a modulator that integrates silicon-rich carbide (SRC) onto silicon slot waveguides. Electro-optic modulation in silicon can be attained via the DC Kerr effect, inducing an effective $\chi^{(2)}$ through a DC bias. Owing to its higher 3rd order nonlinearity and the higher breakdwon electric field, SRC became a good candidate for the electric field induced $\chi^{(2)}$ process. This potential is underscored by the capacity to achieve higher induced $\chi^{(2)}$, subsequently enabling efficient electro-optic modulation. In addition, the presence of lower permittivity plays a role in reducing the RC time constant, thereby paving the way for the realization of high-speed operations. In contrast to the plasma dispersion effect, the DC Kerr effect realizes high-speed, phase modulation with reduced residual amplitude modulation accociated. Unlike the integration of ferroelectric materials or EO polymers, SRC processes offer ease, while remaining fully CMOS compatible. In this chapter, I will focus on detailing our endeavors in designing the SRC/Si hybrid

waveguide modulator, accompanied by preliminary experimental analysis of main components for the SRC/Si hybrid mach-zehnder modulator.

5.2 Device simulation and modulator performance analysis

Our initial investigation focuses on evaluating the influence of distinct SRC cladding coverage configurations in a SRC slot waveguide on the distribution of the electric field. Employing the Lumerical DEVICE solver, we seek to optimize the electric field concentration within the SRC for effective utilization of the DC Kerr effect in modulator applications**. Figure 5.1(a)** illustrates the device configuration parameters within Lumerical DEVICE. Specifically, the silicon waveguide dimensions are set at 250 nm × 200 nm, while the slot width spans 300 nm, and the slab height reaches 50 nm. The SRC layer thickness is set to be 150 nm to filled up the slot area. The doping level is maintained at 1×10^{18} cm^{-3} for both the silicon slabs and silicon waveguides, with a small portion of the slab further doped to $1 \times 10^{20}\mathrm{cm}^{-3}$ to facilitate an ohmic contact with the metal. As exemplified in **Figure 5.1(b)**, a simulation of the electric field distribution illustrates that the arrangement of the two silicon waveguides effectively creates a parallel plate, predominantly confining the electric field within the slot region. This configuration is designed to maximize the electric field contribution to induce $\chi^{(2)}$ nonlinearity of SRC.

Figure 5.1(c) presents the average electric field distribution across the waveguide for various configuration. The 2D schematic illustrates various SRC cladding coverage configurations, encompassing both ideal scenarios where only the slot region is filled with SRC, and more practical arrangements featuring larger coverage areas. Intriguingly, our simulations indicate that irrespective of the specific SRC cladding coverage employed, the variation in electric field remains within a modest 4% range in the slot region. This finding underscores the robustness

of the electric field distribution across different SRC cladding arrangements. In the folloowing, we continue our investigation on the optical mode profile under the same structures.

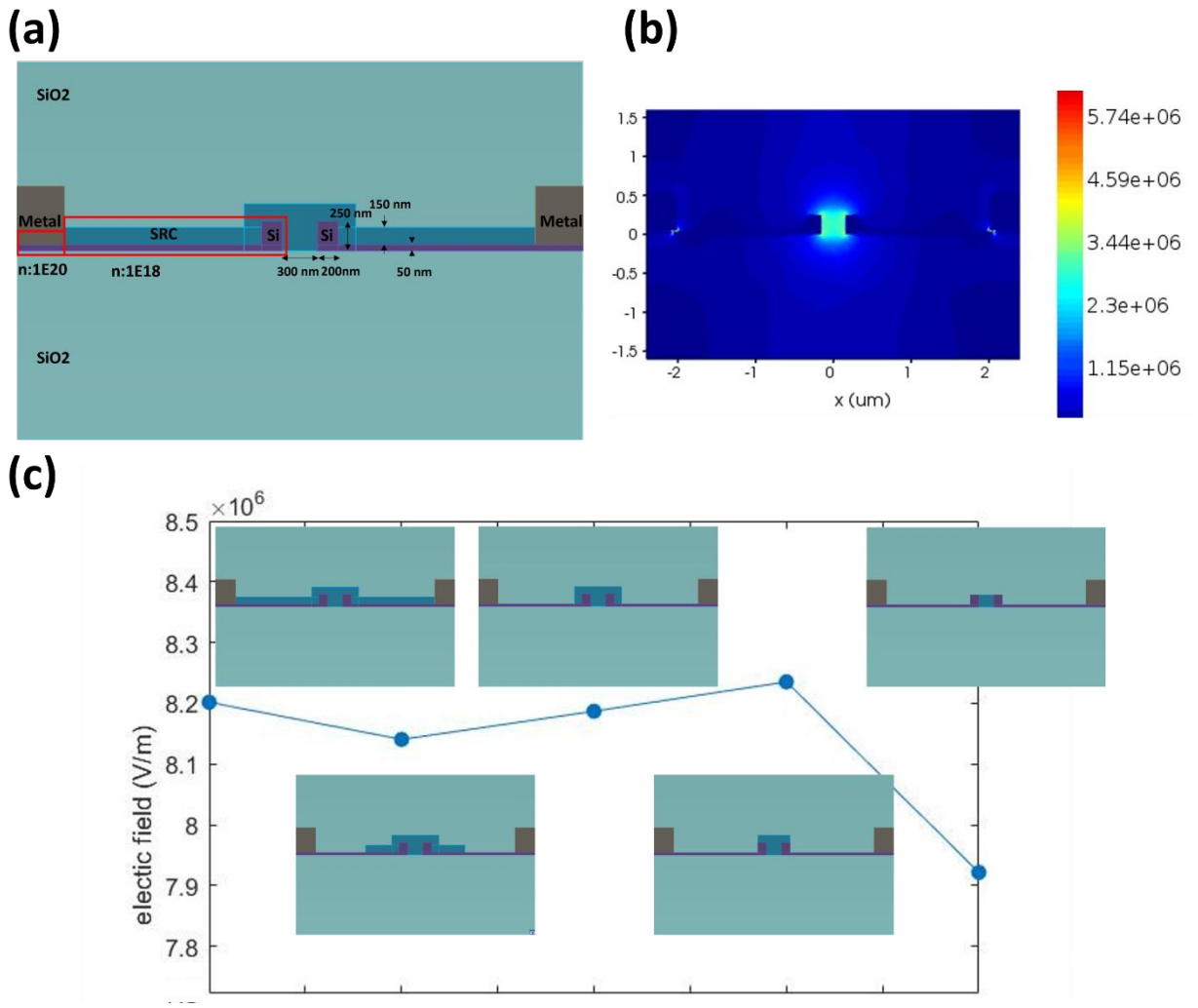

Figure 5.1 (a) The device configuration setting in the electric field distribution simulations. Waveguide dimensions are set at 250 nm × 200 nm, while the slot width spans 300 nm, the slab height reaches 50 nm, and the SRC layer thickness is set to be 150 nm (b) A simulation of electric field distribution showing that most of the electric field concentrates in the slot area. (c) Simulated average electric field across the slot area with different SRC cladding arrangements.

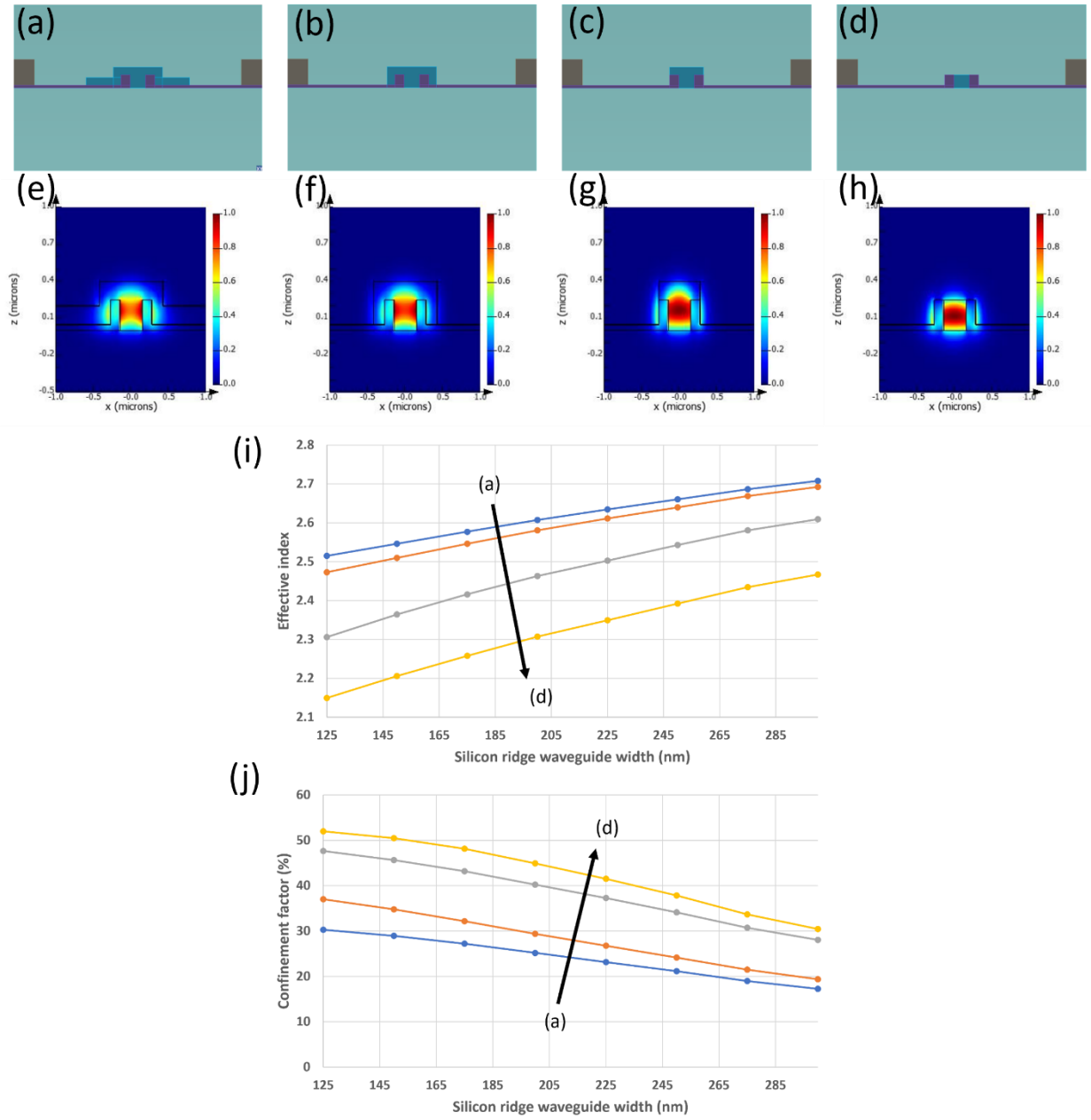

Figure 5.2 (a) – (d) SRC slot and cladding structures setting in the Lumerical MODE simulation. (e) - (h) Simulated fundamental TE mode profile for the different SRC slot and cladding structures. (i) Corresponding simulated effective index of the fundamental TE mode for the different SRC slot structure and the silicon ridge waveguide width. (j) Simulated confinement factor of the fundamental TE mode to the slot area for the different SRC slot structure and the silicon ridge waveguide width.

Subsequently, we delved into the study of optical mode profiles across various device structures using Lumerical MODE solution. As depicted in **Figure 5.2(a)-(d)**, diverse SRC slot and cladding configurations are examined in the simulations, while **Figure 5.2(e)-(h)** show the corresponding simulated fundamental TE mode profiles for each distinct structure. Notably, the optical mode field's behavior differs from the DC electric field, with increased SRC cladding coverage giving rise to a more extended distribution that leads to reduced confinement of the optical mode within the slot. This observation is reinforced by **Figure 5.2(j)**, which highlights the increasing enhancement in mode confinement as the structure evolves from (a) to (d). The heightened mode confinement in the latter structures results in a greater interaction of light with the active material SRC, consequently inducing a more pronounced phase shift through the application of the DC Kerr effect. A similar insight is gleaned from **Figure 5.2(i)**, where we observe a decline in the effective index of the mode as the structure progresses from (a) to (d). This is attributed to the optical mode becoming more confined within structure (d), leading to a heightened interaction with the lower index SRC material.

Further investigation delves into the impact of silicon ridge waveguide width on the optical mode profile. **Figures 5.2(i)** and **Figure 5.2(j)** corroborate that an increase in silicon ridge waveguide width correlates with reduced mode confinement. Finally, we turn our attention to investigating the impact of different silicon slab heights on the optical mode. The outcomes are illustrated in **Figure 5.3(a)** and **Figure 5.3(b)**. Notably, as the silicon slab thickness increases, the mode exhibits a greater interaction with the silicon material, resulting in reduced confinement within the slot area. As can be seen from the simulation in **Figure 5.3**, when compared to the influence exerted by the silicon ridge waveguide width and the different SRC cladding structures, the slab height has a smaller impact on the optical mode profile.

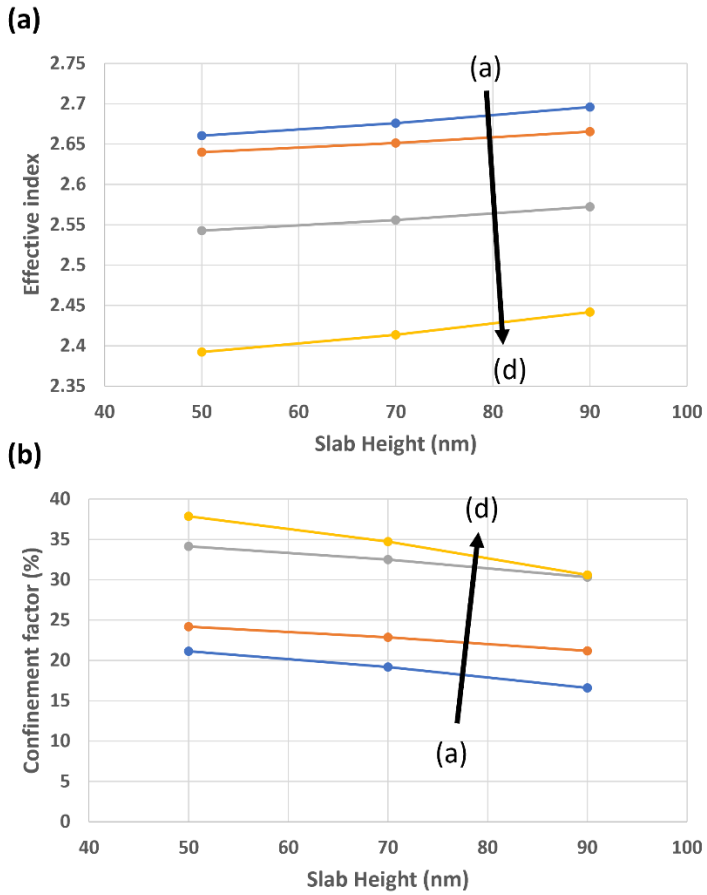

Figure 5.3 Simulated (a) effective index and (b) confinement factor of the fundamental TE mode for varying slab height for the four SRC cladding structure.

The insights gained from our exploration of mode profiles across varied structures provide valuable guidance for understanding device behavior. Taking into account our nano fabrication capabilities, we have opted to adopt structure (b) from **Figure 5.2** for our SRC cladding. This choice aligns with its greater feasibility in real-world implementation. This structure is used in the following modulator efficiency simulation.

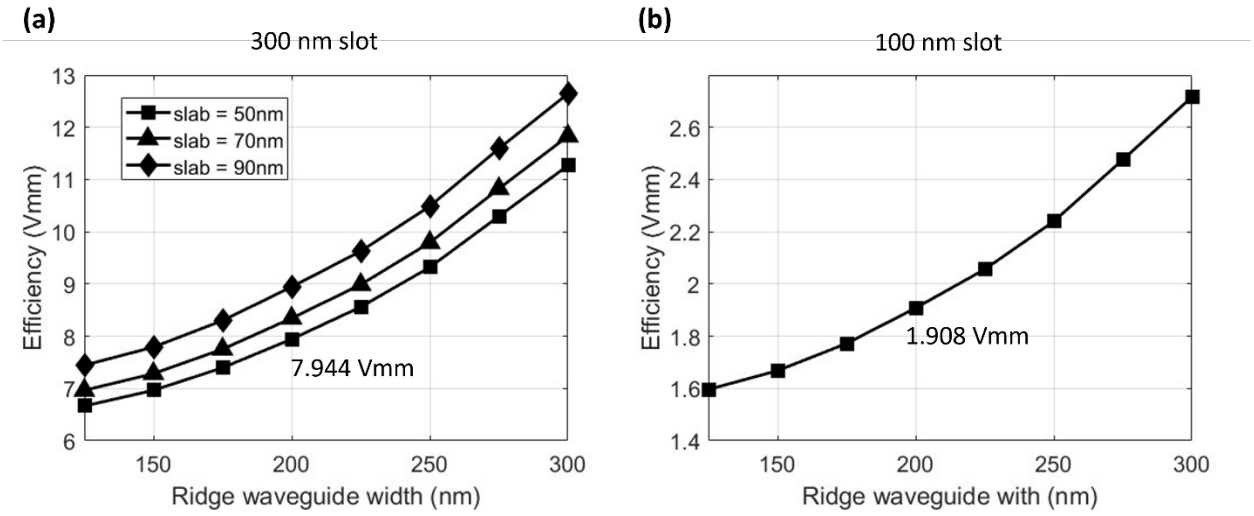

Figure 5.4 Simulated SRC/Silicon hybrid waveguide modulator modulation efficiency for (a) 300 nm slot and (b) 100 nm slot structures.

Next, we embark on combining the simulations of DC electric field and optical mode behavior to unveil the convoluted structure-property relationship governing the SRC/silicon hybrid waveguide Mach–Zehnder modulator. For our simulations, we operate under the assumption that the SRC slot is applied under an electric field approaching its breakdown threshold. This choice enables us to harness the full potential of the DC Kerr effect, resulting in the maximal induction of $\chi^{(2)}$ within the material. The simulation follows a systematic series of steps outlined below:

1. DC Electric Field Simulation: The DC electric field distribution across the slot is simulated using the Lumerical Charge solver. This outcome serves as the foundation for subsequent correlation with the material's index change, accomplished through **Equation (15)**. The $\chi^{(3)}$ value employed in the simulation, $6.9 \times 10^{-19}\ \mathrm{m^2/V^2}$, is extracted earlier from measurements of the DC Kerr effect.

2. Effective Index Calculation: Employing the Lumerical FDE solver, the effective index of the fundamental TE mode of the slotted waveguide is computed before and after the application of DC voltage. This step provides key insights into the mode's behavior under voltage modulation.
3. Transmission Spectra Calculation: The transmission spectra of the Mach–Zehnder interferometer (MZI) can be calculated using the equation:

$$T = 0.25 \times \mathrm{abs}\left(e^{-i\beta_1 L} + e^{-i\beta_2 L}\right) \quad (25)$$

   Here, $\beta = 2\pi n_{eff}/\lambda$ which represents the propagation constant, β_1 and β_2 denote the propagation constants of the optical mode before and after voltage application, and L denotes the arms' length of the MZI.
4. Modulation Efficiency Determination: The modulation efficiency is derived by evaluating the length-voltage product of the π phase shift obtained from the transmission spectra.

The outcomes are visually presented in **Figure 5.4(a)** and **Figure 5.4(b)**, showcasing a good alignment with the prior findings derived from the optical mode simulations. Evidently, a correlation exists between the silicon ridge waveguide dimensions and the modulator's efficiency. A clear trend emerges, where a narrower silicon ridge waveguide leads to better modulator efficiency. Similarly, the silicon slab thickness inversely influences the modulator's efficiency – thinner slabs result in more efficient modulation.

Furthermore, we extended our inquiry to investigate the modulation efficiency across different slot width designs. Intriguingly, we observed that the slot width plays a pivotal role in determining the modulation efficiency. A narrower slot width yields benefits not only from

enhanced optical confinement within the slot but also from the ability to reach the breakdown electric field with a lower applied DC voltage. This dual advantage contributes to improved modulator efficiency. To illustrate, a comparison of the results between two structures with 100 nm and 300 nm slot widths, maintaining the same silicon ridge waveguide width and slab height, is depicted in **Figure 5.4**. Remarkably, this comparison highlights a significant enhancement in modulation efficiency – from 7.944 Vmm to 1.908 Vmm – emphasizing the profound impact of slot width on the modulator's performance.

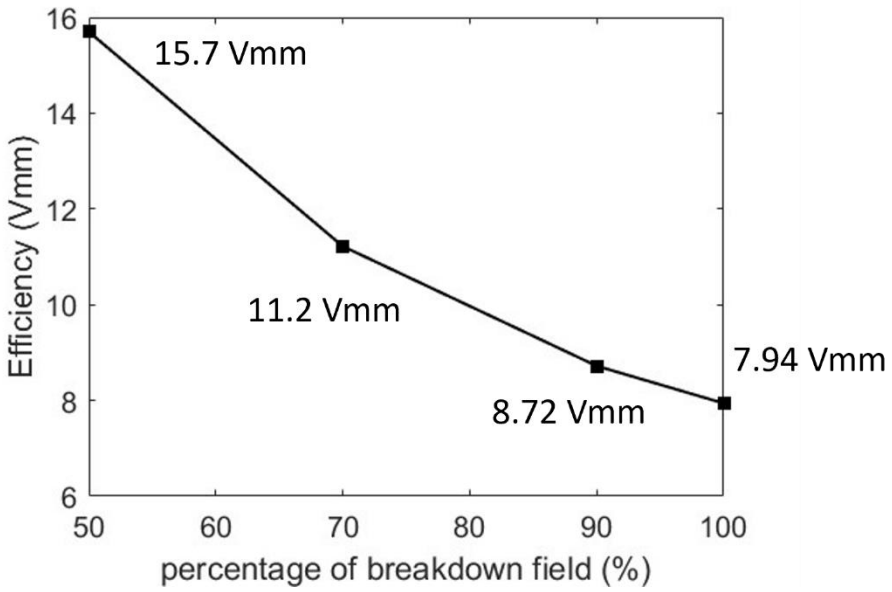

Figure 5.5 Simulated SRC/Silicon hybrid waveguide modulator modulation efficiency under different applied electric field.

Our investigation extends further to examine how the magnitude of applied DC electric field influences modulation efficiency. The insights are depicted in **Figure 5.5**, focusing on a 200 nm ridge and 300 nm slot waveguide configuration. Evidently, a nearly linear relationship emerges between the efficiency and the magnitude of the applied DC electric field. Intriguingly, this

analysis highlights the pronounced impact of the electric field's strength on modulation efficiency. When applying 100% of the breakdown field, the resulting modulation efficiency registers at 7.94 Vmm. However, with only 50% of the breakdown field applied, the efficiency undergoes a substantial drop to 15.7 Vmm. This clear correlation underscores the critical role of maintaining a high electric field across the slot.

5.3 Design and validation of essential components

5.3.1 Slot filling test

Building upon our previous discussion, the width of the slot has emerged as a pivotal determinant of modulator efficiency. In this section, we embark on the investigation of the capability of PECVD to effectively fill material into a narrow slot. For this endeavor, we curated a series of slot structures, with slot widths spanning from 150 nm to 500 nm. Our objective was to discern the extent to which PECVD could proficiently fill materials within these narrow slots.

Upon conducting our experiments, we discerned that successful material filling was achieved for slot widths exceeding 250 nm, where the aspect ratio remained at 1:1. However, as the slot width narrowed down to 200 nm, we began to observe the emergence of gaps within the slot region, indicative of incomplete material filling. The SEM image displayed in **Figure 5.6(a)** captures the 200 nm and 250 nm slots filled with SRC. In the case of the 200 nm slot, a discernible gap within the slot area is observable. To enhance the reliability of our findings, we are inclined to favor a slot width of 300 nm, as it provides an extra margin of safety. This assessment is further reinforced by the cross-sectional depiction presented in **Figure 5.6(b)**, which shows a fabricated SRC/silicon slot waveguide featuring a slot width of 300 nm. Notably, the material has been effectively infused into the slot, although a residual "keyhole" presence atop the slot region

remains. To address this, further optimization is warranted through adjustments in the fabrication process. One potential avenue involves introducing a slope to the silicon waveguide, achieved through refining the etching recipe. This strategic adjustment could potentially mitigate the slot close up issue and bring about a more refined result.

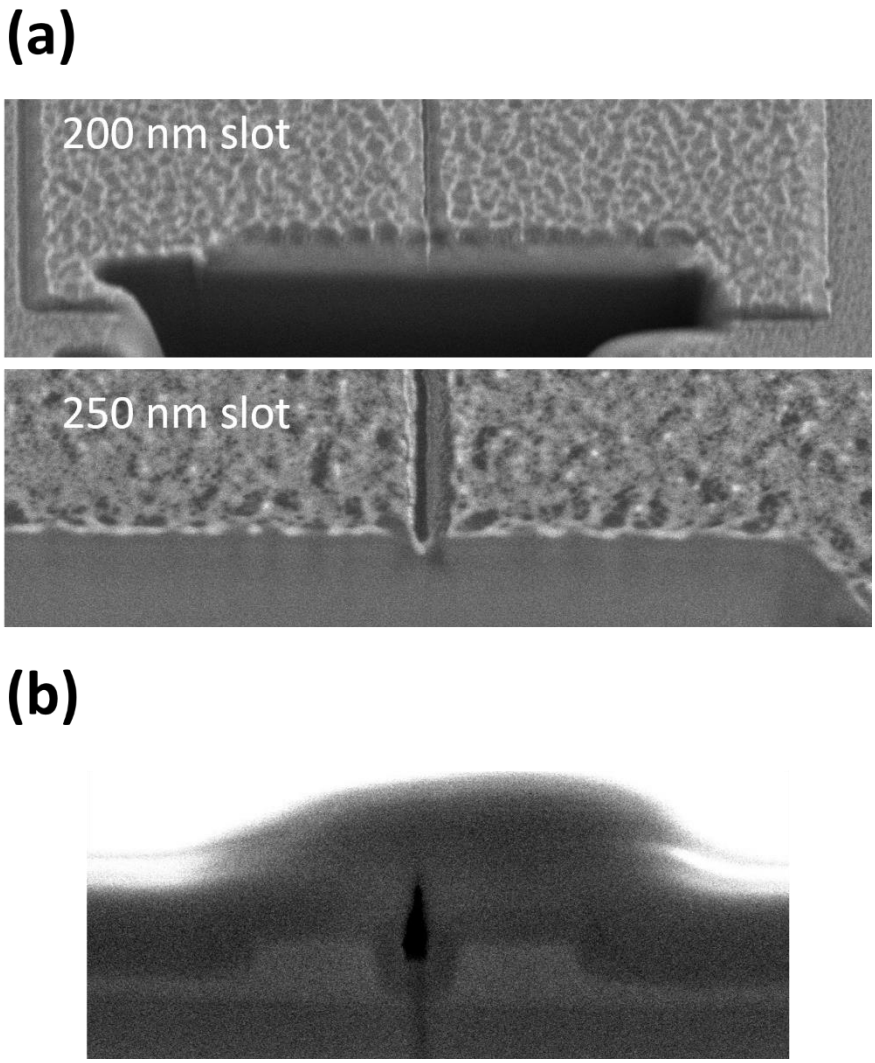

Figure 5.6 (a) SEM image of the 200 nm and 250 nm slot filled with SRC. (b) A SEM image of the cross section of a 300 nm slot waveguide filled with SRC and SiO_2 layer is clad on top.

5.3.2 Strip to slot waveguide converter

In our Mach-Zehnder modulator (MZM) design, a seamless transition from a silicon strip waveguide to an SRC/silicon hybrid slot waveguide is of paramount importance to minimize any additional loss. To achieve this, we have devoted our efforts to developing a multimode interferometer (MMI) based strip-to-slot waveguide converter, which we'll discuss in detail.

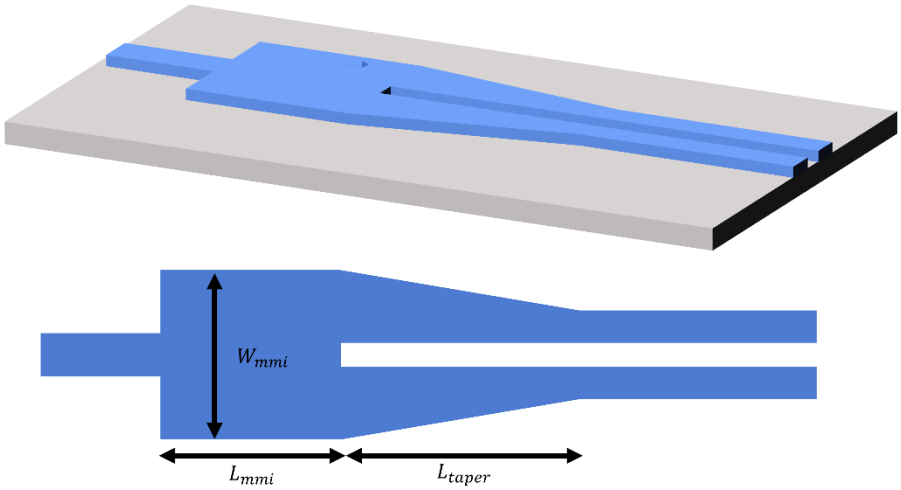

Figure 5.7 3D schematic and the top view of the MMI-based strip to slot waveguide converter (not to scale).

Illustrated in **Figure 5.7**, our proposed strip-to-slot converter is comprised of a 1 X 2 MMI and slot tapers. Key design parameters are showcased in the top view of the converter configuration. Specifically, W_{mmi} represents the MMI width, L_{mmi} corresponds to the MMI length, and L_{taper} signifies the length of the slot taper. Throughout our simulations, we maintain the device layer at 250 nm and the strip waveguide width at 500 nm. Considering the slot filling capacity, the slot width is set at 300 nm, and it's filled with SRC material.

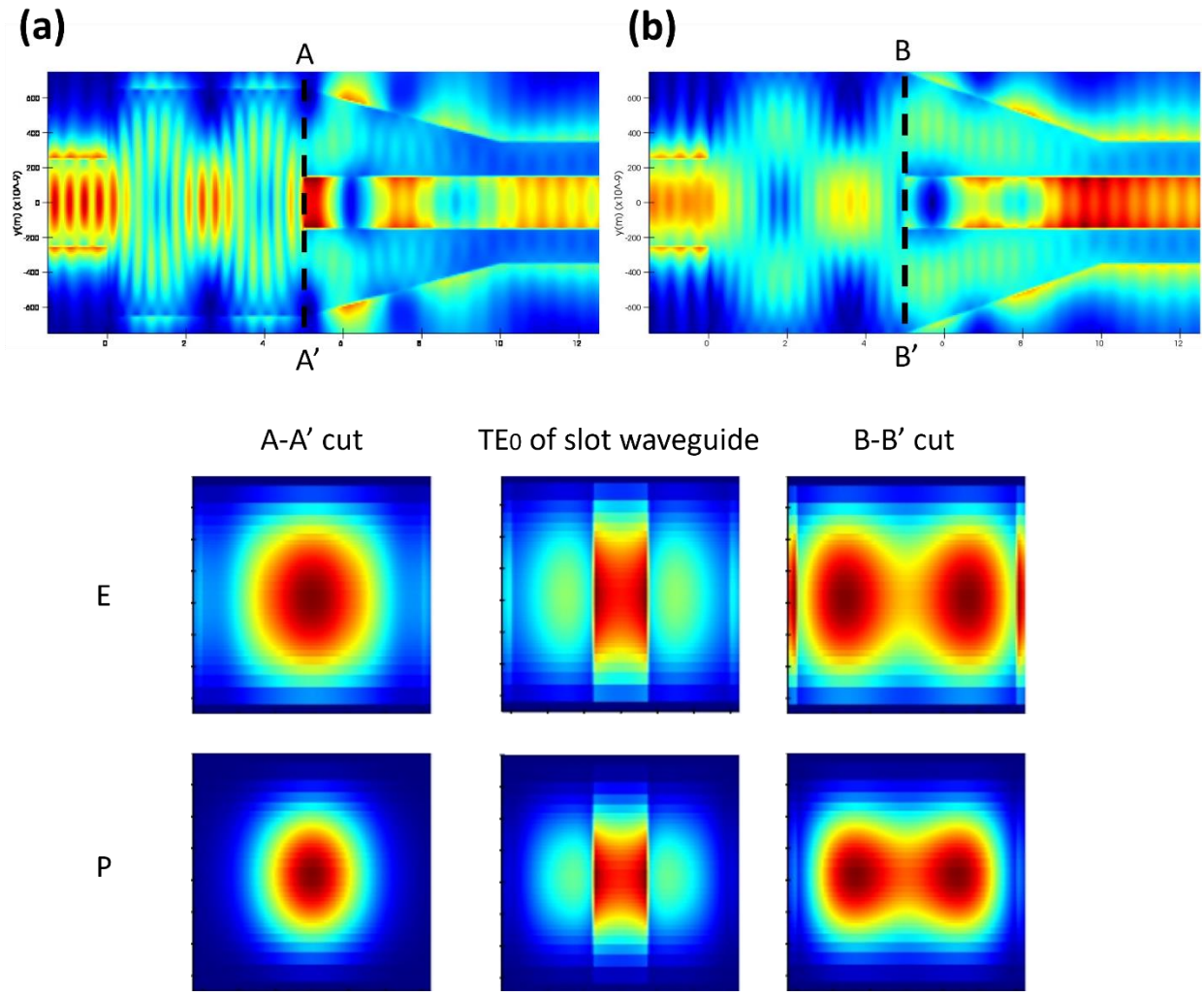

Figure 5.8 Comparison of optical field distribution in two MMI structures with the same length and different MMI width and the eigenmodes in slot waveguide: (a) W_{mmi} = 1.1 μm and (b) W_{mmi} = 1.5 μm. P indicates optical power flow density and E indicates electric field.

Figure 5.8 (a) and **Figure 5.8 (b)** highlight how the incident optical mode field generates single or multiple images at periodic intervals along the propagation direction. The number of optical modes is tied to the MMI width, with the possibility of controlling this through MMI width adjustments. The periodicity is determined by both the MMI width and length. Notably, when comparing the 2-fold image (B-B' cut in **Figure 5.8(b)**) with the fundamental TE mode within a

slot waveguide, a high degree of similarity in the mode profile is evident. This suggests the feasibility of achieving a seamless transition of optical power from the MMI to the slot waveguide. As depicted in **Figure 5.8 (a)** and **Figure 5.8 (b)**, a comparison of power conversion at two different transition points in the single and two modes regions reveals higher power delivery in the latter case. This discrepancy is attributed to the substantial mode mismatch between the single mode and the slot mode, contrasting with the comparatively smaller mismatch between the two-fold image and the slot mode.

We leverage a two-dimensional FDTD method to simulate the power transition across various MMI structures. Two converters are incorporated into the simulation to model the power transition from the strip waveguide to the slot waveguide and back to the strip waveguide. The outcomes, as depicted in **Figure 5.9**, showcase numerous combinations yielding notably high conversion efficiencies. Importantly, we affirm that the fabrication tolerance is sufficient for these configurations. Selecting $W_{mmi} = 1.4$ μm and $L_{mmi} = 1.7$ μm based on simulation results, we identify a specific structure capable of achieving a remarkable 93% power conversion efficiency, translating to 96.5% for a single converter.

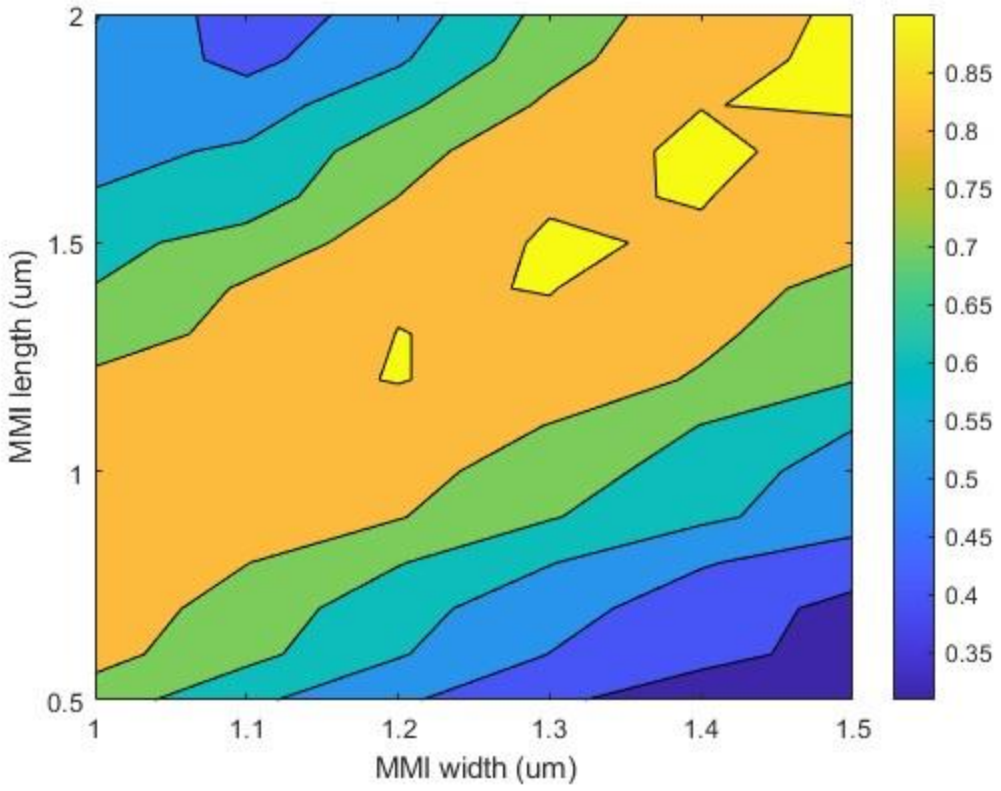

Figure 5.9 Simulated optical power transmission for different combination of MMI width and MMI length. For this simulation, the slot tapers are set to be long enough to adiabatically transfer the power into slot mode.

Another crucial design parameter is the slot taper length, as depicted in **Figure 5.7**. Our objective is to design a slot taper that adiabatically transfers the two modes from the MMI to the slot waveguide while minimizing additional propagation loss. Through further two-dimensional FDTD simulations, we evaluate the power transition with varying taper lengths. Employing consistent MMI dimensions ($W_{mmi} = 1.4$ μm, $L_{mmi} = 1.7$ μm), we deduce from the results shown in **Figure 5.10** that taper lengths exceeding 10 μm achieve optimal power transition efficiency.

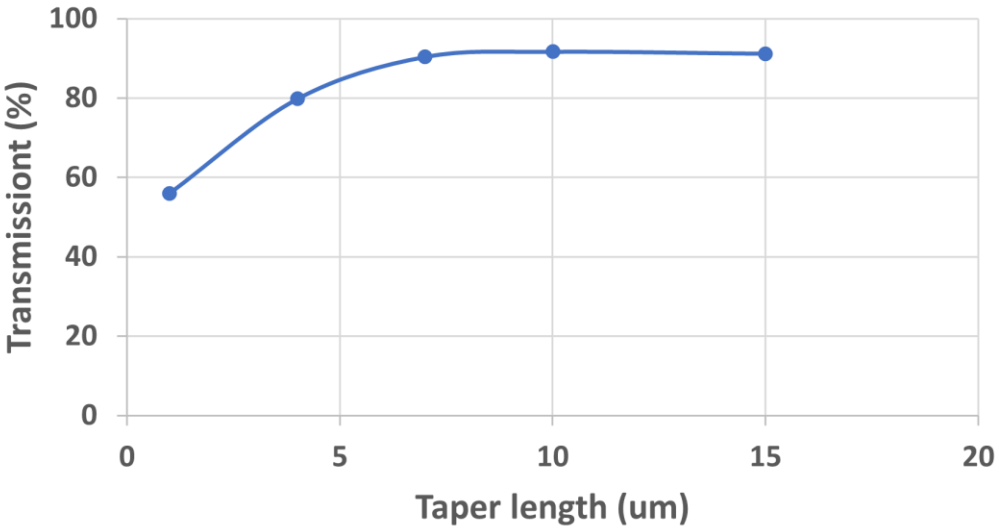

Figure 5.10 Simulated optical power transmission for different slot taper lengths.

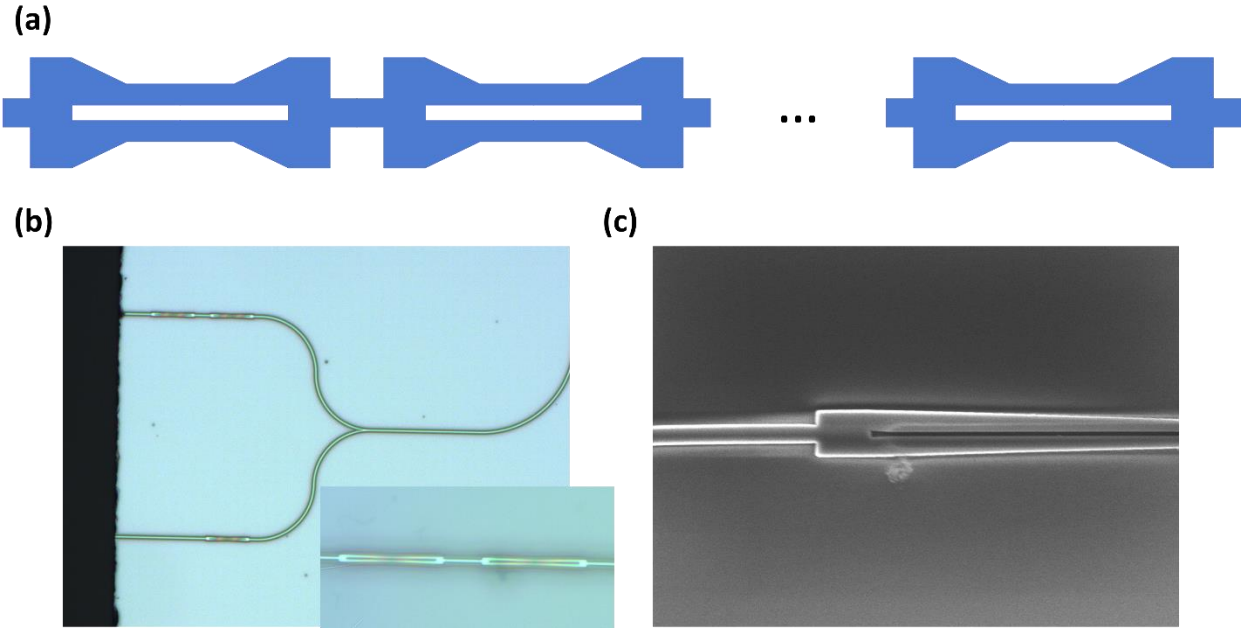

Figure 5.11 (a) Schematic of the layout of the cascade converters (not to scale). (b) OM image showing the fabricated cascade converters. The inset shows a zoom-in image of the converters. (c) SEM image of single converter.

The devised converters are physically realized on a SOI wafer, featuring a top silicon layer with a thickness of 250 nm and an underlying buried oxide layer measuring 3 μm in thickness. Fabrication entails EBL and RIE, followed by the deposition of a 2 μm SiO2 cladding atop the waveguides. Our design encompasses 2 to 4 pairs of converters, a setup aimed at evaluating the loss characteristics of these converters. The arrangement of cascaded converters is depicted in **Figure 5.11(a)**, and **Figure 5.11(b)** provides an optical microscope image showcasing a fabricated waveguide featuring the converters within its two arms. Additionally, **Figure 5.11(c)** offers a SEM image of a single strip-to-slot converter.

The obtained measurement results are presented in **Figure 5.12**. The waveguides are tested under TE mode. We normalized the output power to the one pair of converters arm. Through a comparative analysis of output power across various numbers of converter pairs, we discern that by adding one pair of converters will introduce 0.4589 dB of loss. The conversion efficiency is then estimated to be 90% for a pair of converters and 95% for a single converter. Importantly, these measurement results align well with our simulation outcomes.

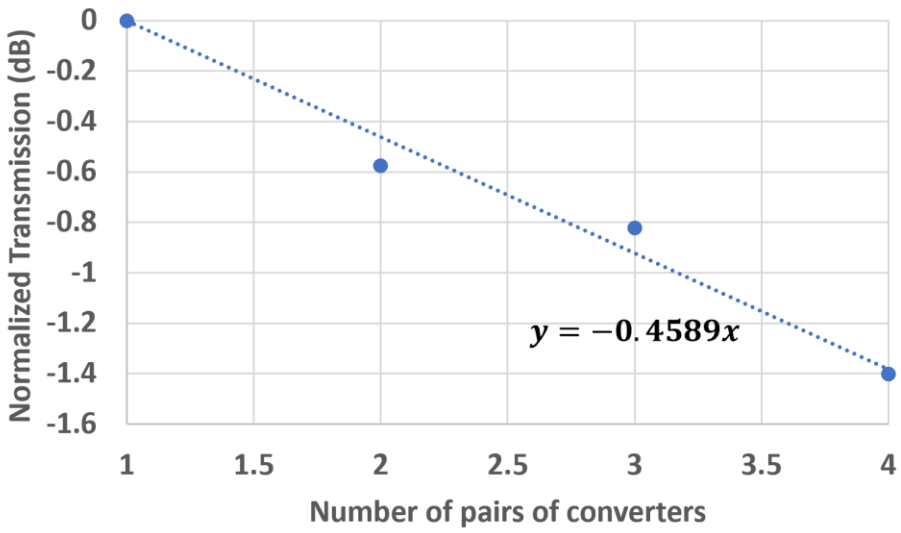

Figure 5.12 Measurement results of the transmission power for different number of converter pairs.

5.3.3 Electric field test

Drawing from our earlier simulations, we have ascertained the pivotal role played by the capacity to sustain high electric fields in enhancing modulator performance. To validate the ability to hold the electric field, we devised a series of test structures mirroring the active region in the modulator. These structures encompass the SRC/silicon hybrid slot configuration, silicon slab, and the electrode. The layout for these 25 test structures is presented in **Figure 5.13**, while **Figure 5.14** outlines the sequential fabrication process flow to create these test structures. The structure dimensions are all set to be our targeting waveguide design where the silicon ridge is 200 nm x 250nm, the slot width is 300 nm and the SRC layer thickness is 150 nm to fill up the slot region. The dimensions are shown in **Figure 5.14**.

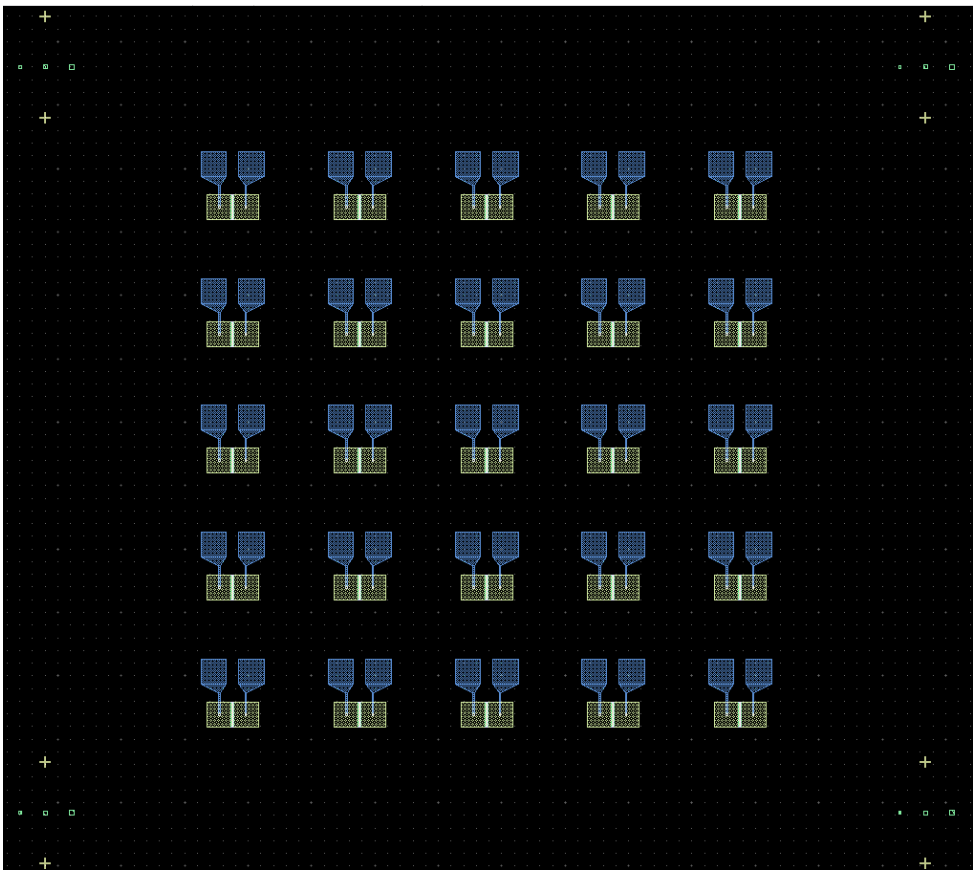

Figure 5.13 Layout of the electric field test structure

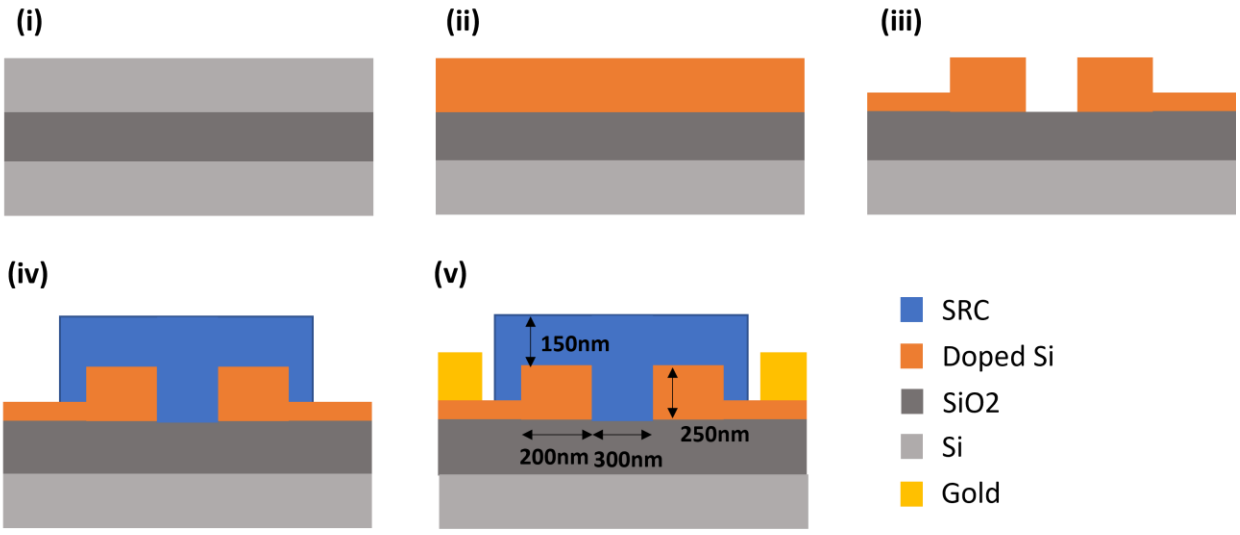

Figure 5.14 Schematic of the process flow for the test structures. (i)-(iii) Silicon slot structure formation. (iv) SRC slot formation. (v) Electrode formation.

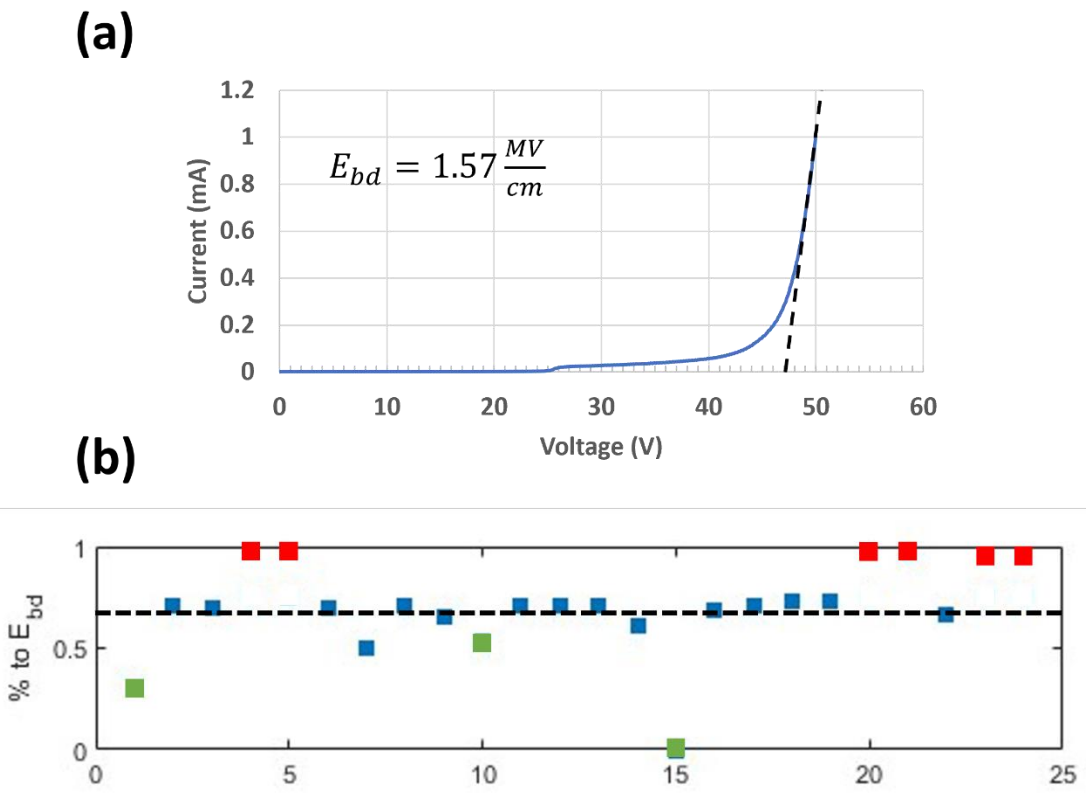

Figure 5.15 (a) I-V test result for a device that reach 1.57 MV/cm of breakdown electric field which is around 71% of material breakdown. (b) Summary of the electric field test results for 25 devices. Red square markers identify the devices that reach the material breakdown and green square markers identify the device that has obvious defect can form leakage pathway. The results show 20 out of 22 devices can reach 70% of the breakdown electric field.

The test results are shown in **Figure 5,15**. **Figure 5.15(a)** shows the I-V measurement results for a device. We estimate the breakdown voltage to be around 47 V by fitting the rise of the I-V curve. The estimate breakdown field for the device is 1.57mV/cm which is around 70% of the material breakdown electric field. The breakdown electric field for all the devices are captured in the same way. A comprehensive summary of the test outcomes is presented in **Figure 5.15(b)**. Within this depiction, red square markers denote devices capable of reaching the material's breakdown electric field, while green square markers identify devices exhibiting discernible

defects in the slot structure, resulting in a leakage pathway formation. Our observations reveal that 6 devices manage to attain the material's breakdown electric field as measured before. Moreover, among the devices without evident defects, a substantial 90% (20 out of 22) can achieve 70% of the material's breakdown electric field – this threshold is demarcated by the black dotted line in the figure. Relating this to our prior simulations, discussed in the preceding section, applying 70% of the breakdown field to our designed structure, we are targeting a modulation efficiency of 11.2 Vmm.

5.3.4 Slot waveguide propagation loss estimation and MZM

An additional parameter needs to be validated pertains to the propagation loss exhibited by the SRC/silicon hybrid slot waveguide. To quantify this aspect, we embarked on fabricating a set of 1 X 2 waveguides. Within each of the output arms, we engineered SRC/silicon slot waveguides of differing lengths. By assessing the output power from these two arms, we could derive an estimation of the waveguide propagation loss. The OM image of the fabricated waveguides is captured in **Figure 5.16**. A zoomed-in view reveals the SRC/silicon slot waveguides in the output arms, showcasing a length difference of 100 μm between them. In the extended waveguides, illustrated in the complete layout, the length variations span 200, 300, 400, 500, and 600 μm. A closer examination through an optical microscope zoomed image highlights the fabricated SRC/silicon slot region within one arm.

Figure 5.16 presents the obtained measurement results. In **Figure 5.17(a)**, the output from a single device is visibly observed on the infrared (IR) card and captured by a CCD camera. Employing a Power meter, we gauge the output power from both arms and subsequently estimate the loss incurred. The summarized outcomes are depicted in **Figure 5.17(b)**. Through fitting

techniques, we deduce the propagation loss to be approximately 4.5 dB/mm. Notably, this loss magnitude is notably high when compared to conventional waveguide materials. For context, our previous assessment of the SRC waveguide yielded a loss of 6.2 dB/cm. We postulate that this discrepancy may arise from fabrication imperfections. Further in-depth exploration is required to ascertain and validate this supposition.

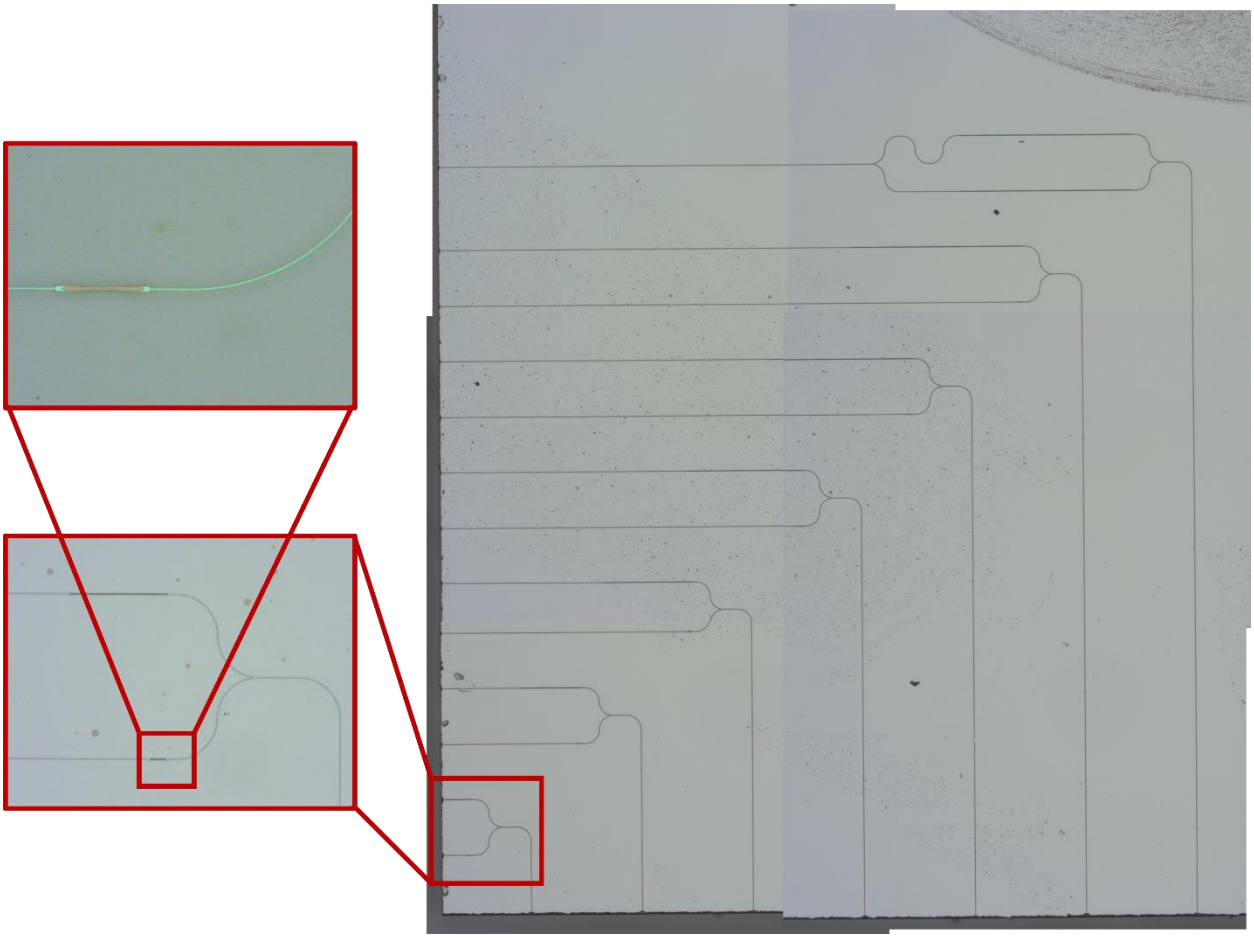

Figure 5.16 OM images showing the layout of the slot loss test devices. The zoom-in picture shows the length difference in the two arms and the SRC/silicon slot region in single arm.

(a)

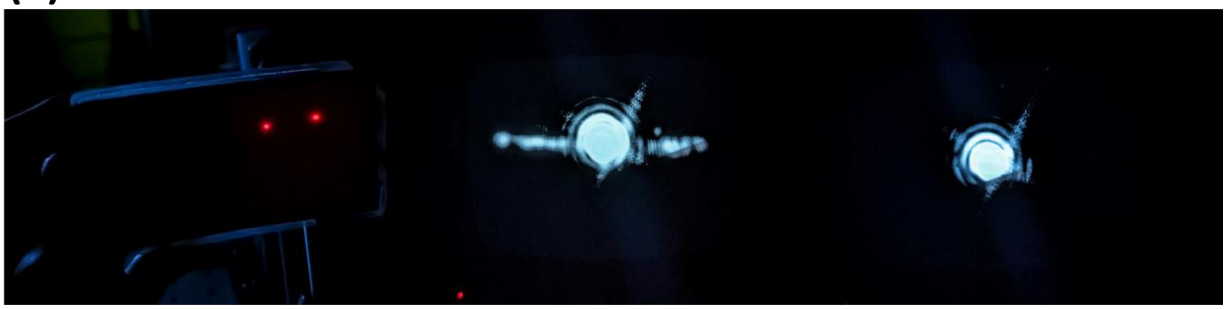

(b)

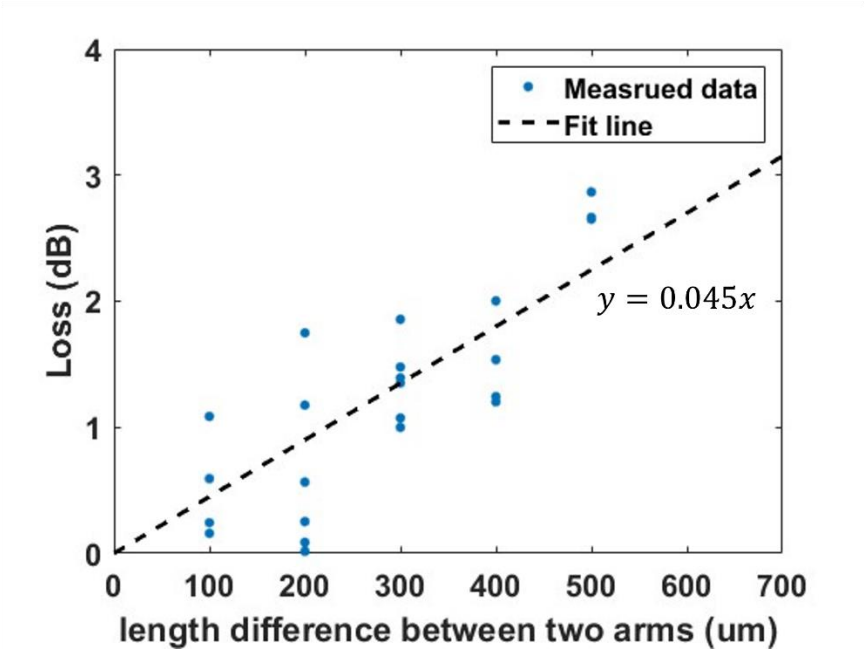

Figure 5.17 Slot loss measurement (a) The two outputs are detected on the IR card and the CCD camera simultaneously. (b) The measured loss from different slot length. Fitted results showing an estimation of 4.5 dB/mm loss.

Furthermore, we have incorporated a MZI structure into our evaluation to validate the device design, as it closely resembles the final configuration of the Mach–Zehnder modulator. In each of the MZI arms, we have integrated 700 μm of the SRC/silicon slot waveguide. By introducing an imbalanced arm setup, we can observe the power transfer across the transmission spectrum of the MZI while varying the wavelength. The results are depicted in **Figure 5.18(a)**,

illustrating the transmission spectrum of the imbalanced arm MZI across the wavelength range of 1540 nm to 1560 nm. We observed the power as the wavelength is swept. For a more detailed view, the extinction ratio of approximately 23 dB is displayed in **Figure 5.18(b)** via a finer wavelength scan.

These measurements collectively affirm the operational viability of the designed MZM waveguide structure. The observed power transfer and extinction ratio validates that our MZI configuration is poised to function effectively as intended.

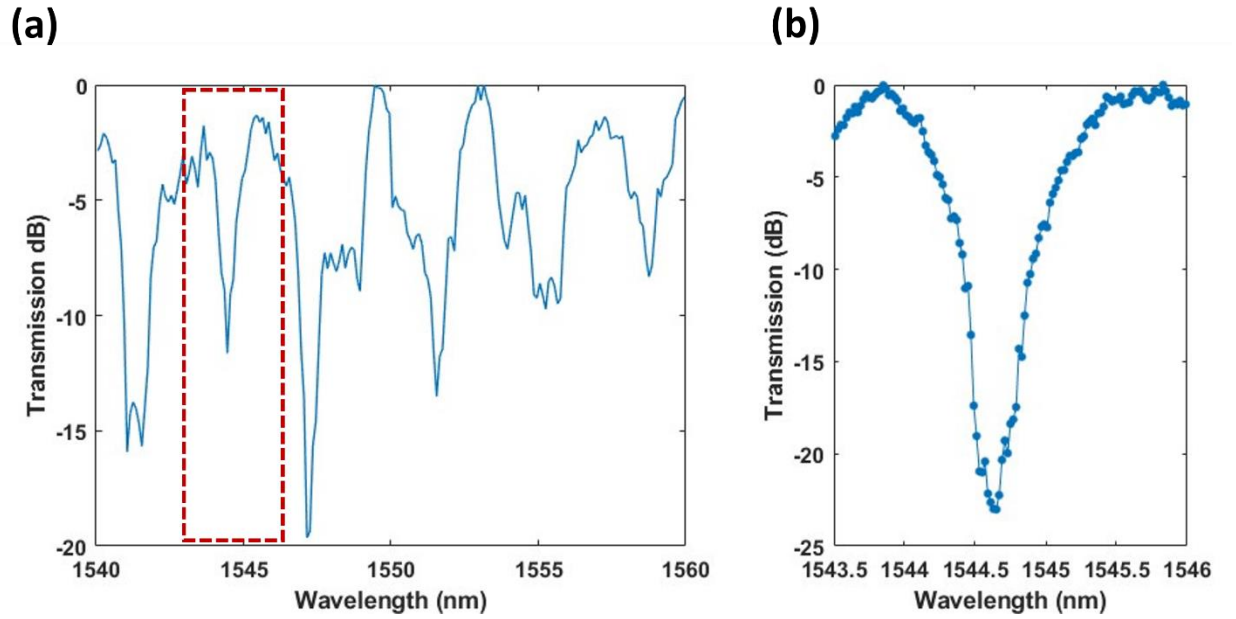

Figure 5.18 (a) The transmission spectrum of the imbalanced arm MZI from 1540 nm to 1560 nm. (b) Single peak with a finer scan from 1543.5 nm to 1546 nm.

5.4 Full modulator design overview

The full design of the SRC/Silicon hybrid waveguide modulator is illustrated in **Figure 5.19**. **Figure 5.19(a)** shows the 3D schematic of the modulator and **Figure 5.19(b)** shows the top view and the cross-section view of the proposed modulator design showing the dimension of each design parameter. According to our simulation that discussed in previous section, to strike the balance the easiness of real-life implementation and the efficiency, we design our silicon ridge waveguide width to be 200 nm × 250 nm and the slot width to be 300 nm. The thickness of the SRC layers is designed to be 150 nm to fill up the slot area. The proposed structure has the modulation efficiency of 7.94 Vmm under 100% of the material breakdown electric field applied, and 11.2 Vmm under 70% of the material breakdown electric field applied. From our electric field test, we are confident that we can apply the electric field up to 70% of the breakdown on this specific structure. The length of the active region is proposed to be 2.5 mm and the corresponding V_π is expected to be 4.48 V under 70 % of breakdown electric field poling. The estimated insertion loss for the slot waveguide is ~ 11.25 dB for this specific length. The MMI based strip to slot converter are put right before and after the slot area to effectively transfer the silicon strip waveguide mode to SRC/Silicon slot waveguide mode. The design MMI width is 1.4 μm and the length is 1.7 μm. From our loss experiment on the converter, we should expect an additional 0.46 dB loss for a pair of converters which leads to 11.65 dB total insertion loss for the device.

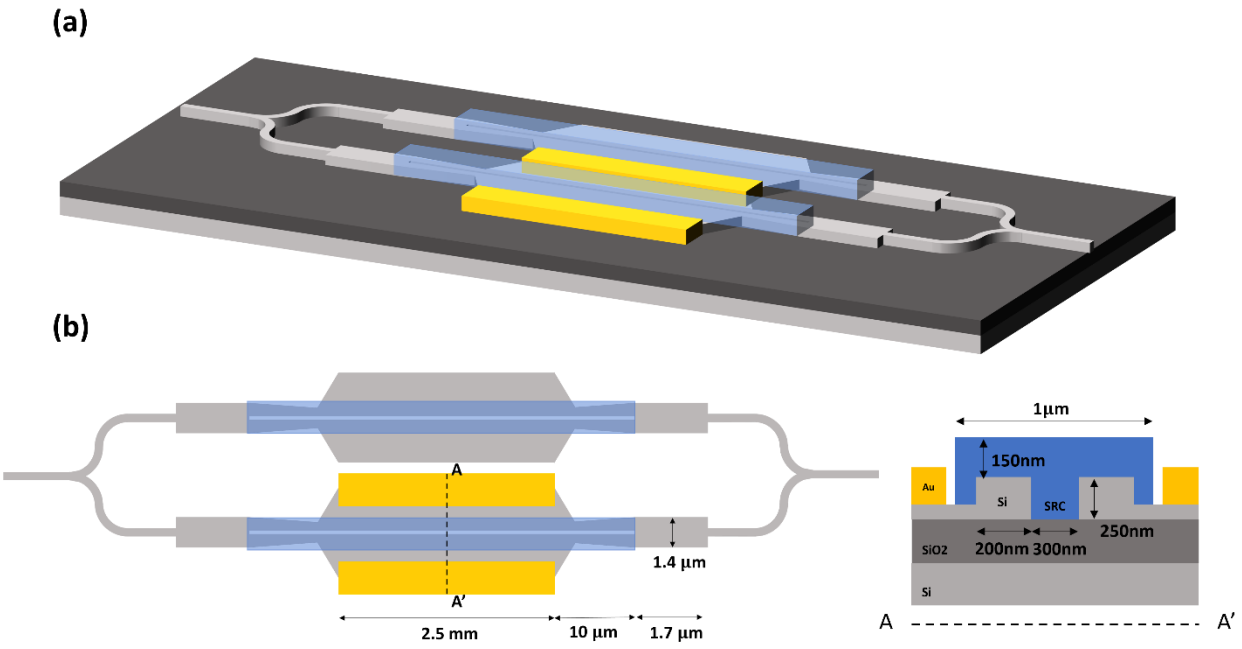

Figure 5.19 (a) 3D schematic of the proposed SRC/Si Hybrid waveguide modulator design. (Not to scale) (b) Top view and the cross-section view of the proposed SRC/Si Hybrid waveguide modulator design showing the dimension of each design parameter.

5.5 Comparison to the state-of-the-art modulators

Table 5.1 provides an inclusive overview of performance metrics for prevalent optical modulator types within silicon photonics platforms. This encompasses plasma dispersion within silicon, as well as the integration of ferroelectric and organic materials with silicon photonics. Common modulator characteristics including modulation efficiency and the loss α are discussed in this table. A figure of merit $V_\pi\alpha$ is also introduced for comparison. This compilation allows us to discern distinct characteristics of each modulator type.

A careful analysis unveils that plasma dispersion modulators exhibit commendable modulation efficiency. However, they grapple with elevated loss due to the requisite high carrier

concentration for effective modulation. Moreover, as aforementioned, the operational speed of such devices becomes constrained by the RC time constant. In contrast, integrating $\chi^{(2)}$ materials with silicon photonics strikes a favorable balance between loss and efficiency. Nonetheless, the integration process for these materials with silicon is presently intricate and challenging.

The SRC/Si hybrid waveguide modulator emerges as an enticing alternative, boasting comparable modulation efficiency (0.2 V·cm) according to our simulation. Its integration potential is also noteworthy, facilitated by a simplified approach. Additionally, DC Kerr effect showcases the potential for high-speed operation, offering a multifaceted solution to existing modulator limitations. The innovative integration scheme holds the potential to address the current constraints encountered in modulator technologies. Certainly, it's worth acknowledging that the estimated loss of this modulator type falls within a range comparable to plasma dispersion counterparts and is somewhat higher compared to modulators harnessing the Pockels effect. However, in considering the materials intrinsic loss and the operating principle, we believe the loss could be drastically improved by optimizing the fabrication process.

Table 5.1 Performance matrix for the plasma dispersion, ferroelectric and organic high-speed modulators in silicon photonic platform

Scheme	Principle	Modulation efficiency (V·cm)	Loss (dB/cm)	FOM (VdB)
Si [96]	Carrier injection	0.058	74	4.3
Si [97]	Carrier accumulation	0.16	35	5.6
Si [98]	Carrier depletion	2.2	9.4	20.7
$LiNbO_3$ Bulk [99]	Pockel's effect	10	1.5	15
BTO on SiPh [100]	Pockel's effect	0.2	6	1.2
$LiNbO_3$ on SiPh [101]	Pockel's effect	2.2	~1	2.2
PZT on SiPh [102]	Pockel's effect	1	1	1
Organic on SiPh [6]	Pockel's effect	0.032	37.5	1.2

5.6 Conclusion

In summary, our work presents a SRC/Silicon hybrid slot waveguide structure that can effectively utilize the DC Kerr effect for optical modulation. Throughout this chapter, we have shown our endeavors in developing this optical modulator scheme.

In the first part of the chapter, our focus was on comprehensive simulation studies that explored the intricate relationship between the modulator's structural properties and its performance characteristics. Through these investigations, we have arrived at the noteworthy conclusion that the slot width and the ability to withstand high electric fields hold pivotal significance in determining the modulator's overall performance.

In the second part of the chapter, we transitioned to practical demonstrations and validations of essential components. Our achievements include showcasing our capability to

effectively infuse SRC materials into nanoscale slots using PECVD, a critical accomplishment for realizing the proposed modulator. Moreover, we successfully designed and evaluated a Strip-to-Slot converter, attaining an impressive conversion efficiency of approximately 95%. Notably, we are also confident in our ability to pole the material under 70% of the breakdown electric field, as evidenced by our electric field tests. Furthermore, our measurements indicate that the estimated loss of the SRC/Si slot waveguide stands at 4.5 dB/mm.

In a culmination of our efforts, we introduced a MZI structure that serves to validate the complete waveguide design. The successful demonstration of this MZI structure lends substantial support to our vision of seamless integration and operation of active devices in the future.

Chapter 5 contains unpublished material coauthored with Li-Yang Sunny Chang, Steve Pappert, and Paul K. L. Yu. The dissertation author was the primary investigator of this chapter.

CHAPTER 6: SUMMARY AND FUTURE WORKS

Within this dissertation, we introduce a new material, silicon-rich carbide, and investigate its main attributes for integrated photonics applications. The initial part of the dissertation centers on material synthesis and comprehensive characterization of its properties. By tuning the precursor flow ratios in PECVD, we effectively deposit silicon carbide thin films with varied stoichiometry. This endeavor yields insights into material properties relative to silicon content, thereby enhancing the design of optical devices for subsequent exploration of nonlinearity and TOC.

Transitioning to the dissertation's second phase, our focus shifts to silicon-rich carbide waveguide design. Employing FDE methodology, we optimize waveguide structures for single-mode operation while accommodating fabrication tolerances. To enhance coupling efficiency, a fiber-to-chip edge coupler is designed and simulated through FDTD, confirming that an 84% coupling efficiency can be achieved. An estimated propagation loss of 6.2 dB/cm is derived from ring resonator transmission spectra, with room for optimization in fabrication processes. Detailed characterizations follow, including material nonlinearity and TOC assessments via ring resonators. The DC Kerr effect measurement reveals a third-order nonlinearity of 6.9×10^{-19} $\mathrm{m^2/V^2}$, surpassing reported values in stoichiometric silicon carbide by a factor of 7. An induced second-order nonlinearity of 44.9 pm/V is achieved. TOC study, demonstrated through transmission spectrum shifts under varying temperatures, reveals more than a threefold enhancement in silicon-rich a-SiC thin films compared to stoichiometric counterparts. The attained highest TOC of 1.88×10^{-4} ℃ is comparable with that of crystalline silicon.

Finally, we extend our investigation in exploring different possibilities of the devices' implementation. An efficient thermo-optic phase shifter combining a NiCr heater with a silicon-

rich a-SiC micro-ring resonator is designed and validated. This setup achieves thermal tunability of 0.117 nm/mW, equivalent to Pπ of 4.2 mW, which shows the potential for further thermo-optic switch development. Further investigation comes in the form of an SRC/Silicon hybrid slot waveguide, leveraging the DC Kerr effect for optical modulation. Detailed simulations indicate a feasible modulation efficiency of 0.2 $V \cdot cm$ within this modulator configuration. Essential components for the modulator are then designed and validated, with an estimated propagation loss of 4.5 dB/mm for the slot waveguide. Finally, validation of complete waveguide design emerges through the successful operation of the introduced MZI structure, bolstering our vision for the seamless integration and operation of active devices in the future.

Based on the findings of this thesis, several areas of future research can be identified for further investigation. These include:

(1) Developing more compact and efficient SRC thermo-optic switches

(2) Reducing the propagation loss of SRC waveguides

(3) Realizing an efficient, high-speed SRC optical modulator

Exploring the development of more compact and efficient thermo-optic switches is one area that should be addressed. As highlighted in the dissertation, the combination of high TOC and high-power handling capacity exhibited by SRC opens up opportunities for efficient thermo-optic switches, particularly in scenarios demanding high optical power. Micro-ring resonator switches, while compact and energy-efficient in tuning, may not fulfill the need for wide optical bandwidth, which is needed in many emerging applications. The viable alternative lies in the form of MZI structures, offering suitability for broadband tasks. Further compactness can be achieved through folded waveguide implementation. These two avenues warrant further exploration.

Another area of future work includes investigating the root causes behind the higher waveguide propagation loss. There is a big discrepancy of the propagation loss between the SRC waveguide and the SRC/Si slot waveguide. Given inherent material characteristics and operational principles, we would expect lower loss in the slot waveguide. Possible contributors to elevated loss may include scattering losses along silicon sidewalls. The compact dimensions of the hundred nanometer slot amplify the influence of surface roughness on both sides of the silicon slot. Post-annealing offers a potential remedy by reducing surface roughness. Another potential reason is the effect of doping. The higher silicon carrier concentration could introduce additional optical loss. Striking a balance between modulator efficiency, bandwidth, and loss requires a study of suitable silicon waveguide doping strategies.

The last recommended area of future work involves the demonstration of a fully operational efficient high-speed optical modulator. The current stage entails the design and demonstration of a passive structure. While simulations paint a promising picture, the immediate focus lies in translating this potential into a tangible, fully operational optical modulator. Substantiating the simulated outcomes through real-world validation is the upcoming objective. Regarding improving the modulator's V_{π}, the most important factor affecting the modulator efficiency is the slot width. Currently, we are confident to fill the SRC into 300 nm wide slot. Further investigation could be focused on the slot filling capability. One possible solution is to tune the etching chemistry to provide a slope to silicon slot waveguide that can facilitate easier material filling. An alternate route involves exploring other deposition techniques, such as ALD, known for superior gap-filling capabilities, to deposit SRC.

These forthcoming research endeavors hold the promise of further refining the capabilities and applications of silicon-rich carbide and its potential impact on integrated photonics.

REFERENCES

1. Cisco, "Cisco Annual Internet Report (2018–2023) White Paper."

2. Ericsson, "Ericsson Mobility Report November 2022," (2022).

3. R. W. Boyd, *Nonlinear Optics* (Academic Press, 2020).

4. J. Leuthold, W. Freude, J.-M. Brosi, R. Baets, P. Dumon, I. Biaggio, M. L. Scimeca, F. Diederich, B. Frank, and C. Koos, "Silicon organic hybrid technology—A platform for practical nonlinear optics," Proceedings of the IEEE **97**, 1304-1316 (2009).

5. M. Hochberg, T. Baehr-Jones, G. Wang, M. Shearn, K. Harvard, J. Luo, B. Chen, Z. Shi, R. Lawson, and P. Sullivan, "Terahertz all-optical modulation in a silicon–polymer hybrid system," Nature materials **5**, 703-709 (2006).

6. C. Kieninger, Y. Kutuvantavida, D. L. Elder, S. Wolf, H. Zwickel, M. Blaicher, J. N. Kemal, M. Lauermann, S. Randel, and W. Freude, "Ultra-high electro-optic activity demonstrated in a silicon-organic hybrid modulator," Optica **5**, 739-748 (2018).

7. T. W. Baehr-Jones, and M. J. Hochberg, "Polymer silicon hybrid systems: A platform for practical nonlinear optics," The Journal of Physical Chemistry C **112**, 8085-8090 (2008).

8. L. Alloatti, R. Palmer, S. Diebold, K. P. Pahl, B. Chen, R. Dinu, M. Fournier, J.-M. Fedeli, T. Zwick, and W. Freude, "100 GHz silicon–organic hybrid modulator," Light: Science & Applications **3**, e173-e173 (2014).

9. C. Xiong, W. H. P. Pernice, J. H. Ngai, J. W. Reiner, D. Kumah, F. J. Walker, C. H. Ahn, and H. X. Tang, "Active silicon integrated nanophotonics: ferroelectric BaTiO3 devices," Nano letters **14**, 1419-1425 (2014).

10. S. Abel, F. Eltes, J. E. Ortmann, A. Messner, P. Castera, T. Wagner, D. Urbonas, A. Rosa, A. M. Gutierrez, and D. Tulli, "Large Pockels effect in micro-and nanostructured barium titanate integrated on silicon," Nature materials **18**, 42-47 (2019).

11. F. Eltes, D. Caimi, F. Fallegger, M. Sousa, E. O'Connor, M. D. Rossell, B. Offrein, J. Fompeyrine, and S. Abel, "Low-loss BaTiO3–Si waveguides for nonlinear integrated photonics," Acs Photonics **3**, 1698-1703 (2016).

12. R. S. Jacobsen, K. N. Andersen, P. I. Borel, J. Fage-Pedersen, L. H. Frandsen, O. Hansen, M. Kristensen, A. V. Lavrinenko, G. Moulin, and H. Ou, "Strained silicon as a new electro-optic material," Nature **441**, 199-202 (2006).

13. S. S. Azadeh, F. Merget, M. P. Nezhad, and J. Witzens, "On the measurement of the Pockels effect in strained silicon," Optics letters **40**, 1877-1880 (2015).

14. M. Borghi, M. Mancinelli, F. Merget, J. Witzens, M. Bernard, M. Ghulinyan, G. Pucker, and L. Pavesi, "High-frequency electro-optic measurement of strained silicon racetrack resonators," Optics letters **40**, 5287-5290 (2015).

15. M. Berciano, G. Marcaud, P. Damas, X. Le Roux, P. Crozat, C. A. Ramos, D. P. Galacho, D. Benedikovic, D. Marris-Morini, and E. Cassan, "Fast linear electro-optic effect in a centrosymmetric semiconductor," Communications Physics **1**, 1-9 (2018).

16. M. Cazzanelli, F. Bianco, E. Borga, G. Pucker, M. Ghulinyan, E. Degoli, E. Luppi, V. Véniard, S. Ossicini, and D. Modotto, "Second-harmonic generation in silicon waveguides strained by silicon nitride," Nature materials **11**, 148-154 (2012).

17. C. Castellan, A. Trenti, C. Vecchi, A. Marchesini, M. Mancinelli, M. Ghulinyan, G. Pucker, and L. Pavesi, "On the origin of second harmonic generation in silicon waveguides with silicon nitride cladding," Scientific reports **9**, 1-12 (2019).

18. C. C. Wang, J. Bomback, W. T. Donlon, C. R. Huo, and a. J. V. James, "Optical third-harmonic generation in reflection from crystalline and amorphous samples of silicon," Physical review letters **57**, 1647 (1986).

19. B. Corcoran, C. Monat, C. Grillet, D. J. Moss, B. J. Eggleton, T. P. White, L. O'Faolain, and T. F. Krauss, "Green light emission in silicon through slow-light enhanced third-harmonic generation in photonic-crystal waveguides," Nature photonics **3**, 206-210 (2009).

20. O. Boyraz, T. Indukuri, and B. Jalali, "Self-phase-modulation induced spectral broadening in silicon waveguides," Optics Express **12**, 829-834 (2004).

21. L. Yin, Q. Lin, and G. P. Agrawal, "Soliton fission and supercontinuum generation in silicon waveguides," Optics letters **32**, 391-393 (2007).

22. I. W. Hsieh, X. Chen, X. Liu, J. I. Dadap, N. C. Panoiu, C.-Y. Chou, F. Xia, W. M. Green, Y. A. Vlasov, and R. M. Osgood, "Supercontinuum generation in silicon photonic wires," Optics express **15**, 15242-15249 (2007).

23. P. Koonath, D. R. Solli, and B. Jalali, "Continuum generation and carving on a silicon chip," Applied Physics Letters **91**, 061111 (2007).

24. K. Yamada, H. Fukuda, T. Tsuchizawa, T. Watanabe, T. Shoji, and S. Itabashi, "All-optical efficient wavelength conversion using silicon photonic wire waveguide," IEEE Photonics Technology Letters **18**, 1046-1048 (2006).

25. H. Rong, Y.-H. Kuo, A. Liu, M. Paniccia, and O. Cohen, "High efficiency wavelength conversion of 10 Gb/s data in silicon waveguides," Optics Express **14**, 1182-1188 (2006).

26. M. A. Foster, A. C. Turner, R. Salem, M. Lipson, and A. L. Gaeta, "Broad-band continuous-wave parametric wavelength conversion in silicon nanowaveguides," Optics Express **15**, 12949-12958 (2007).

27. T. Vallaitis, C. Heine, R. Bonk, W. Freude, J. Leuthold, C. Koos, B. Esembeson, I. Biaggio, T. Michinobu, and F. Diederich, "All-optical wavelength conversion at 42.7 Gbit/s in a 4 mm long silicon-organic hybrid waveguide," (Optical Society of America), p. OWS3.

28. M. A. Foster, A. C. Turner, J. E. Sharping, B. S. Schmidt, M. Lipson, and A. L. Gaeta, "Broad-band optical parametric gain on a silicon photonic chip," Nature **441**, 960-963 (2006).

29. X. Liu, R. M. Osgood, Y. A. Vlasov, and W. M. J. Green, "Mid-infrared optical parametric amplifier using silicon nanophotonic waveguides," Nature Photonics **4**, 557-560 (2010).

30. J. Leuthold, C. Koos, and W. Freude, "Nonlinear silicon photonics," Nature photonics **4**, 535-544 (2010).

31. H. K. Tsang, and Y. Liu, "Nonlinear optical properties of silicon waveguides," Semiconductor Science and Technology **23**, 064007 (2008).

32. J. Komma, C. Schwarz, G. Hofmann, D. Heinert, and R. Nawrodt, "Thermo-optic coefficient of silicon at 1550 nm and cryogenic temperatures," Applied Physics Letters **101**, 041905 (2012).

33. S. Chung, M. Nakai, and H. Hashemi, "Low-power thermo-optic silicon modulator for large-scale photonic integrated systems," Optics express **27**, 13430-13459 (2019).

34. G. Qin, Q. Zhu, and Y. Su, "Fast wavelength seeking in a silicon dual-ring switch based on artificial neural networks," Journal of Lightwave Technology **38**, 5078-5085 (2020).

35. K. Van Acoleyen, W. Bogaerts, J. Jágerská, N. Le Thomas, R. Houdré, and R. Baets, "Off-chip beam steering with a one-dimensional optical phased array on silicon-on-insulator," Optics letters **34**, 1477-1479 (2009).

36. S. Chung, H. Abediasl, and H. Hashemi, "A monolithically integrated large-scale optical phased array in silicon-on-insulator CMOS," IEEE Journal of Solid-State Circuits **53**, 275-296 (2017).

37. D. Pérez-López, A. López, P. DasMahapatra, and J. Capmany, "Multipurpose self-configuration of programmable photonic circuits," Nature communications **11**, 6359 (2020).

38. W. Bogaerts, D. Pérez, J. Capmany, D. A. B. Miller, J. Poon, D. Englund, F. Morichetti, and A. Melloni, "Programmable photonic circuits," Nature **586**, 207-216 (2020).

39. J. Wang, S. Paesani, Y. Ding, R. Santagati, P. Skrzypczyk, A. Salavrakos, J. Tura, R. Augusiak, L. Mančinska, and D. Bacco, "Multidimensional quantum entanglement with large-scale integrated optics," Science **360**, 285-291 (2018).

40. J. W. Silverstone, D. Bonneau, K. Ohira, N. Suzuki, H. Yoshida, N. Iizuka, M. Ezaki, C. M. Natarajan, M. G. Tanner, and R. H. Hadfield, "On-chip quantum interference between silicon photon-pair sources," Nature Photonics **8**, 104-108 (2014).

41. V. E. Chelnokov, and A. L. Syrkin, "High temperature electronics using SiC: actual situation and unsolved problems," Materials Science and Engineering: B **46**, 248-253 (1997).

42. I. J. Wu, and G. Y. Guo, "Second-harmonic generation and linear electro-optical coefficients of SiC polytypes and nanotubes," Physical Review B **78**, 035447 (2008).

43. Y. Zheng, M. Pu, A. Yi, X. Ou, and H. Ou, "4H-SiC microring resonators for nonlinear integrated photonics," Optics letters **44**, 5784-5787 (2019).

44. X. Lu, J. Y. Lee, P. X. L. Feng, and Q. Lin, "High Q silicon carbide microdisk resonator," Applied Physics Letters **104**, 181103 (2014).

45. T. Fan, X. Wu, A. A. Eftekhar, M. Bosi, H. Moradinejad, E. V. Woods, and A. Adibi, "High-quality integrated microdisk resonators in the visible-to-near-infrared wavelength range on a 3C-silicon carbide-on-insulator platform," Optics Letters **45**, 153-156 (2020).

46. C. Wang, Z. Fang, A. Yi, B. Yang, Z. Wang, L. Zhou, C. Shen, Y. Zhu, Y. Zhou, and R. Bao, "High-Q microresonators on 4H-silicon-carbide-on-insulator platform for nonlinear photonics," Light: Science & Applications **10**, 139 (2021).

47. Y. Zheng, M. Pu, A. Yi, B. Chang, T. You, K. Huang, A. N. Kamel, M. R. Henriksen, A. A. Jørgensen, and X. Ou, "High-quality factor, high-confinement microring resonators in 4H-silicon carbide-on-insulator," Optics express **27**, 13053-13060 (2019).

48. T. Fan, H. Moradinejad, X. Wu, A. A. Eftekhar, and A. Adibi, "High-Q integrated photonic microresonators on 3C-SiC-on-insulator (SiCOI) platform," Optics express **26**, 25814-25826 (2018).

49. J. Cardenas, M. Zhang, C. T. Phare, S. Y. Shah, C. B. Poitras, B. Guha, and M. Lipson, "High q sic microresonators," Optics express **21**, 16882-16887 (2013).

50. D. M. Lukin, C. Dory, M. A. Guidry, K. Y. Yang, S. D. Mishra, R. Trivedi, M. Radulaski, S. Sun, D. Vercruysse, and G. H. Ahn, "4H-silicon-carbide-on-insulator for integrated quantum and nonlinear photonics," Nature Photonics **14**, 330-334 (2020).

51. F. Martini, and A. Politi, "Four wave mixing in 3C SiC ring resonators," Applied Physics Letters **112**, 251110 (2018).

52. M. A. Guidry, K. Y. Yang, D. M. Lukin, A. Markosyan, J. Yang, M. M. Fejer, and J. Vučković, "Optical parametric oscillation in silicon carbide nanophotonics," Optica **7**, 1139-1142 (2020).

53. B.-S. Song, T. Asano, S. Jeon, H. Kim, C. Chen, D. D. Kang, and S. Noda, "Ultrahigh-Q photonic crystal nanocavities based on 4H silicon carbide," Optica **6**, 991-995 (2019).

54. S. Yamada, B.-S. Song, S. Jeon, J. Upham, Y. Tanaka, T. Asano, and S. Noda, "Second-harmonic generation in a silicon-carbide-based photonic crystal nanocavity," Optics letters **39**, 1768-1771 (2014).

55. J. Cardenas, M. Yu, Y. Okawachi, C. B. Poitras, R. K. W. Lau, A. Dutt, A. L. Gaeta, and M. Lipson, "Optical nonlinearities in high-confinement silicon carbide waveguides," Optics letters **40**, 4138-4141 (2015).

56. L. Di Cioccio, F. Letertre, Y. Le Tiec, A. M. Papon, C. Jaussaud, and M. Bruel, "Silicon carbide on insulator formation by the Smart-Cut® process," Materials Science and Engineering: B **46**, 349-356 (1997).

57. X. Wu, T. Fan, A. A. Eftekhar, and A. Adibi, "High-Q microresonators integrated with microheaters on a 3C-SiC-on-insulator platform," Optics letters **44**, 4941-4944 (2019).

58. X. Lu, J. Y. Lee, S. Rogers, and Q. Lin, "Optical Kerr nonlinearity in a high-Q silicon carbide microresonator," Optics express **22**, 30826-30832 (2014).

59. P. Xing, D. Ma, K. J. A. Ooi, J. W. Choi, A. M. Agarwal, and D. Tan, "CMOS-compatible PECVD silicon carbide platform for linear and nonlinear optics," ACS Photonics **6**, 1162-1167 (2019).

60. Y. Shoji, K. Nakanishi, Y. Sakakibara, K. Kintaka, H. Kawashima, M. Mori, and T. Kamei, "Hydrogenated amorphous silicon carbide optical waveguide for telecommunication wavelength applications," Applied Physics Express **3**, 122201 (2010).

61. F. G. Della Corte, M. E. Montefusco, L. Moretti, I. Rendina, and A. Rubino, "Study of the thermo-optic effect in hydrogenated amorphous silicon and hydrogenated amorphous silicon carbide between 300 and 500 K at 1.55 μm," Applied Physics Letters **79**, 168-170 (2001).

62. M. Hiramoto, K. Yoshimura, and M. Yokoyama, "Photo-modulation of light up-conversion in light transducer using high-gain photoresponsive amorphous silicon carbide combined with organic electroluminescent diode," Applied physics letters **60**, 324-325 (1992).

63. X. Yu, B. Ding, H. Lu, Y. Huo, Q. Peng, X. Xiu, C. Zhang, C. Yang, S. Jiang, and B. Man, "Third-order optical nonlinearity in nonstoichiometric amorphous silicon carbide films," Journal of Alloys and Compounds **794**, 518-524 (2019).

64. K. Akiyama, A. Takimoto, and H. Ogawa, "Photoaddressed spatial light modulator using transmissive and highly photosensitive amorphous-silicon carbide film," Applied optics **32**, 6493-6500 (1993).

65. G. Cocorullo, F. G. Della Corte, I. Rendina, A. Rubino, and E. Terzini, "Thermo-optical modulation at/spl lambda/= 1.5 μm in an/spl alpha/-SiC-/spl alpha/-Si-/spl alpha/-SiC planar guided-wave structure," IEEE Photonics Technology Letters **8**, 900-902 (1996).

66. E. Timurdogan, C. V. Poulton, M. J. Byrd, and M. R. Watts, "Electric field-induced second-order nonlinear optical effects in silicon waveguides," Nature Photonics **11**, 200-206 (2017).

67. C. G. Bottenfield, V. A. Thomas, and S. E. Ralph, "Silicon photonic modulator linearity and optimization for microwave photonic links," IEEE Journal of Selected Topics in Quantum Electronics **25**, 1-10 (2019).

68. C. Castellan, R. Franchi, S. Biasi, M. Bernard, M. Ghulinyan, and L. Pavesi, "Field-induced nonlinearities in silicon waveguides embedded in lateral pn junctions," Frontiers in Physics **7**, 104 (2019).

69. P. T. B. Shaffer, "Refractive index, dispersion, and birefringence of silicon carbide polytypes," Applied optics **10**, 1034-1036 (1971).

70. H. Shang, D. Sun, P. Yu, B. Wang, T. Yu, T. Li, and H. Jiang, "Investigation for sidewall roughness caused optical scattering loss of silicon-on-insulator waveguides with confocal laser scanning microscopy," Coatings **10**, 236 (2020).

71. D. Brassard, and M. A. El Khakani, "Dielectric properties of amorphous hydrogenated silicon carbide thin films grown by plasma-enhanced chemical vapor deposition," Journal of applied physics **93**, 4066-4071 (2003).

72. S. M. Sze, Y. Li, and K. K. Ng, Physics of semiconductor devices (John wiley & sons, 2021).

73. W. Bogaerts, P. De Heyn, T. Van Vaerenbergh, K. De Vos, S. Kumar Selvaraja, T. Claes, P. Dumon, P. Bienstman, D. Van Thourhout, and R. Baets, "Silicon microring resonators," Laser & Photonics Reviews **6**, 47-73 (2012).

74. A. Friedman, H. Nejadriahi, R. Sharma, and Y. Fainman, "Demonstration of the DC-Kerr effect in silicon-rich nitride," Optics Letters **46**, 4236-4239 (2021).

75. K. Ikeda, R. E. Saperstein, N. Alic, and Y. Fainman, "Thermal and Kerr nonlinear properties of plasma-deposited silicon nitride/silicon dioxide waveguides," Optics express **16**, 12987-12994 (2008).

76. K. J. A. Ooi, D. K. T. Ng, T. Wang, A. K. L. Chee, S. K. Ng, Q. Wang, L. K. Ang, A. M. Agarwal, L. C. Kimerling, and D. T. H. Tan, "Pushing the limits of CMOS optical parametric amplifiers with USRN: Si7N3 above the two-photon absorption edge," Nature communications **8**, 13878 (2017).

77. M. Ferrera, L. Razzari, D. Duchesne, R. Morandotti, Z. Yang, M. Liscidini, J. E. Sipe, S. Chu, B. E. Little, and D. J. Moss, "Low-power continuous-wave nonlinear optics in doped silica glass integrated waveguide structures," Nature photonics **2**, 737-740 (2008).

78. H. Jung, C. Xiong, K. Y. Fong, X. Zhang, and H. X. Tang, "Optical frequency comb generation from aluminum nitride microring resonator," Optics letters **38**, 2810-2813 (2013).

79. B. J. M. Hausmann, I. Bulu, V. Venkataraman, P. Deotare, and M. Lončar, "Diamond nonlinear photonics," Nature Photonics **8**, 369-374 (2014).

80. C. L. Wu, C. H. Hsieh, G. R. Lin, W. C. Chi, Y. J. Chiu, Y. Y. Lin, Y. J. Hung, M. H. Shih, A. K. Chu, and C. K. Lee, "Tens of GHz Tantalum pentoxide-based micro-ring all-optical modulator for Si photonics," Annalen der Physik **529**, 1600358 (2017).

81. S. Wang, M. Zhan, G. Wang, H. Xuan, W. Zhang, C. Liu, C. Xu, Y. Liu, Z. Wei, and X. Chen, "4H-SiC: a new nonlinear material for midinfrared lasers," Laser & Photonics Reviews **7**, 831-838 (2013).

82. L.-Y. S. Chang, H. Nejadriahi, S. Pappert, and P. K. L. Yu, "Demonstration of DC Kerr effect induced high nonlinear susceptibility in silicon rich amorphous silicon carbide," Applied Physics Letters **120**, 071107 (2022).

83. L.-Y. S. Chang, S. Pappert, and K. L. Paul, "Thermo-optic Properties in PECVD Silicon Rich Silicon Carbide," (Optica Publishing Group), pp. NoTh2E-4.

84. L.-Y. S. Chang, S. Pappert, and K. L. Paul, "High thermo-optic tunability in PECVD silicon-rich amorphous silicon carbide," Optics letters **48**, 1188-1191 (2023).

85. X. Shi, W. Fan, A. K. Hansen, M. Chi, A. Yi, X. Ou, K. Rottwitt, and H. Ou, "Thermal Behaviors and Optical Parametric Oscillation in 4H-Silicon Carbide Integrated Platforms," Advanced Photonics Research **2**, 2100068 (2021).

86. S. Yamada, B.-S. Song, T. Asano, and S. Noda, "Experimental investigation of thermo-optic effects in SiC and Si photonic crystal nanocavities," Optics letters **36**, 3981-3983 (2011).

87. Y. Lu, X. Shi, D. Chaussende, K. Rottwitt, and H. Ou, "Thermal-tuning of Amorphous Silicon Carbide Nanophotonic Devices," (Optica Publishing Group), pp. JW3B-190.

88. H. Lin, Y. Song, Y. Huang, D. Kita, S. Deckoff-Jones, K. Wang, L. Li, J. Li, H. Zheng, and Z. Luo, "Chalcogenide glass-on-graphene photonics," Nature Photonics **11**, 798-805 (2017).

89. H. Qiu, Y. Liu, C. Luan, D. Kong, X. Guan, Y. Ding, and H. Hu, "Energy-efficient thermo-optic silicon phase shifter with well-balanced overall performance," Optics Letters **45**, 4806-4809 (2020).

90. H. Nejadriahi, S. Pappert, Y. Fainman, and P. Yu, "Efficient and compact thermo-optic phase shifter in silicon-rich silicon nitride," Optics Letters **46**, 4646-4649 (2021).

91. J. Joo, J. Park, and G. Kim, "Cost-Effective 2×2 Silicon Nitride Mach-Zehnder Interferometric (MZI) Thermo-Optic Switch," IEEE Photonics Technology Letters **30**, 740-743 (2018).

92. A. Rahim, A. Hermans, B. Wohlfeil, D. Petousi, B. Kuyken, D. Van Thourhout, and R. Baets, "Taking silicon photonics modulators to a higher performance level: state-of-the-art and a review of new technologies," Advanced Photonics **3**, 024003-024003 (2021).

93. G. Sinatkas, T. Christopoulos, O. Tsilipakos, and E. E. Kriezis, "Electro-optic modulation in integrated photonics," Journal of Applied Physics **130** (2021).

94. C. Wang, M. Zhang, X. Chen, M. Bertrand, A. Shams-Ansari, S. Chandrasekhar, P. Winzer, and M. Lončar, "Integrated lithium niobate electro-optic modulators operating at CMOS-compatible voltages," Nature **562**, 101-104 (2018).

95. S. Singh, and S. K. Selvaraja, "Sputter-deposited PZT-on-Silicon electro-optic modulator," (IEEE), pp. 1-2.

96. D. Patel, V. Veerasubramanian, S. Ghosh, A. Samani, Q. Zhong, and D. V. Plant, "High-speed compact silicon photonic Michelson interferometric modulator," Optics express **22**, 26788-26802 (2014).

97. J. Fujikata, S. Takahashi, M. Takahashi, M. Noguchi, T. Nakamura, and Y. Arakawa, "High-performance MOS-capacitor-type Si optical modulator and surface-illumination-type Ge photodetector for optical interconnection," Japanese Journal of Applied Physics **55**, 04EC01 (2016).

98. X. Tu, K.-F. Chang, T.-Y. Liow, J. Song, X. Luo, L. Jia, Q. Fang, M. Yu, G.-Q. Lo, and P. Dong, "Silicon optical modulator with shield coplanar waveguide electrodes," Optics express **22**, 23724-23731 (2014).

99. K. Noguchi, O. Mitomi, H. Miyazawa, and S. Seki, "A broadband Ti: LiNbO/sub 3/optical modulator with a ridge structure," Journal of Lightwave Technology **13**, 1164-1168 (1995).

100. F. Eltes, C. Mai, D. Caimi, M. Kroh, Y. Popoff, G. Winzer, D. Petousi, S. Lischke, J. E. Ortmann, and L. Czornomaz, "A BaTiO 3-based electro-optic Pockels modulator monolithically integrated on an advanced silicon photonics platform," Journal of Lightwave Technology **37**, 1456-1462 (2019).

101. M. He, M. Xu, Y. Ren, J. Jian, Z. Ruan, Y. Xu, S. Gao, S. Sun, X. Wen, and L. Zhou, "High-performance hybrid silicon and lithium niobate Mach–Zehnder modulators for 100 Gbit s− 1 and beyond," Nature Photonics **13**, 359-364 (2019).

102. K. Alexander, J. P. George, B. Kuyken, J. Beeckman, and D. Van Thourhout, "Broadband electro-optic modulation using low-loss PZT-on-silicon nitride integrated waveguides," (Optica Publishing Group), pp. JTh5C-7.